Europa's Plasma Interaction with Jupiter's Magnetosphere: Characterizing Variability with Multi-Fluid MHD Simulations

by

Camilla D. K. Harris

A dissertation submitted in partial fulfillment
of the requirements for the degree of
Doctor of Philosophy
(Climate and Space Sciences and Engineering)
in the University of Michigan
2022

Doctoral Committee:

Associate Professor Xianzhe Jia, Co-Chair
Professor James A. Slavin, Co-Chair
Associate Professor Emily Rauscher
Research Professor Gabor Toth
Dr. Joseph Westlake, Johns Hopkins University Applied Physics Laboratory

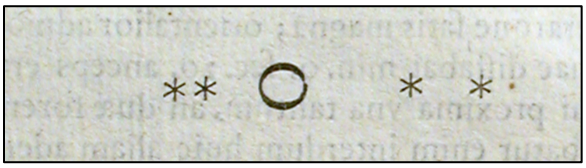

One of Galileo Galilei's drawings of Jupiter and its “Medicean Stars” from Sidereus Nuncius (1610). Jupiter is drawn at the center as a circle flanked by two moons on either side represented by asterisks. A rival astronomer, Simon Marius, gave them the names they are known by today: Io, Europa, Ganymede, and Callisto. Collectively, they are called Jupiter’s Galilean moons.

Camilla D. K. Harris

cdha@umich.edu

ORCID iD: 0000-0001-5045-8827

Dedication

For my Mom,

who gave me the boots,

but always let me find my own way.

Acknowledgements

This work was partially supported by NASA through the Europa Clipper project through contract #1631492 through the Jet Propulsion Laboratory, and contract #143448 through the Applied Physics Laboratory at Johns Hopkins University, and by the Michigan Space Grant Consortium, NASA grant #NNX15AJ20H. This work was also supported by the Rackham Merit Fellowship.

High-performance computing resources supporting this work were provided by the NASA High-End Computing (HEC) Program through the NASA Advanced Supercomputing (NAS) Division at Ames Research Center, and the Texas Advanced Computing Center (TACC) at The University of Texas at Austin.

* * O * *

So many people have supported me over the last five and a half years, during my academic career, and throughout my whole life. Without them this would have taken a lot longer, been a lot more unpleasant, or maybe wouldn't have happened at all.

I need to first thank my advisors and my dissertation committee, who provided valuable feedback on this dissertation. In particular, I need to thank Xianzhe Jia, Jim Slavin, and Gabor Toth, who have mentored me during my time with the Climate and Space Sciences department.

I need to thank my mother and father for fostering a healthy sense of scientific curiosity and excitement about space, and for supporting my first forays in higher education. I need to thank my brother Chris too, for being a good friend and GM and sending cat pictures.

To my comrades from Sunland-Tujunga: you know what you did. Thank you, Julia, Lis, Amy, and Ada. Special thank you to Emily, who went with me from high school to UCLA, and I'm so glad I had you to lean on.

Thank you to my Friends From the Internet: you know who you are.

My friends from UCLA and LANL made my life (and my homework) so much better. Thank you, Anna, Jackie, Phillip, Brittany, Jenn, Szilard ("Sizzle"), Liya, Chloe, Kacie, Addam, Nicole, Emily, and Sara.

My mentors at UCLA made it possible for me to go to graduate school: thank you, Christine and Vassilis. My mentors at GSFC and LANL helped me understand why I wanted to do it: thank you, Alex and Mike. I need to thank Alex in particular, for teaching me how to use emacs rectangles, without which a lot of this research would have been so much more annoying.

Thank you to the IT and administrative staff of the Climate and Space department, for their encouragement, friendliness, and chats in the kitchen: Faye, Bryan, Darren, Cameron, Kevin, Claire, Sandy, Laura and EJ.

I need to thank my friends that I've met at UM, who shared lunch and ideas with me on so many occasions. Thank you, Yash, Ryan, Hongyang, Yeimy, Garrett, Tim, Natasha, Kali, Emily, Jamie, Leonardo, Zhenguang, Doga, Gang kai, and Wami. I need to thank Abby in particular, for so many reasons but they all amount to simply being a good friend. I also need to thank Brian, Alex, and Agnit for joining me at our writing club over the past few months. Good luck, guys.

Space science is one of the few categories of science where much of it actually happens in a vacuum. Space scientists, however, do not live in a vacuum. Thank you so much to the Magnetospheres of the Outer Planets community for supporting your students and early career

scientists. Thank you to the many friends I've met at MOP meetings, but in particular, Max, Zoe, Gianluca, and dear Henry.

Thank you to the Europa Clipper team for supporting this research, and in particular, thank you to the ECM and PIMS teams for many useful discussions that helped shape it. Thank you also to Tom for an exciting collaboration, and helping me figure out how to take this research further.

The most ancient form of the university is a union of scholars, and the university only continues to work because the students do. Thank you to the Graduate Employees' Organization for making all of our lives better through collective bargaining.

In case this thesis is being read by anthropologists hundreds of years in the future, I need to acknowledge that much of it was written during the COVID-19 pandemic. The pandemic has cost hundreds of thousands of people their lives all over the world. In response, we have been isolating and social distancing to try and preserve public health. The past two years would have been very lonely indeed without the online support of the UM GOSTEM chapter, who helped me through the last mile with RPGs, socially distanced nature walks, Revolutionary Girl Utena, Xena: Warrior Princess, various plants, and monster movies.

Preface

The research presented in Chapter 2 and Chapter 3 was previously published as Harris, C. D. K., Jia, X., Slavin, J. A., Toth, G., Huang, Z., & Rubin, M. (2021). Multi-fluid MHD simulations of Europa's plasma interaction under different magnetospheric conditions. *JGR: Space Physics*, doi:10.1029/2020JA028888. The research presented in Chapter 2, Chapter 3, and Chapter 4 was previously presented in oral and poster sessions at the American Geophysical Union Fall Meeting and the Magnetospheres of the Outer Planets Conference, as well as at other scientific meetings, workshops, schools, and journal clubs.

Table of Contents

Dedication ii

Acknowledgements iii

Preface vi

List of Tables x

List of Figures xi

Abstract xviii

Chapter 1 Introduction 1

1.1 Europa's plasma interaction with Jupiter's magnetosphere 2

1.1.1 Jupiter's inner magnetosphere 2

1.1.2 Europa's space environment 5

1.2 *In situ* and remote observations 11

1.2.1 Magnetic field 11

1.2.2 Bulk plasma parameters 11

1.2.3 Ionosphere 12

1.2.4 Atmosphere and potential water plumes 13

1.3 Modeling Europa's plasma interaction 14

1.3.1 The multi-fluid magnetohydrodynamic approach 14

1.3.2 Advances in computational models for Europa's plasma interaction 15

1.4 Outstanding questions 18

1.5 Outline of the dissertation 20

Chapter 2 The Multi-Fluid Magnetohydrodynamic Model for Europa's Plasma Interaction ... 21
2.1 Model equations ... 22
2.2 Numerical aspects ... 26
2.3 Source and loss terms ... 27
2.3.1 Electron impact ionization and photoionization ... 30
2.3.2 Charge exchange ... 32
2.3.3 Recombination ... 32
2.4 Boundary conditions ... 33
2.5 Neutral atmosphere ... 34
2.6 Model validation: *Galileo* E4 and E14 flybys ... 36
2.6.1 The E4 flyby ... 38
2.6.2 The E14 flyby ... 44
2.7 Conclusions ... 48
Chapter 3 Effect of Jovian Magnetospheric Conditions on Precipitation of Thermal Plasma to Europa's Surface ... 50
3.1 Methods ... 52
3.2 Results ... 57
3.3 Discussion ... 66
3.3.1 Spatial distribution of precipitation ... 68
3.3.2 Trends in the total precipitation rate ... 72
3.4 Conclusions ... 76
Chapter 4 Insights from the *Galileo* E15 Flyby on the Effects of Solar Illumination on Europa's Plasma Interaction ... 79
4.1 Simulations of the *Galileo* E15 flyby ... 82
4.1.1 Run 1: E4-like atmosphere ... 85
4.1.2 Run 2: Milillo et al. (2016) atmosphere ... 85

4.1.3 Leading atmospheric bulge 86
4.2 Results and Discussion 87
4.2.1 Evaluation of the data-model comparisons for Runs 1, 2, and 3 91
4.2.2 Evidence of enhanced ion pick-up during the E15 flyby 96
4.2.3 Likelihood of a water plume during the E15 flyby 98
4.3 Conclusions 99
Chapter 5 Effects of Variation in Europa's Atmosphere on the Plasma Interaction 102
5.1 Methods 104
5.2 Results 108
5.3 Precipitation of thermal plasma 119
5.4 Conclusions 126
Chapter 6 Summary and Outlook 130
6.1 Summary 130
6.2 Outlook 134
6.2.1 Connections with Europa Clipper 134
6.2.2 Coupling between Europa's surface, atmosphere, and plasma interaction. 135
Appendices 137
Appendix A Coordinate Systems 138
A.1 Jupiter System-III 138
A.2 E-Phi-Omega (EPO) 139
A.3 E-Phi-B (EPB) 140
A.4 Europa Geographic 142
Bibliography 144

List of Tables

Table 2.1: Chemical processes represented in the model. For each process the corresponding reference from which the reaction rates were implemented is given. Note that while O is referenced in the reactions for completeness, the model does not include neutral O. Note also that while O_2 is consumed and produced by these reactions, in the model the O_2 density is not modified. 27

Table 3.1: Simulation boundary conditions. Magnetic field and plasma parameters for the outer boundary and induced dipole moment for each simulation. 53

Table 3.2: Mass-loading and charge exchange rates calculated for the ion species in each simulation. 59

Table 3.3: Total magnetospheric O^+ precipitation rate [10^{24} ions/s] in all 9 simulations. 74

Table 5.1: O_2 column density over Europa's surface for each of 9 atmospheres in the parameter study. In each cell we give the average column density over the whole surface followed by the minimum and maximum column densities in parentheses. In each atmosphere the maximum occurs at the apex of the trailing hemisphere, while the minimum occurs on the leading hemisphere. 107

List of Figures

Figure 1.1: Relative scales of Jupiter's magnetosphere (A), the Io plasma torus (B), and Europa's plasma interaction (C). Panel A is reproduced from Khurana et al. (2004) and Panel B from Bagenal et al. (2015). 3

Figure 1.2: The variation of Jupiter's magnetic field as seen at Europa's location in the magnetosphere (not to scale). Column A illustrates Jupiter, its magnetic field, and the orientations of the planetary rotation (Ω) and magnetic moment (M) vectors. Columns B and C illustrate Europa's position in the magnetosphere and the local orientation of the Jovian magnetic field. Column D indicates time, which progresses from the top to the bottom of the figure. At t_0, Europa is located at the magnetic equator and the magnetospheric magnetic field is directed southward. At t_0+3 hours Jupiter has completed a quarter of its rotation, causing the magnetic equator to dip below the moon, and such that Europa sees a magnetospheric magnetic field with a radial component directed away from Jupiter. The rotation continues; after 11 hours Jupiter has completed its rotation and the system returns to the original state. 4

Figure 1.3: Particles and kinetic processes in Europa's ionosphere, and a not-to-scale simple model for Europa's interior. Europa's interior is generally modeled as a rocky core surrounded by a briny ocean and a surface layer of ice. The moon is then surrounded by a tenuous atmosphere. The atmosphere is generated by sputtering interactions wherein magnetospheric plasma and energetic particles strike the ice, releasing neutral particles. Neutrals are then ionized by magnetospheric electrons and photons, producing the cold plasma of Europa's ionosphere. These cold ions can then undergo charge exchange with the local neutral population. Magnetospheric ions also engage in charge exchange with the atmospheric neutrals. 6

Figure 1.4: Europa's surface, assembled from images captured by the Galileo Solid State Imaging experiment. Credit: NASA/JPL-Caltech/SETI Institute. 7

Figure 1.5: Schematic of the Alfvén wings. The moon is at the center, the magnetic field (labeled "B") points mainly downward, and ambient plasma flows (labeled "V") from left to right in Panel A, or into the page in Panel B. The currents associated with the perturbations to the magnetic field are labeled "J" in Panel B. After Kivelson et al. (2009) Figure 6. 7

Figure 1.6: Jupiter's aurora with the footprints of three Galilean moons imaged by the Hubble Space Telescope. Credit: modified by JHUAPL from NASA/Space Telescope Science Institute/Association of Universities for Research in Astronomy. 10

Figure 2.1: The simulation grid in the Z=0 plane shown in successively smaller scales. Panel A shows the whole simulation space extending from R=1-64 R_{Eu}. Panel B shows the first layer of grid refinement at R=20 R_{Eu}; Panel C shows the second and third layers of refinement at R=4 R_{Eu}

and R=3 R_{Eu}. Panel D shows the cells closest to Europa's surface on the upstream side of the plasma interaction, and includes the density of the atmosphere in color contours. In Panel D a red bar indicates the 100 km scale height of the atmosphere..... 25

Figure 2.2: The E4 and E14 flyby trajectories in the (A) YZ and (B) XY planes. In Panel B symbols mark the points when the spacecraft entered and exited the region of Y = [1, -1]. The grey shaded region marks Europa's downstream geometric wake. 36

Figure 2.3: Density contours of the three ion fluids (A, C, D) and electron temperature (B) in the Z=0 plane from the simulation of the *Galileo* E4 flyby. Panel A shows the number density of magnetospheric O^+, Panel B shows the temperature of electrons, Panel C shows ionospheric O_2^+, and Panel D shows ionospheric O^+. In Panels A, C, and D the black or white lines with arrows show velocity streamlines of the corresponding ion fluids in the Z=0 plane. In all panels the trajectory of the E4 flyby is marked by a red line..... 37

Figure 2.4: Comparison of simulated magnetic fields to the *Galileo* magnetometer observations for the E4 flyby. Gray dots indicate the *Galileo* magnetometer data, while the solid black line shows the data smoothed with a rolling boxcar average of 50 seconds. The black dashed line indicates the sum of the dipole representing the induced field background Jovian magnetic field. The red solid line gives the simulated magnetic field summed with the trend in the background magnetic field as determined from the data. The vertical black line indicates the time of closest approach, while the gray shaded area spans the time that the spacecraft spent in the region of -1 R_{Eu} < Y < 1 R_{Eu}. 40

Figure 2.5: Color contours showing the B_x (A), B_y (B), and B_z (C) components of the simulation magnetic field from the E4 simulation in the Z=0 plane. In all panels the trajectory of the E4 flyby is marked by a red line. A black line marks the projection of the E14 flyby into the Z=0 plane. 41

Figure 2.6: Comparison of the simulated plasma densities to the *Galileo* PLS total plasma density observations for the E4 flyby. The observed PLS densities are given by black triangles while the color curves show the number density of the Jovian magnetospheric O^+ (blue), O_2^+ (orange), ionospheric O^+ (green), and the total ion number density (red) which is equivalent to the electron density. Other annotations are as described for **Figure 2.4**. 41

Figure 2.7: Comparison of the simulated charge-averaged fluid velocity (red curve) to the *Galileo* PLS total plasma velocity observations for the E4 flyby (Paterson et al., 1999) (black triangles). Other annotations are as described for **Figure 2.4**. 43

Figure 2.8: Comparison of simulated magnetic fields to the Galileo magnetometer observations for the E14 flyby. Annotations are as described for **Figure 2.4**. 45

Figure 2.9: Simulated plasma density for the E14 flyby. Published PLS densities are not available for this flyby. Annotations are as described for **Figure 2.6**. 46

Figure 2.10: Simulated charge-averaged plasma velocity for the E14 flyby. Published PLS velocities are not available for this flyby. Annotations are as described for **Figure 2.6**. 47

Figure 3.1: The range of parameters for the nine simulations at different magnetospheric conditions at Europa: (A) Magnetic latitude, (B) models for the Jovian magnetic field and (C and D) plasma conditions at Europa's orbit. Vertical black lines indicate the System III longitudes at which parameters for 9 simulations were selected. In panels C and D the blue, orange, and green lines correspond respectively to the magnetospheric states 1, 2, and 3 of *Bagenal et al.* (2015). The vertical dashed grey lines indicate the longitudes of the *Galileo* E4 and E14 flybys. 54

Figure 3.2: Contours of u_{qx} overlaid with B_{XZ} field lines in the Y=0 plane for each of the 9 parameter study simulations. 58

Figure 3.3: Simulated number densities on a logarithmic scale in the equatorial plane of the case 1, plasma sheet simulation for (A) Jupiter's magnetospheric O^+ ions, (B) electrons, (C) O_2^+ ions, and (D) ionospheric O^+ ions. 60

Figure 3.4: Color contours of the X component of the simulated velocity for each ion fluid (A: magnetospheric O^+; C: ionospheric O_2^+; D: ionospheric O^+) and the charge-averaged velocity (B) in the equatorial plane of the case 1, plasma sheet simulation, overlaid with streamlines of the X and Y components of the respective velocities. 61

Figure 3.5: Simulated number densities along the -X axis in all simulations for (A) the magnetospheric O+ and (B) the ionospheric O2+ fluids. Blue lines indicate the Case 1 simulations, orange lines indicate Case 2, and green lines indicate Case 3. Solid lines correspond to the simulations in the plasma sheet configuration (19˚ S-III longitude), dashed lines to the transitional configuration (76˚), and dash-dot lines to the lobe configuration (110˚). The flyby simulations are indicated by red dashed lines (E4) and purple solid lines (E14). 64

Figure 3.6: Column densities of Europa's ionosphere along the -X axis in all simulations plotted versus the outer boundary magnetospheric O^+ number density. Blue markers indicate the Case 1 simulations, orange markers indicate Case 2, and green markers indicate Case 3. Circle markers correspond to the simulations in the lobe configuration (19˚ S-III longitude), triangle markers to the transitional configuration (76˚), and square markers to the plasma sheet configuration (110˚). The flyby simulations are indicated by a red triangle marker (E4) and a purple circular marker (E14). 65

Figure 3.7: Precipitation of individual ion fluids in the E4 simulation. Each panel shows the spatial distribution of downward ion precipitation to Europa's surface. The surface was extracted at R = 1.01 R_{Eu} (15.6 km altitude) at a resolution of 1 point per degree. Gray regions block out upward-traveling ions, while white regions indicate low density precipitation below the color threshold. Black plus symbols mark the center of the trailing/upstream hemisphere at 270˚ West Longitude. The center of the anti-Jovian hemisphere is at 180˚. White arrows at 270˚ and 90˚ longitude show the direction of $B_{J,YZ}$ mapped onto the trailing and leading hemispheres, respectively. In panel A, contour lines indicate the temperature of the precipitating magnetospheric O^+ ions in eV. 67

Figure 3.8: Precipitation of the magnetospheric O^+ fluid in the set of 9 parameter study simulations. The format of each panel and the color values are the same as for **Figure 3.7a**.

Columns show simulations of the different magnetospheric states, while rows show the lobe, transition, and plasma sheet simulations for each case. 70

Figure 3.9: Streamlines of magnetospheric O+ in the case 3, plasma sheet simulation. This view looks towards Europa in the +Y direction to observe the anti-Jovian hemisphere. Europa's surface is colored according to the downward flux of magnetospheric O^+. The streamlines are seeded at points on Europa's surface corresponding to the points A-D marked on the case 3, plasma sheet panel in **Figure 3.8**. 71

Figure 3.10: Precipitation rate of magnetospheric O^+ versus (A) magnetic latitude and (B) outer boundary magnetospheric O^+ number density. The markers are organized as in **Figure 3.6**. 74

Figure 4.1: Panel A illustrates the configuration of Europa and Jupiter with respect to solar illumination during the *Galileo* E4 and E25 flybys. Panels B and C compare the trajectory of the *Galileo* spacecraft during these flybys. 81

Figure 4.2: The different atmospheres specified for Run 1 (A), Run 2 (B), and Run 3 (C). Each panel shows color contours of the O_2 number density in the E15 plane (Z = 0.66) as prescribed for each simulation. The black contours identify where the density equals 1000 cm^{-3}. The red line shows the E15 flyby trajectory. White lines indicate where R = 1.0 R_{Eu} and the boundaries of the geometric plasma wake at Y = 1.0 R_{Eu} and Y = -1.0 R_{Eu} 84

Figure 4.3: Data-model comparison for Run 1. Panel A gives the density of each ion fluid and the electron density along the E15 trajectory. Panels B-D give each magnetic field component, and Panel E gives the magnetic field strength. The vertical black line indicates the time of closest approach, and the grey span indicates the time range that the spacecraft spent in the plasma wake, Y=[-1,1] R_{Eu}. In Panels B-E the solid black line gives a 51-second average of the magnetometer data (grey line). 88

Figure 4.4: Data-model comparison for Run 2. Annotations are as for **Figure 4.3**. 89

Figure 4.5: Data-model comparison for Run 3. Annotations are as for **Figure 4.3**. 90

Figure 4.6: The B_X component of the magnetic field for Run 1 (A), Run 2 (B), and Run 3 (C) and the density of the O_2^+ ion fluid for Run 1 (D), Run 2 (E), and Run 3 (F). Each panel shows color contours of the corresponding parameter in the E15 plane (Z = 0.66). Red lines show the E15 flyby trajectory. White lines indicate where R = 1.0 R_{Eu} and the boundaries of the geometric plasma wake at Y = 1.0 R_{Eu} and Y = -1.0 R_{Eu}. 92

Figure 4.7: The density of the O_2^+ ion fluid for Run 1 (A), Run 2 (B), and Run 3 (C). Each panel shows color contours of the O_2^+ number density in the Y=-1 R_{Eu} plane. Red lines show the E15 flyby trajectory, with the point at which the E15 trajectory intersects the Y=-1 R_{Eu} plane marked with a red arrow. White circles indicate where R = 1.0 R_{Eu}. White streamlines indicate the direction of the parallel components of the magnetic field in the Y=-1 R_{Eu} plane. 93

Figure 4.8: Streamtraces of O_2^+ velocity for Run 1 (A, D), Run 2 (B, E), and Run 3 (C, F). Each panel shows 3D streamtraces of the O_2^+ fluid velocity that were seeded on the E15 trajectory during the wake crossing. The streamtraces flow from left to right and are colored according to

the density of O_2^+. The E15 trajectory is indicated by a red line. The left panels (A, B, C) show the XY plane, while the right panels (D, E, F) show the XZ plane. 97

Figure 5.1: Probable O_2 column densities for Europa's atmosphere. Black and white contours describe the upper and lower limits on the column density of Europa's atmosphere determined from observations of Europa's oxygen aurora by the HST (Hall et al., 1995; 1998). Red pluses mark the column density of the primary atmosphere component for each simulation in the parameter study. 107

Figure 5.2: Density of O_2^+ in the equatorial plane for the simulations with low ambient plasma density. 109

Figure 5.3: Density of O_2^+ in the equatorial plane for the simulations with high ambient plasma density. 110

Figure 5.4: Color contours show the magnetic field in the equatorial plane for the simulations with low ambient plasma density. Streamlines indicate the direction of the charge-averaged velocity U_q in the XY plane. 111

Figure 5.5: Color contours show the magnetic field in the equatorial plane for the simulations with high ambient plasma density. Streamlines indicate the direction of the charge-averaged velocity U_q in the XY plane. 112

Figure 5.6: Bulk plasma properties of O_2^+ and B_Z in the equatorial plane for the low ambient plasma density, high atmosphere surface density, high atmosphere scale height simulation (top right panel in **Figure 5.2** and **Figure 5.4**). Panels A, B, and C show respectively the number density, speed, and pressure of the O_2^+ MHD fluid, while Panel D shows B_Z. Streamlines in all four panels indicate the velocity of O_2^+ in the equatorial plane. 113

Figure 5.7: Comparison of atmosphere and ionosphere density profiles in the upstream direction, along the negative X axis. Panel A shows the O_2 density for each atmosphere in the study. Panel B shows the corresponding density of O_2^+. In Panel B solid lines give the density from the simulations with low ambient plasma density, while the dashed lines correspond to simulations with high ambient plasma density..... 114

Figure 5.8: Electron density profiles at low altitudes. In both panels solid lines denote the electron density along the upstream/-X axis, dashed lines correspond to the sub-jovian/+Y axis, and dash-dot lines correspond to the anti-jovian/-Y axis. Panel A gives the electron density for the simulations with low ambient plasma density, while Panel B shows the simulations with high ambient plasma density. Note that the X axes differ between Panel A and Panel B. For Panel A the range was chosen for easy comparison with the *Galileo* radio occultation measurements shown in McGrath et al. (2009), Figure 7. For Panel B the range was increased and scaled logarithmically to show the full variability of the electron density. 116

Figure 5.9: Electron density profiles measured by *Galileo* radio occultations, reproduced from McGrath et al. (2009), Figure 7. 117

Figure 5.10: Column density of O_2^+ integrated along the upstream/-X axis. Circle markers indicate simulations with low ambient plasma density, while squares indicate high ambient plasma density. Note that the markers for the simulations with the highest column density atmosphere overlap each other..... 118

Figure 5.11: Maps of downward flux of the ambient plasma fluid in each of the simulations with low upstream plasma density. Grey regions block out locations where the net flux of plasma is outward. Black pluses mark the ram direction, or the apex of the trailing hemisphere, at 0˚ latitude and 270˚ West longitude. Orange contours describe regions where the temperature of the precipitating plasma exceeds 100 eV..... 120

Figure 5.12: Maps of downward flux of the ambient plasma fluid in each of the simulations with high upstream plasma density. Annotations are as described for **Figure 5.11**..... 121

Figure 5.13: 3D streamtraces of the ambient magnetospheric fluid in the simulations with high ambient plasma density, high atmosphere surface density, and either high (A) or low (B) atmosphere scale height. This view shows streamtraces that were seeded upstream and run from left to right, with some terminating on Europa's trailing hemisphere and others continuing downstream. Color contours show the speed of the magnetospheric plasma in the Z=0 plane. The streamlines are colored according to the temperature of the magnetospheric plasma. The simulation shown in Panel A corresponds to **Figure 5.11c**, while Panel B corresponds to **Figure 5.11i**. 122

Figure 5.14: Fraction of streamtraces diverted in each simulation. Annotations are as described for **Figure 5.10**..... 124

Figure 5.15: Integrated downward flux of thermal ambient plasma for each simulation. Annotations are as described for **Figure 5.10**. Trend lines have been fit to the data; the method and fit parameters are discussed in the text. 125

Figure A.1: Diagram of Europa's position in Jupiter System-III longitude. 138

Figure A.2: (A) In the EPhiO coordinate system, Z is aligned with Europa's spin axis. (B) The vector X is along the background flow and $Y = Z \times X$ is positive towards Jupiter..... 139

Figure A.3: (A) In the EPhiB coordinate system, x is along the background flow. (B) The vector $Y = b \times X$ and is positive towards Jupiter, where b is the background Jovian magnetic field at the time of the spacecraft's closest approach. (C) The vector $Z = X \times Y$ and B lies in the XZ plane. 141

Figure A.4: (A) Europa geographic longitude originates at the Jupiter-facing meridian. West longitude increases in the opposite sense to Europa's orbital motion. (B) The hemispheres centered at 0˚ and 180˚ West lon. are respectively called the sub- and anti-Jovian hemispheres. The hemispheres centered at 90˚ and 270˚ West lon. are respectively called the leading and trailing hemispheres in reference to Europa's orbital motion, or the down- and upstream hemispheres in reference to magnetospheric plasma flow. In EPhiO coordinates, the sub-jovian meridian corresponds to the +Y axis, the leading meridian corresponds to the +X axis, the anti-

jovian meridian corresponds to the -Y axis, and the trailing meridian corresponds to the -X axis. 143

Abstract

Europa, one of Jupiter's Galilean moons, is embedded in the region of space dominated by Jupiter's magnetic field known as Jupiter's magnetosphere. The interaction of Jupiter's magnetospheric plasma and magnetic field with Europa's atmosphere, ionosphere, surface, and subsurface ocean is affected by a variety of external and internal factors. This dissertation investigates the variability of Europa's magnetic and plasma environment through the development and application of a multi-fluid magnetohydrodynamics (MHD) model.

Our multi-fluid MHD model simulates the major plasma populations at Europa, including Jupiter's magnetospheric plasma and the major plasma species from the moon's ionosphere, and self-consistently solves for perturbations to the local electromagnetic fields while accounting for key mass-loading and momentum-loading processes at Europa. The model has been used to simulate various *Galileo* mission flybys of Europa, and was validated through comparisons of the magnetic field and plasma data, indicating that the model is suitable to apply to more general investigations of Europa's plasma interaction and its variability.

To characterize the variability of Europa's plasma interaction caused by changes in the conditions of Jupiter's magnetosphere, we have conducted a series of simulations using different upstream parameters that span the known range of external conditions at Europa. By separately tracking multiple ion fluids, we quantified the access of the Jovian magnetospheric plasma to Europa's surface and determined how that access is affected by changing magnetospheric conditions. We found that changes in the external conditions resulting from Jupiter's tilted plasma sheet relative to Europa's orbit lead to significant variations in the amount and spatial

distribution of Jupiter's magnetospheric plasma precipitating onto Europa's surface. The total precipitation rate of the thermal magnetospheric ions increases with the density of the ambient plasma ranging between $(1.8 – 26) \times 10^{24}$ ions/s. Because sputtering of Europa's icy surface by the thermal plasma is an important contributor to the generation of its atmosphere, the variations in the plasma precipitation as revealed by our modeling results provide quantitative constraints for future models for Europa's atmosphere.

We have also investigated the effects of Europa's atmosphere on its plasma interaction by conducting a parametric study in which the atmosphere model was systematically varied to quantitatively assess the role of atmosphere density and scale height in controlling Europa's plasma interaction. We found that variations of the atmosphere within reasonable constraints can result in increases of the density of Europa's ionosphere by several orders of magnitude. The atmosphere also has a strong influence on the precipitation rate of Jupiter's magnetospheric plasma, which decreases with increasing column density of the atmosphere in relatively weak atmosphere cases and then levels off for strong atmospheres at a rate governed by the density of the upstream plasma.

The studies undertaken for this dissertation have provided quantitative characterization of variability of Europa's plasma interaction in response to the external conditions of Jupiter's magnetosphere as well as the internal influences from Europa's atmosphere. Looking into the future, the development of our multi-fluid MHD model and its continued application to Europa provide a critical method to study this fascinating Ocean World in preparation of NASA's *Europa Clipper* mission, which launches in 2024 and will travel to the Jupiter system over the next decade.

Chapter 1 Introduction

Europa is one of many moons of the planet Jupiter; they numbered 79 in total at the latest count (Carnegie Science, 2018). While most of these moons are small, oddly-shaped, or fixed in distant orbits of their parent planet, Europa is one of the four largest Jovian satellites, collectively known as the Galilean moons. The moons are named for 17th century astronomer Galileo Galilei, who first reported their presence in his 1610 pamphlet, *Sidereus Nuncius*:

> "On the 7th day of January in the present year, 1610, in the first hour of the following night, when I was viewing the constellations of the heavens through a telescope, the planet Jupiter presented itself to my view, and as I had prepared for myself a very excellent instrument, I noticed a circumstance which I had never been able to notice before, owing to want of power in my other telescope, namely, that three little stars, small but very bright, were near the planet; and although I believed them to belong to the number of fixed stars, yet they made me somewhat wonder, because they seemed to be arranged exactly in a straight line, parallel to the ecliptic, and to be brighter than the rest of the stars, equal to them in magnitude." (Galilei, 1880)

What Galileo could not have seen through a 17th century telescope is that the Galilean moons are embedded in a complex system of electromagnetic fields and charged particles known as Jupiter's magnetosphere. The moon-magnetosphere interactions between Jupiter and its large satellites shape the magnetosphere as well as the space environments surrounding each moon in different ways.

In the following sections we review the general features of Jupiter's magnetosphere that Europa is embedded within, as well as the space environment local to the moon. We then highlight the in situ and remote observations of Europa that have informed our current

understanding of the plasma interaction. Finally, we discuss the MHD approach to modeling space plasmas and briefly trace the development of computational models for Europa's plasma interaction.

1.1 Europa's plasma interaction with Jupiter's magnetosphere

1.1.1 Jupiter's inner magnetosphere

At ~5 million km in diameter and more than 500 million km long, the magnetosphere of Jupiter is by far the largest structure inside our Solar system. **Figure 1.1a** shows a diagram of the magnetosphere and the different large-scale features within it. The magnetosphere is essentially a region of space in which the strong magnetic field of Jupiter stands off the solar wind and the interplanetary magnetic field emanating from the Sun. Jupiter's fast rotation (with a period of ~10 hours) causes the planetary dipole magnetic field to rotate, with magnetic field lines near the planet traveling at near-corotation speeds (Khurana et al. 2004). In addition to magnetic field, the magnetosphere is filled with plasma originating mainly from the Galilean moon, Io.

Figure 1.1b illustrates the transport of plasma within the inner magnetosphere (<15 R_J, where R_J is Jupiter's radius of ~71,000 km). Here the Jovian magnetic field is dominantly dipolar, pointing mainly southward. Magnetospheric plasma that originates from the orbit of the inner moon Io (at ~ 5.95 R_J) circulates around the planet with the magnetic field, forming the magnetospheric plasma sheet. Io releases ~1 ton/s of neutrals, which are quickly ionized to form a plasma composed mainly of O^+ and S^{++} (Bagenal and Dols, 2020). Over tens of days this plasma is transported radially outward to Europa's orbit.

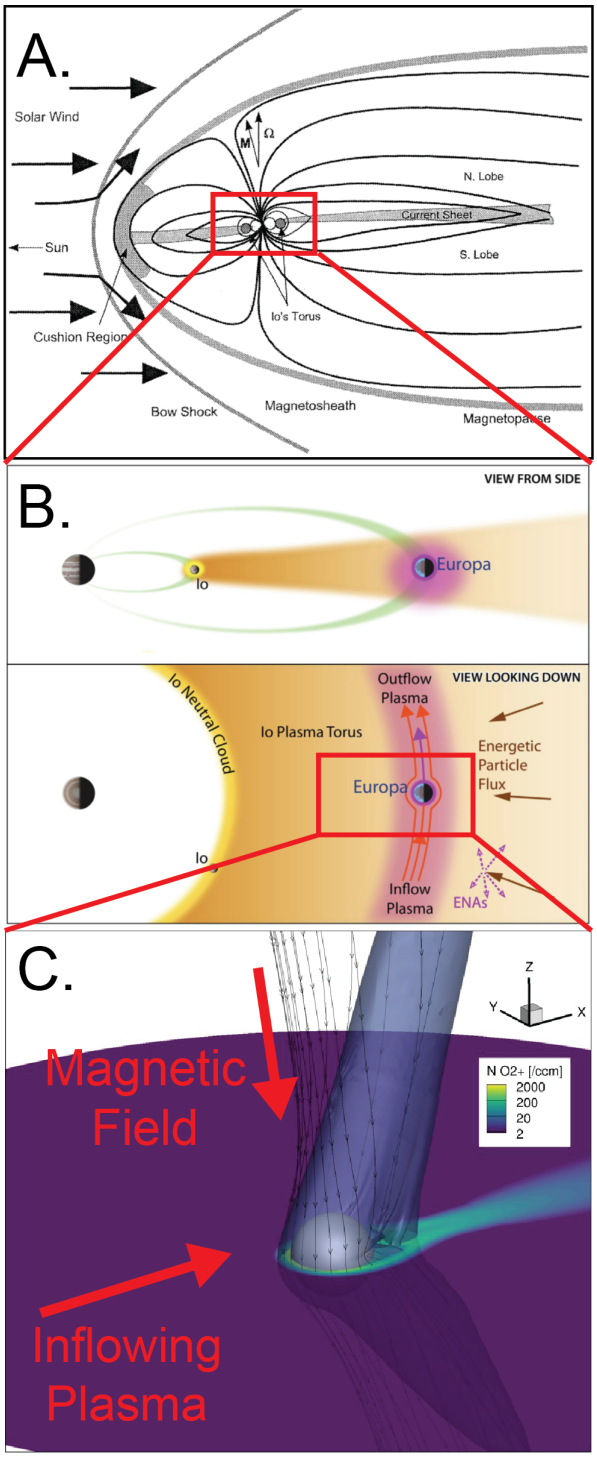

Figure 1.1: Relative scales of Jupiter's magnetosphere (A), the Io plasma torus (B), and Europa's plasma interaction (C). Panel A is reproduced from Khurana et al. (2004) and Panel B from Bagenal et al. (2015).

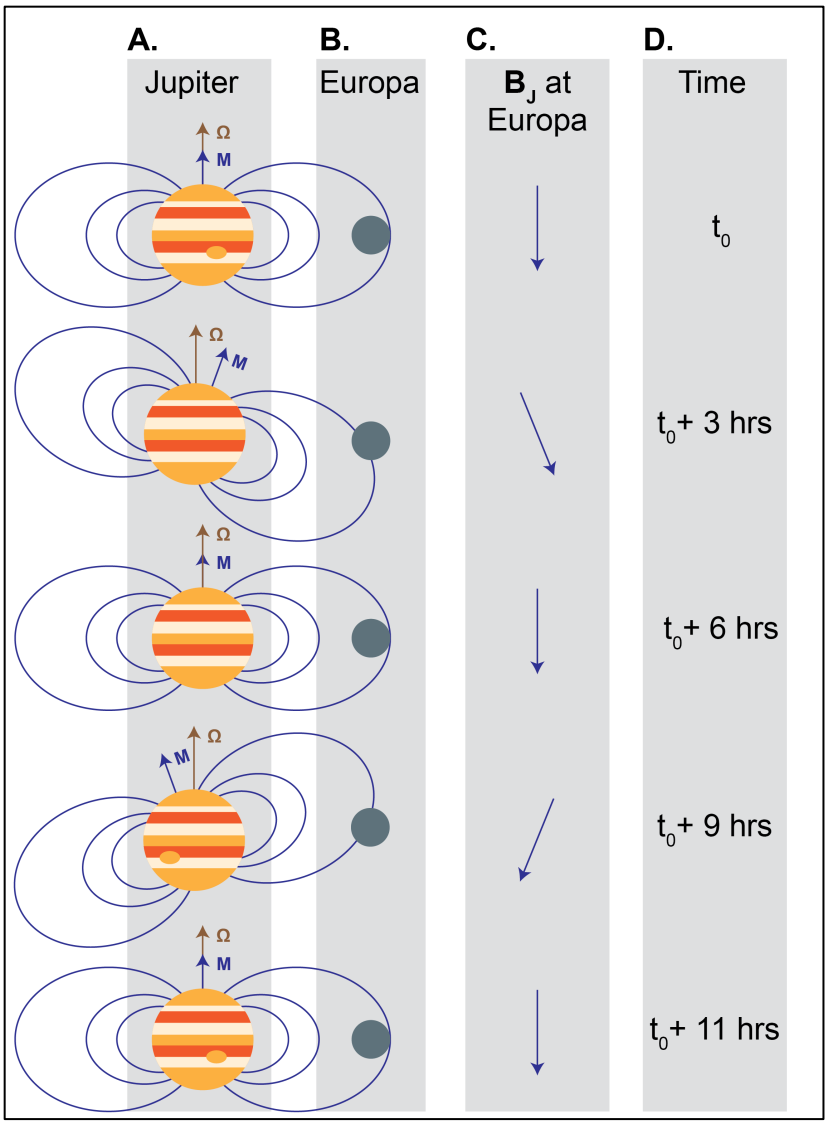

Figure 1.2: The variation of Jupiter's magnetic field as seen at Europa's location in the magnetosphere (not to scale). Column A illustrates Jupiter, its magnetic field, and the orientations of the planetary rotation (Ω) and magnetic moment (M) vectors. Columns B and C illustrate Europa's position in the magnetosphere and the local orientation of the Jovian magnetic field. Column D indicates time, which progresses from the top to the bottom of the figure. At t_0, Europa is located at the magnetic equator and the magnetospheric magnetic field is directed southward. At t_0+3 hours Jupiter has completed a quarter of its rotation, causing the magnetic equator to dip below the moon, and such that Europa sees a magnetospheric magnetic field with a radial component directed away from Jupiter. The rotation continues; after 11 hours Jupiter has completed its rotation and the system returns to the original state.

Europa is embedded within the magnetosphere at 9.4 R_J. Due to Europa's long orbital period (~80 hrs) compared to the period of Jupiter's synodic rotation (~11 hrs), Jupiter's magnetospheric plasma flows past Europa at a relative speed of ~100 km/s. At this distance Jupiter's magnetic field points dominantly southward with a magnetic field strength of ~400 nT. However, due to the tilt of Jupiter's magnetic dipole moment by 10˚ relative to its rotation axis, Jupiter's magnetospheric field "wobbles" over Europa with the planet's rotation, as illustrated in **Figure 1.2**. This wobble causes Europa's position in magnetic latitude to oscillate every 11 hours, and correspondingly the radial and azimuthal components of the magnetic field at Europa's location oscillate at the same period. The same oscillation also modulates the magnetospheric plasma properties at Europa. The center of Jupiter's plasma sheet is tilted by 7˚ from the moon's orbital plane (Bagenal et al., 2015). Therefore, as Jupiter rotates and Europa approaches the center of the plasma sheet the magnetospheric plasma tends to become cooler and denser. Conversely, as Europa reaches its farthest excursions from the center of the plasma sheet the magnetospheric plasma becomes hotter and less dense.

As this magnetized plasma approaches the moon it interacts with Europa's neutral atmosphere and ionosphere, causing perturbations to the flow and the local electromagnetic fields (**Figure 1.1c**). We refer to this system of mixing plasmas and their electromagnetic effects as the plasma interaction between Europa and Jupiter.

1.1.2 Europa's space environment

Figure 1.3 illustrates the different elements of Europa and its space environment discussed in this subsection.

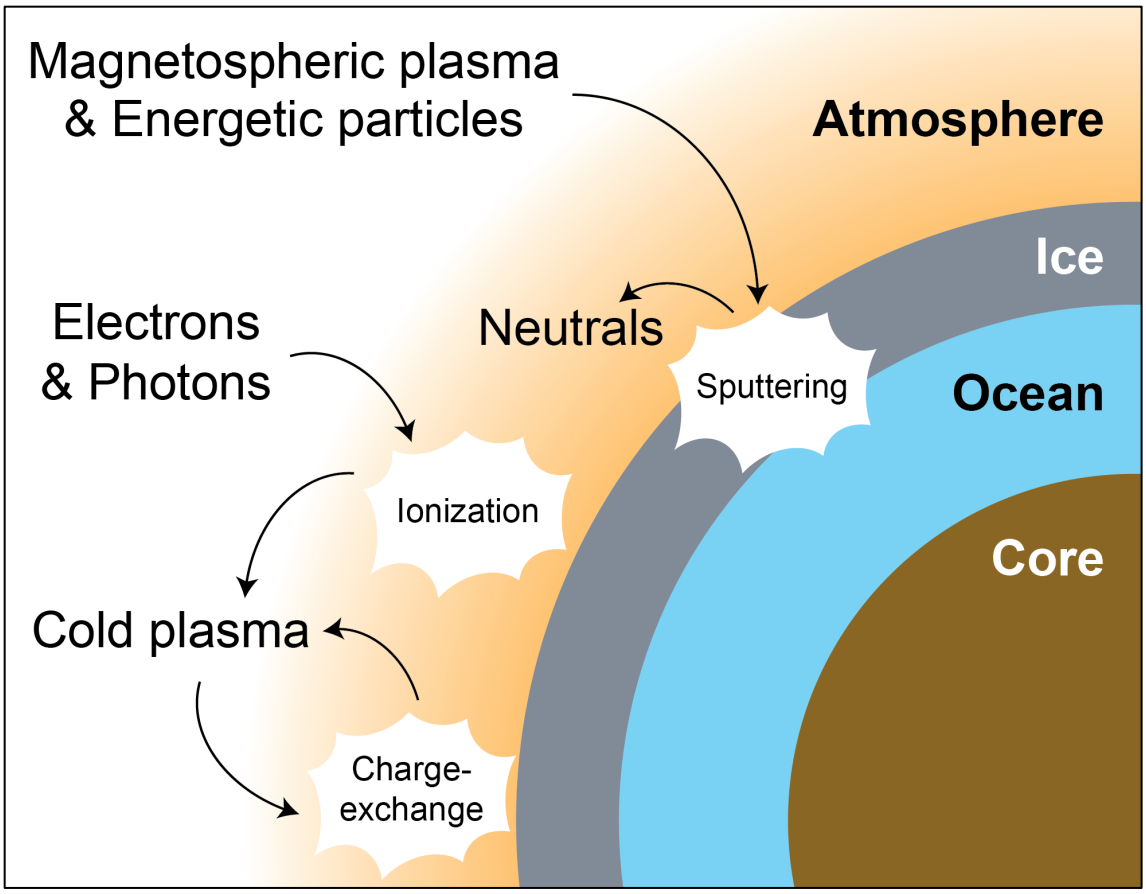

Figure 1.3: Particles and kinetic processes in Europa's ionosphere, and a not-to-scale simple model for Europa's interior. Europa's interior is generally modeled as a rocky core surrounded by a briny ocean and a surface layer of ice. The moon is then surrounded by a tenuous atmosphere. The atmosphere is generated by sputtering interactions wherein magnetospheric plasma and energetic particles strike the ice, releasing neutral particles. Neutrals are then ionized by magnetospheric electrons and photons, producing the cold plasma of Europa's ionosphere. These cold ions can then undergo charge exchange with the local neutral population. Magnetospheric ions also engage in charge exchange with the atmospheric neutrals.

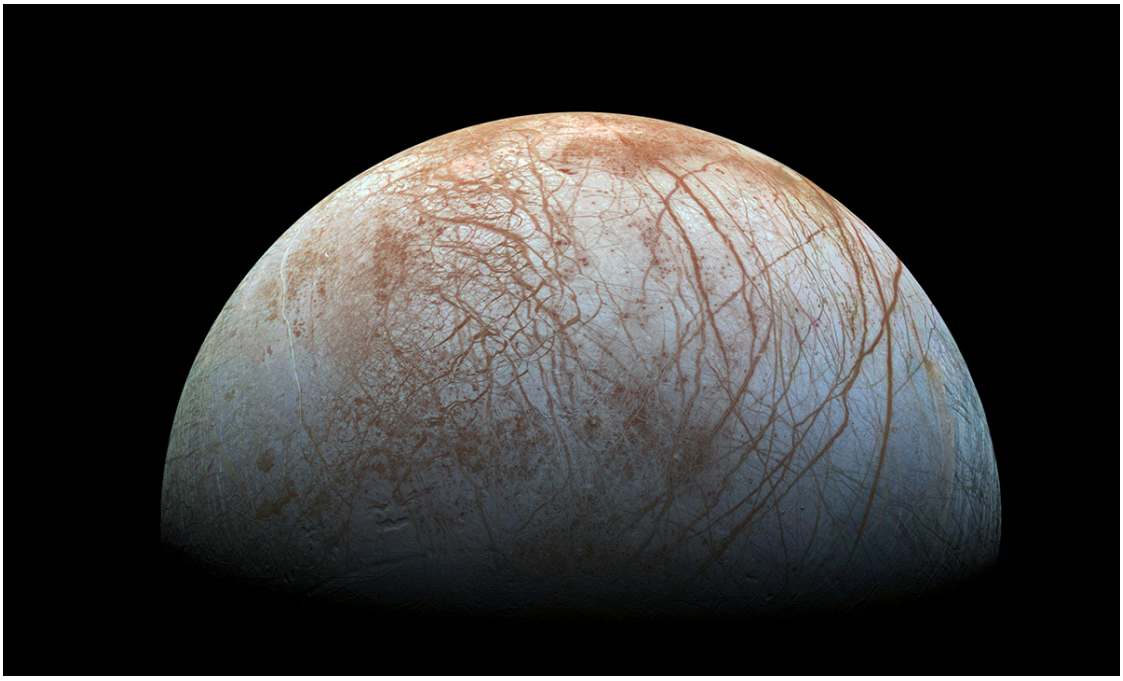

Figure 1.4: Europa's surface, assembled from images captured by the Galileo Solid State Imaging experiment. Credit: NASA/JPL-Caltech/SETI Institute.

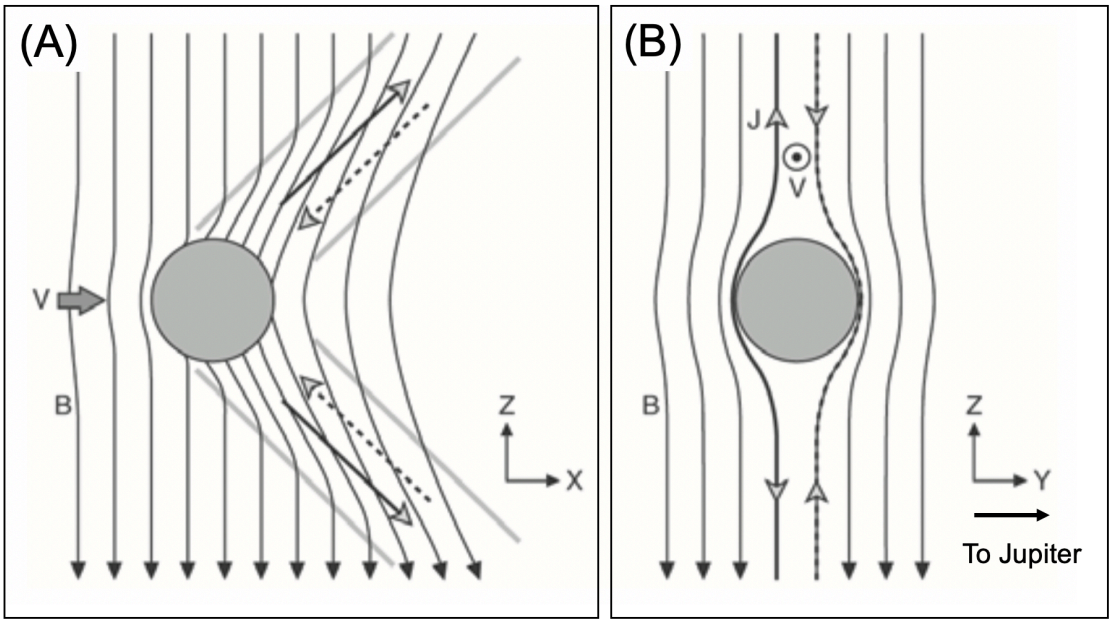

Figure 1.5: Schematic of the Alfvén wings. The moon is at the center, the magnetic field (labeled "B") points mainly downward, and ambient plasma flows (labeled "V") from left to right in Panel A, or into the page in Panel B. The currents associated with the perturbations to the magnetic field are labeled "J" in Panel B. After Kivelson et al. (2009) Figure 6.

Europa's interior is generally understood to be differentiated, with a rocky core, a subsurface ocean, and a layer of ice at the surface (Schubert et al., 2009). **Figure 1.4** shows a true-color image of Europa's water ice surface from the *Galileo* mission. Reddish-brown streaks are thought to be associated with hydrated salts (Carlson et al., 2009).

Europa's icy surface is exposed to bombardment by magnetospheric particles. In addition to the thermal plasma of Jupiter's plasma sheet discussed above, energetic charged particles with energies ranging from several keV to tens of MeV (Paranicas et al., 2009) also strike the surface. In doing so, magnetospheric ions and energetic electrons impart energy into the ice that causes the process known as sputtering, by which neutral material is ejected from Europa's surface. Sputtering yields are governed by many factors, including the energy of the sputtering particle, its angle of impact, and properties of the ice such as composition and temperature (Johnson et al., 2009; Teolis et al., 2017b). Among other processes, such as sublimation and radiolysis, sputtering is responsible for generating Europa's tenuous atmosphere.

Europa's atmosphere is composed mainly of O_2. Though H_2O and H_2 are also present, computational models for the atmosphere suggest that H_2O tends to freeze back into the icy surface, while H_2 is much lighter and tends to escape. O_2 is therefore the most persistent and long-lived component (Johnson et al., 2009). Energetic magnetospheric electrons and solar photons ionize this O_2, generating O_2^+ and O^+ that form Europa's ionosphere.

The presence of Europa's atmosphere and ionosphere, and the process of loading charged particles through ionization, together present an electromagnetic obstacle to the ambient flow of magnetized thermal plasma of Jupiter's magnetosphere. The Alfvén speed of the upstream plasma is variable due to the variations in plasma conditions at Europa's orbit, but the consistently strong magnetospheric magnetic field elevates the Alfvén speed to ~150-700 km/s.

This high Alfvén speed relative to the speed of the ambient plasma (~100 km/s) causes the Alfvénic Mach number to range from 0.3-0.5 (Kivelson et al., 2009; Bagenal and Dols, 2020), leading to a sub-Alfvénic interaction between the ambient magnetospheric plasma and Europa's ionosphere. This type of plasma interaction between moons and their parent planets has been studied for many decades (see, for example, early studies such as that by Neubauer et al. (1980), Southwood et al. (1980) for Io). In brief, the general characteristics of the interaction entail a slowing of the flow upstream of the moon, the accumulation of newly picked-up ions in the downstream wake of the moon, and perturbations to the ambient magnetic field extending to the north and south, known as Alfvén wings. **Figure 1.5** shows a schematic of the Alfvén wings. The perturbations to the magnetic field are caused by the slowing of the flow of plasma in proximity to the moon. Magnetic field lines far upstream of the interaction are undisturbed and uniform, but **Figure 1.5a** shows that as they draw nearer to Europa's surface they are slowed by the loading of mass, and ultimately shear develops between the undisturbed portions of the magnetic field (far to the north and south) and the portions that interact with the moon. In accordance with Ampere's law, this bending of the magnetic field causes currents to flow across the field, which then close through field-aligned currents along the Alfvén wings. These currents close through Europa's ionosphere and run north and south along the magnetospheric magnetic field to Jupiter's ionosphere, where they create auroral footprints, as shown in **Figure 1.6**.

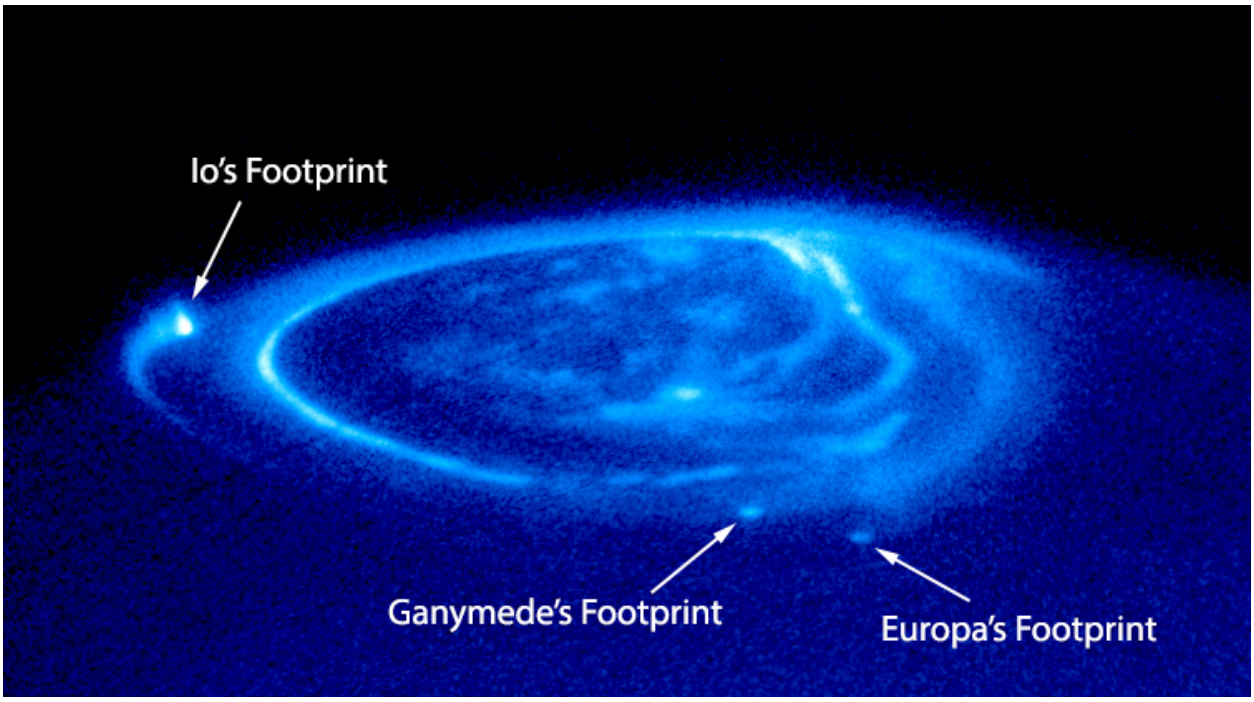

Figure 1.6: Jupiter's aurora with the footprints of three Galilean moons imaged by the Hubble Space Telescope. Credit: modified by JHUAPL from NASA/Space Telescope Science Institute/Association of Universities for Research in Astronomy.

The periodic variation of the Jovian magnetic field over Europa induces eddy currents in Europa's conducting, subsurface ocean. These eddy currents generate induced magnetic fields that oppose the change in the background magnetospheric field, and therefore vary with time. This phenomenon was critical to the *Galileo* mission's discovery of Europa's subsurface ocean. They conducted multiple flybys of Europa, during which the spacecraft magnetometer measured the local magnetic fields and identified the induced field from the ocean (Khurana et al., 1998; Kivelson et al., 2000). This magnetic sounding experiment also underpins the goal of NASA's upcoming *Europa Clipper* mission to characterize Europa's subsurface ocean and assess the potential habitability of the moon (Howell and Pappalardo, 2020).

1.2 *In situ* and remote observations

Over the last several decades many observations, some *in situ* and others remote, have been made of the particles and electromagnetic fields that make up Europa's space environment. Of central importance to this dissertation are the measurements made by the *Galileo* mission (1995–2003) during flybys of Europa. The *Galileo* spacecraft orbited Jupiter and made close passes of the Galilean moons, measuring, among many other features, the magnetic signatures of the moons' interactions with Jupiter's magnetosphere, properties of various charged particle populations, and images of the surface. Though *Galileo* made many important discoveries, the mission was hindered by a problem with the high-gain antenna that prevented much of the data from being transmitted back to Earth; as a result, the data are more limited than was expected.

Here we review the observations and datasets that are relevant to this dissertation.

1.2.1 Magnetic field

The *Galileo* magnetometer observations underpin every model for the plasma interaction. From December 1996 to January 2000 the spacecraft conducted flybys of Europa, resulting in eight magnetic field datasets collected during the E4, E11, E12, E14, E15, E17, E19, and E26 flybys. Each flyby passes through the plasma interaction on a different trajectory. Europa's position within Jupiter's magnetosphere and the moon's orbital phase also vary with each flyby. Kivelson et al. (2009) provides the most recent comprehensive review of the *Galileo* magnetometer data.

1.2.2 Bulk plasma parameters

The *Galileo* spacecraft also observed the thermal plasma at Europa with the Plasma Subsystem (PLS). Paterson et al. (1999) report the total ion density and bulk ion velocity

components for thermal ions during the E4 and E6 flybys. They found that the density of the thermal magnetospheric plasma at Europa was ~20 cm^{-3}, while the speed of the plasma relative to the moon was ~100 km s^{-1}. No other PLS observations were published by the *Galileo* team. However, there have been efforts in recent years to process the data and recover plasma moments for other flybys (e.g., Collinson et al., 2018 and Huybrighs, 2018).

The *Galileo* spacecraft also carried a plasma waves instrument (PWS). By analyzing the upper hybrid resonance frequencies observed during the flybys, Kurth et al. (2001) derived electron densities along the flyby trajectories. They determined that the electron density near Europa ranged from 30-200 cm^{-3} during the *Galileo* flybys.

Bagenal et al. (2015) synthesized multiple datasets to model the magnetospheric plasma at Europa's orbit. They determined how the density and temperature of magnetospheric plasma at Europa should vary both with Europa's System-III longitude (see Appendix A) and with the global state of Jupiter's magnetosphere.

Recently, JAXA's Hisaki telescope has undertaken campaigns of continuous observation of the Io plasma torus (see, for example, Yoshioka et al., 2018). While these observations do not provide plasma bulk parameters at Europa, they are informative for understanding the periodic variations of the Jovian plasma sheet due to Jupiter's rotation, as well as variations caused by volcanic activity at Io.

1.2.3 Ionosphere

The *Galileo* mission also conducted radio occultation experiments to measure electron density altitude profiles. Kliore et al. (1997) first reported these results, which were subsequently collected, updated, and published by McGrath et al. (2009). The radio occultations produced 10 altitude profiles of electron density in Europa's ionosphere, sampling different locations over

Europa's surface, and were conducted during different flybys. The highest density observed is ~12500 cm^{-3} and occurs below 50 km in altitude. Other profiles registered much lower densities (<2500 cm^{-3}) at all altitudes. All together, the radio occultation measurements suggest that Europa's ionosphere exhibited significant spatial and temporal variation during the *Galileo* mission era.

1.2.4 Atmosphere and potential water plumes

Observational constraints on the composition, shape and structure of Europa's atmosphere are principally derived from Hubble Space Telescope (HST) observations of Europa's oxygen aurora. Hall et al. (1995) and Hall et al. (1998) determined that the composition of Europa's atmosphere is dominated by O_2, and that during the HST observations conducted in 1994 and 1996 the column density of the atmosphere ranged from $(2.4\text{-}20)\times10^{14}$ cm^{-2}. Roth et al. (2016) analyzed new observations by the HST that were conducted from 2012-2015, confirming the previous results. As the new measurements were superior in spatial resolution, Roth et al. (2016) also tentatively estimated the scale height of the atmosphere to be ~100 km. A recent review by Plainaki et al. (2018) summarizes these results, and others, in more detail.

In recent years Europa has been the subject of significant interest due to several possible detections of water plumes. Roth et al. (2014) and Sparks et al. (2016) analyzed HST data using two different techniques, both of which reported results consistent with water plumes in Europa's southern high latitudes. Most recently, Paganini et al. (2019) identified a direct measurement of water vapor in Europa's atmosphere with the near-infrared spectrograph at the Keck Observatory. These observations have inspired researchers modeling Europa's plasma interaction to consider the effects of atmospheric inhomogeneities associated with water plumes on Europa's plasma interaction (Blöcker et al., 2016; Jia et al., 2018; Arnold et al., 2019, 2020).

1.3 Modeling Europa's plasma interaction

1.3.1 The multi-fluid magnetohydrodynamic approach

Magnetohydrodynamics (MHD) is a method of modeling magnetized plasmas as a charged fluid. In brief, the MHD approach requires solving the set of fluid transport equations derived from the first three moments of the Boltzmann equation together with Maxwell's equations for electromagnetic fields. The equations are closed and simplified by making various approximations. Computational models based on the MHD approach are ubiquitous in the study of space plasmas throughout the solar system because MHD models are well-suited for efficiently solving the bulk properties (density, velocity, pressure) of space plasmas self-consistently with the local perturbations to the magnetic field caused by currents that flow in the plasma (Toth et al., 2012).

A system of space plasmas can be represented by MHD when the length and time scales that describe the interaction are long compared to the Larmor radius of the charged particles in the local magnetic field. At Europa the relevant scales for the system are the radius of Europa itself (1 R_{Eu} = 1560 km) and the time required for magnetospheric plasma to flow past the interaction region around the moon, which extends at least a few Europa radii (> 5 R_{Eu}) along the ambient flow direction in the upstream and the downstream. At a relative velocity of ~100 km/s, this transit time across the interaction region is at least 150 seconds. The relevant scales for charged particles in a magnetic field are the period of cyclotron motion and the Larmor radius of the dominant ion species. The period of cyclotron motion for magnetospheric O^+ in the Jovian magnetic field at Europa's orbit (~400 nT) is 2.6 seconds. The Larmor radius for a ~100 eV O^+ ion in the same environment is 14 km. Thus, it is appropriate to represent Europa's plasma interaction with MHD.

In ideal MHD, the ensemble of ions and electrons that forms a plasma is represented by one fluid. However, as we have seen above, Europa's plasma interaction is a system of multiple plasma populations with different sources, weights, charges, and energies. We can extend the system of equations to model multiple MHD fluids simultaneously and separately determine the mass, velocity, and pressure associated with different populations of ions and electrons. This approach is known as multi-fluid MHD. Though adding multiple MHD fluids increases the complexity of the model, at Europa the benefits of modeling the interactions between different plasma fluids can outweigh the increased computational cost.

1.3.2 Advances in computational models for Europa's plasma interaction

Numerous computational models for Europa's plasma interaction have been developed during and since the *Galileo* mission. By responding to new discoveries and testing new ideas, simulations have shaped our understanding of how each of the observations described above fit together as a unified system. Here we trace the recent history of computational models pertinent to this dissertation; more comprehensive reviews have been conducted by Plainaki et al. (2018) and Bagenal and Dols (2020).

Saur et al. (1998) developed a fluid model for the plasma interaction that balanced the mass exchanged through ionization and recombination processes between Europa's atmosphere and ionosphere in uniform magnetic fields. They varied the density of Europa's atmosphere in the simulations, calculated the rates at which mass was added and lost from the atmosphere, and identified the atmosphere that produced the most balanced state. Saur et al. (1998) went on to characterize properties of the ionosphere, such as electron density, currents, and conductance, for this case. They determined that a plasma wake forms downstream of the moon due to diversion

by the plasma interaction and characterized how this diversion increases with the column density of the neutral atmosphere.

Kivelson et al. (2000) presented definitive proof for Europa's time-variable induced magnetic field, adding a new element to the plasma interaction. Schilling et al. (2007, 2008) used single-fluid MHD to self-consistently model the electromagnetic fields and plasma properties of Europa's plasma interaction, with particular attention to understanding the generation and implications of Europa's induced field. The authors implemented the conductivity model developed by Zimmer et al. (2000) for Europa's differentiated interior. In addition to the magnetic field induced by the interaction of the magnetospheric magnetic field with Europa's ocean, the authors calculated the induced fields caused by time-variation of the plasma interaction magnetic fields, and the effect of these fields on determining the properties of the subsurface ocean.

Hybrid models that represent electrons with a charged fluid and ions as charged particles have been applied to Europa's plasma interaction (e.g., Lipatov et al., 2010 and Arnold et al., 2019). As we have described above, Europa is subjected to bombardment by different ion species from Jupiter's magnetosphere. Hybrid models' kinetic approach to ions permits the study of the different roles of these distinct ion species that form the Jovian thermal magnetospheric plasma in the plasma interaction. Lipatov et al. (2010, 2013) implemented this approach and identified the effects of different compositions for the ambient magnetospheric ions. They also incorporated recent results of modeling of Europa's atmosphere (Cassidy et al., 2007) by implementing an atmosphere with two populations: cold O_2 with a scale height of 200 km and thermal O_2 with a scale height of 30 km.

Rubin et al. (2015) implemented multi-fluid MHD with two ion fluids, one representing the combined O^+ of Jupiter's magnetosphere and Europa's ionosphere, and the second representing the O_2^+ of Europa's ionosphere. By coupling the ion fluids to Europa's neutral atmosphere through source and loss processes representing the effects of ionization, recombination, and charge exchange, Rubin et al. (2015) self-consistently solved the multi-fluid MHD equations for the steady state bulk plasma properties and magnetic fields of the plasma interaction during the E4 and E26 flybys. Rubin et al. (2015) also incorporated the results of Cassidy et al. (2007, 2013) to prescribe a realistic, though static, neutral O_2 atmosphere. The results of Rubin et al. (2015) exhibited asymmetries on the anti- and sub-Jovian hemispheres in the distribution of plasma impinging on Europa's surface that had not been observed in single-fluid MHD simulations. The authors also presented maps of the flux of precipitating plasma onto the surface. The good data-model comparison between these simulations and the *Galileo* datasets set the standard for modeling of Europa's plasma interaction.

Blöcker et al. (2016) used single-fluid MHD to self-consistently model the electromagnetic fields and plasma properties of Europa's plasma interaction. Their investigation focused on the effects of localized inhomogeneities in the neutral atmosphere, such as could be caused by water plumes, on Europa's plasma interaction. They found that such localized neutral inhomogeneities created strong electromagnetic disturbances that formed Alfvén winglets within the larger Alfvén wings caused by the presence of Europa's ionosphere. In particular, they simulated several *Galileo* flybys and determined that the magnetic field perturbations observed during the E26 flyby could be consistent with the presence of a water plume.

Jia et al. (2018) subsequently applied the Rubin et al. (2015) two-ion-fluid model to identify signatures of a water plume in *Galileo* magnetometer and plasma wave data from the

E12 flyby. Jia et al. (2018) re-analyzed the *Galileo* magnetic field and plasma wave data and identified short-duration (several minutes) signatures consistent with perturbations generated by a plume in interaction with the Jovian plasma.

Arnold et al. (2019) applied a hybrid model to simulate the *Galileo* E26 flyby, supporting the findings of Blöcker et al. (2016) that a plume could have caused some of the magnetic field perturbations observed at the spacecraft. Arnold et al. (2020) then conducted a systematic study to characterize the effects of a water plume as one might be observed by a spacecraft. They conducted several simulations with different atmosphere configurations and extracted data along hypothetical spacecraft trajectories. Their results illustrate how the detectability of a plume at Europa is influenced by the proximity with which it is encountered by a spacecraft as well as by the state of the base neutral atmosphere.

1.4 Outstanding questions

Since the end of the *Galileo* mission in the early 2000s, there have been no new *in situ* observations of Europa's plasma interaction. Remote observations by Earth-based telescopes, namely, the HST, JAXA's Hisaki telescope, and the Keck observatory, have made tantalizing new observations with implications for Europa's atmosphere, but to understand the effects on the plasma interaction requires simultaneous, co-located observations of the plasmas and electromagnetic fields. NASA's *Juno* spacecraft will make one close pass of Europa in 2022. However, the most anticipated, extensive new data on Europa will be collected by the *Europa Clipper* mission in the 2030s. This leaves a gap of several decades with no new *in situ* data.

In the previous section we discussed several of the computational models that have been developed to continue the study of Europa in the wake of the *Galileo* mission. In the 2000s, much progress was made by incorporating the discoveries made possible by the *Galileo* mission.

Simultaneously, improvements were made to models for Europa's atmosphere that then informed the plasma interaction models developed in the 2010s. In light of remote observations that raised the possibility of water plumes at Europa in 2014, many studies of the plasma interaction then focused on the effects of these possible plumes, and searched for evidence of them in the *Galileo* datasets.

The significant progress made in recent decades highlights the benefits of incorporating more realistic models for Europa's atmosphere into plasma interaction models. However, there are still significant gaps in understanding the coupling between Europa's atmosphere and plasma interaction, and the role of Jovian magnetospheric plasma in that coupling. The research undertaken for this dissertation addresses these gaps. For instance, atmospheric models suggest that the generation of the atmosphere depends in part on sputtering caused by the precipitation of thermal magnetospheric plasma (Cassidy et al., 2013; Vorburger and Wurz, 2018). **Chapter 3** of this dissertation presents the results of a parameter study to characterize this precipitation and identify how it varies with magnetospheric conditions. Furthermore, models for Europa's atmosphere have indicated that the base atmosphere may be variable due to the effects of solar illumination (Plainaki et al., 2013; Oza et al., 2019); these expected variations are tested in **Chapter 4**. In **Chapter 5** of this dissertation, the effects of nominal variations in Europa's atmosphere on the plasma interaction, and on the precipitation of thermal plasma, are investigated further.

By closing these gaps, this dissertation improves our understanding of how Europa's plasma interaction depends on the conditions of Jupiter's magnetosphere, and on Europa's own atmosphere. The results of this research provide inputs and identify trends that should be

accounted for in future models for Europa's atmosphere. In brief, this research lays the groundwork for modeling Europa's space environment as a unified, connected system.

1.5 Outline of the dissertation

In **Chapter 2** we introduce a multi-fluid magnetohydrodynamic (MHD) model, developed based on that of Rubin et al. (2015), that simulates the major plasma populations at Europa and self-consistently solves for perturbations to the local electromagnetic fields. The most significant advance made for this new model is the addition of a new ion fluid to separately model thermal magnetospheric plasma. We verify the model by simulating the plasma interaction during the E4 and E14 flybys conducted by the *Galileo* mission. In **Chapter 3** we apply the model to characterize variability in Europa's plasma interaction caused by natural periodicities in the magnetic field and plasma conditions of Jupiter's magnetosphere. In **Chapter 4**, we consider a case study of the *Galileo* E15 flyby that exemplifies the effects of the internal state of Europa's atmosphere on the plasma interaction. To better understand the role of the atmosphere and the effects of variations in atmosphere density and scale height on the plasma interaction, in **Chapter 5** we present the results of a new parameter study within which parameters of the atmosphere were varied. **Appendix A** summarizes the different coordinate systems used to make sense of various datasets throughout this dissertation.

Chapter 2 The Multi-Fluid Magnetohydrodynamic Model for Europa's Plasma Interaction

Our model is based on that of Rubin et al. (2015), in which the authors used the multi-fluid capabilities of the BATS-R-US magnetohydrodynamic (MHD) code (Toth et al., 2012; Glocer et al., 2009) to self-consistently solve for the electromagnetic fields and bulk plasma properties of Europa's plasma interaction. Rubin et al. (2015) generated Europa's ionosphere from a static distribution of neutral O_2 by including mass, momentum, and pressure sources in the multi-fluid MHD equations for two ion fluids: a fluid representing O_2^+ originating in Europa's ionosphere, and a combined magnetospheric and ionospheric O^+ fluid. They also included an electron fluid. We have made improvements to the performance of the model, expanded the simulation domain, increased the grid resolution, and used a more accurate scheme to solve the model equations. The most significant improvement from the model of Rubin et al. (2015) is that our new model has separated Jupiter's magnetospheric O^+ ions from those generated by ionization of Europa's atmosphere.

In our new model we solve the steady-state multi-fluid MHD equations for three ion fluids and one electron fluid so that we can separately track the O^+ ions of ionospheric and magnetospheric origin. The first ion fluid represents magnetospheric O^+ which flows past Europa from the upstream outer boundary. Though S^{2+} is also a significant component of the thermal magnetospheric plasma population at Europa's orbit (e.g. Kivelson et al., 2004), the mass-to-charge ratio of S^{2+} is identical to that of O^+, and the ion species share bulk flow properties and

both originate from the Io plasma torus. Therefore, we did not include S^{2+} as an additional fluid in our simulations in order to reduce computational demand.

The second and third ion fluids represent O_2^+ and O^+ ions that are generated from Europa's O_2-dominated atmosphere through electron impact ionization, photoionization, and charge exchange. These fluids together form Europa's ionosphere and an extended region of pick-up ions around the moon. Ions may be lost as they leave the simulation's downstream outer boundary, by absorption to Europa's surface, or they may recombine with electrons to become neutrals. Separating the magnetospheric and ionospheric O^+ ions is critical because their bulk properties (density, velocity, and temperature) are very different even in the same volume of the space plasma environment around Europa.

The 3-ion-fluid model retains most of the features of the previous 2-ion-fluid model described in Section 2 of Rubin et al. (2015). In **Sections 2.1-2.5** of this chapter we describe the governing equations, the source and loss terms representing mass-loading and momentum-loading processes at Europa, the boundary conditions, the parameters of the neutral atmosphere, as well as the updates we have made to the numerical aspects of the model. Cartesian coordinates and vector quantities are given in the Europa-centric EPhiO coordinate system, in which X points in the flow direction of Jupiter's corotating plasma, Y points towards Jupiter, and Z is parallel to Jupiter's spin axis (for further description of this coordinate system, see **Appendix A.2**). We finish the chapter by presenting the results of two simulations modeling the *Galileo* E4 and E14 flybys in **Section 2.6**. These results verify that our model accurately represents Europa's plasma interaction.

2.1 Model equations

The multi-fluid MHD model solves the steady-state ion continuity equations,

$$\frac{\partial \rho_s}{\partial t} + \nabla \cdot (\rho_s \vec{u}_s) = \frac{\delta \rho_s}{\delta t} \tag{2.1}$$

the ion momentum equations,

$$\frac{\partial (\rho_s \vec{u}_s)}{\partial t} + \nabla \cdot \left(\rho_s \vec{u}_s \vec{u}_s + \bar{I} p_s\right) - Z_s e \frac{\rho_s}{m_s}\left(\vec{E} + \vec{u}_s \times \vec{B}\right) - \rho_s \vec{g} = \frac{\delta (\rho_s \vec{u}_s)}{\delta t} \tag{2.2}$$

and the ion and electron pressure equations.

$$\frac{\partial p_s}{\partial t} + (\vec{u}_s \cdot \nabla) p_s + \gamma p_s (\nabla \cdot \vec{u}_s) = \frac{\delta p_s}{\delta t} \tag{2.3}$$

$$\frac{\partial p_e}{\partial t} + (\vec{u}_e \cdot \nabla) p_e + \gamma p_e (\nabla \cdot \vec{u}_e) + (\gamma - 1) \nabla \cdot \vec{h}_e|_{\|B} = \frac{\delta p_e}{\delta t} \tag{2.4}$$

In **Equations 2.1-5** the symbols ρ_s, u_s, p_s, Z_s, and m_s are respectively the mass density, bulk velocity, thermal pressure, charge state, and mass of ion fluid *s*, where *s* indicates any of the three ion fluids described above (or with subscript *e* for electrons in **Equation 2.4**). The symbol *e* indicates the elementary charge. The symbols $\vec{E}$, $\vec{B}$, and $\vec{j}$ give the electric field, magnetic field, and electric current density, respectively. In **Equation 2.2** the symbols $\bar{I}$ and $\vec{g}$ refer respectively to the identity matrix and the acceleration due to gravity. In **Equations 2.3 and 2.4** the symbol γ indicates the adiabatic index.

The electric field is given by the generalized Ohm's law.

$$\vec{E} = -\vec{u}_e \times \vec{B} - \frac{1}{n_e e} \nabla p_e + \eta \vec{j} \tag{2.5}$$

In **Equation 2.5** we include resistivity η to represent the effects of collisions between electrons and neutrals, as well as collisions between electrons and ions, on the electric field. The parameter n_e gives the electron number density, which is derived as follows assuming quasi-neutrality between the electrons and the ion fluids.

$$n_e = \sum_s Z_s n_s \tag{2.6}$$

In **Equation 2.6** n_s gives the number density of each ion fluid. The vector $\vec{u}_e$ gives the electron bulk velocity, which is calculated as the sum of the charge-averaged velocity ($\vec{u}_q$) and the Hall velocity ($\vec{u}_H$).

$$\vec{u}_e = \vec{u}_q + \vec{u}_H = \frac{\sum_s Z_s n_s \vec{u}_s}{n_e} - \frac{\vec{j}}{n_e e} \tag{2.7}$$

The terms $\delta\rho_s/\delta t$, $\delta(\rho_s u_s)/\delta t$, $\delta p_s/\delta t$, and $\delta p_e/\delta t$ in **Equations 2.1-4** are the net sources of mass, momentum, and pressure for the ion and electron fluids. They represent the effects of photoionization, electron impact ionization, recombination, charge exchange, and collisions; the implementations of these source terms are described in **Section 2.3**. These terms are responsible for the generation of the ionosphere, as well as the coupling in momentum and energy between the ion fluids, electrons, and neutrals.

The fourth term on the left-hand side of **Equation 2.4** describes field-aligned electron heat conduction as implemented by Rubin et al. (2015). This term permits heat to be transferred among the electrons along the direction of the magnetic field lines in the simulation. This feature allows us to include the energy input from the Io plasma torus through the simulation outer

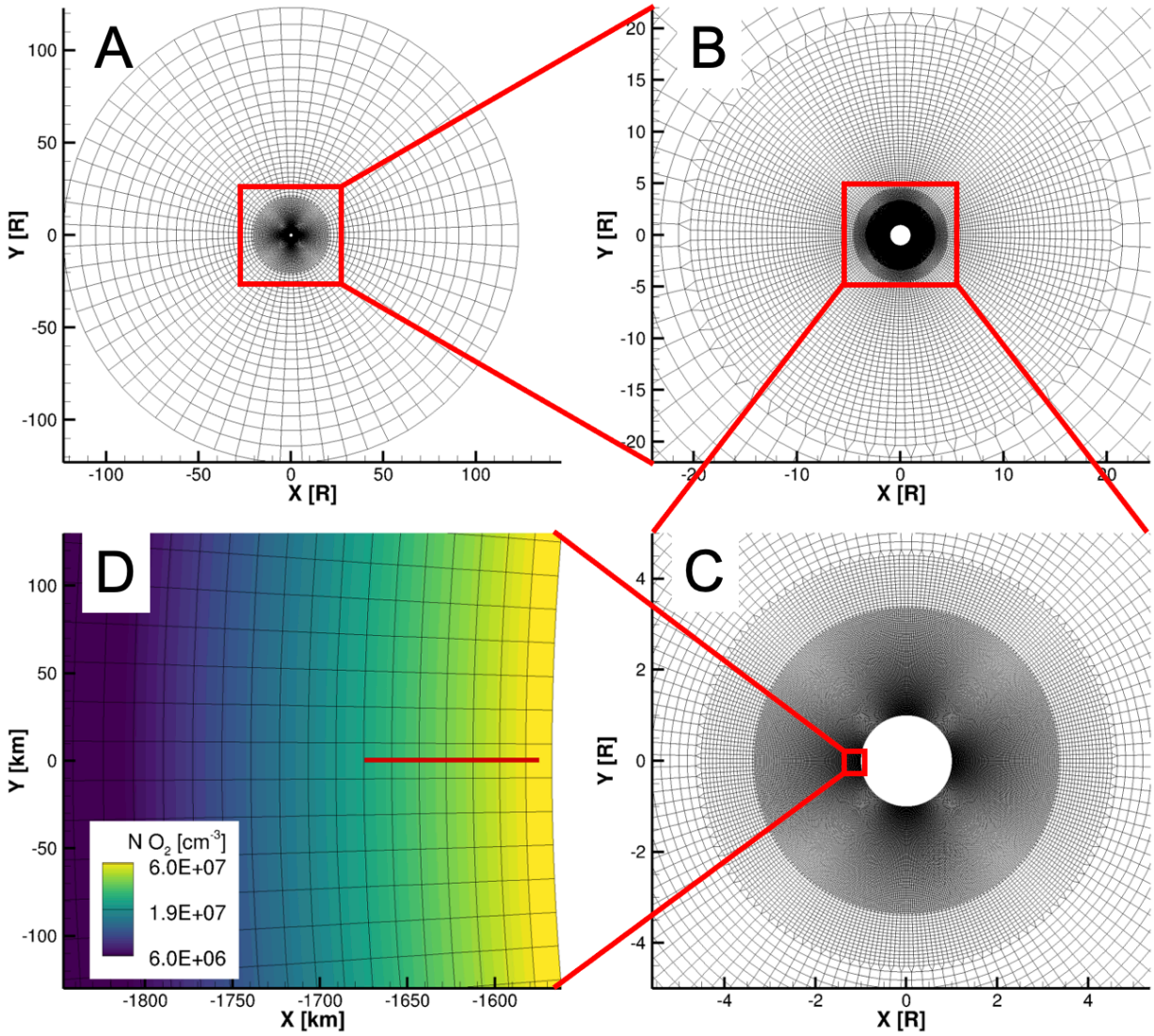

Figure 2.1: The simulation grid in the Z=0 plane shown in successively smaller scales. Panel A shows the whole simulation space extending from R=1-64 R_{Eu}. Panel B shows the first layer of grid refinement at R=20 R_{Eu}; Panel C shows the second and third layers of refinement at R=4 R_{Eu} and R=3 R_{Eu}. Panel D shows the cells closest to Europa's surface on the upstream side of the plasma interaction, and includes the density of the atmosphere in color contours. In Panel D a red bar indicates the 100 km scale height of the atmosphere.

boundary, which is important for obtaining a realistic calculation of the electron impact ionization rate.

The evolution of the magnetic field is given by solving Faraday's law of induction.

$$\frac{\partial \vec{B}}{\partial t} = -\nabla \times \vec{E} \tag{2.8}$$

Using **Equations 2.5** and **2.7**, **Equation 2.8** can be rewritten as the magnetic induction equation:

$$\frac{\partial \vec{B}}{\partial t} = \nabla \times \left(\underbrace{\vec{u}_q \times \vec{B}}_{\text{convection}} - \underbrace{\frac{\vec{J}}{n_e e} \times \vec{B}}_{\text{Hall}} + \underbrace{\frac{1}{n_e e} \nabla p_e}_{\text{electron pressure}} - \underbrace{\eta \vec{J}}_{\text{resistivity}} \right) \tag{2.9}$$

The terms on the right-hand side of **Equation 2.9** are the convection term, the Hall term, the electron pressure gradient term, and the resistivity term. The Hall term was not included in our simulations to reduce computational demand to make it feasible to run a large number of simulations. Accordingly, in **Equation 2.7** we set $\vec{u}_H$=0, such that in the simulations the velocity of the electrons is given by the charge-averaged velocity. However, the differential speed between ions and electrons is accounted for in the source and loss terms described in **Section 2.3**.

2.2 Numerical aspects

We solve the multi-fluid MHD equations on a non-uniform spherical grid, shown in **Figure 2.1**. The grid is logarithmically stretched in the radial dimension and block-adaptive grid refinement is used to increase the resolution in the near-Europa region. The simulation domain extends from R = 1 to 128 R_{Eu} (where Europa's mean radius is 1 R_{Eu} = 1570 km). The smallest cell size near the simulation inner boundary just above Europa's surface is typically ~0.01 R_{Eu} = 15 km, while the largest cells at the outer boundary are ~10 R_{Eu} = 15700 km in size.

To obtain steady-state solutions to the MHD equations, the model solves them using a second-order Linde scheme (for details of the scheme implementation in BATS-R-US see Toth et al., 2012).

2.3 Source and loss terms

Section 2.4 of Rubin et al. (2015) gives a detailed description of the implementation of source and loss terms that model the effects of ionization, recombination, and charge exchange on the multi-fluid mass, momentum, and pressure MHD equations. Here we review that discussion and address the updates we have made. **Table 2.1** summarizes the chemical processes represented by these sources and losses.

Table 2.1: Chemical processes represented in the model. For each process the corresponding reference from which the reaction rates were implemented is given. Note that while O is referenced in the reactions for completeness, the model does not include neutral O. Note also that while O_2 is consumed and produced by these reactions, in the model the O_2 density is not modified.

Name	Reaction	Model fluids affected	Reference
Electron impact ionization	$O_2 + e^- \rightarrow O_2^+ + 2e^-$	O_2^+, electrons	Schilling (2006)
	$O_2 + e^- \rightarrow O_{\text{iono}}^+ + O + 2e^-$	Iono. O^+, electrons	
Photoionization	$O_2 + h\nu \rightarrow O_2^+ + e^-$	O_2^+, electrons	Huebner et al. (1992)
	$O_2 + h\nu \rightarrow O_{\text{iono}}^+ + O + e^-$	Iono. O^+, electrons	
Charge exchange	$O_2 + O_2^+ \rightarrow O_2^+ + O_2$	O_2^+	Schunk and Nagy (2009)
Recombination	$O_{\text{mag}}^+ + e^- \rightarrow O$	Mag. O^+, electrons	Schunk and Nagy (2009)
	$O_2^+ + e^- \rightarrow O + O$	O_2^+, electrons	
	$O_2^+ + e^- \rightarrow O_2$	O_2^+, electrons	
	$O_{\text{iono}}^+ + e^- \rightarrow O$	Iono. O^+, electrons	

The sources of mass for each ion fluid (right hand side of **Equation 2.1**) are as follows:

$$\frac{\delta \rho_s}{\delta t} = \underbrace{m_s \nu_{n\to s}^{\mathrm{io}} n_n}_{1} - \underbrace{m_s \sum_{s'} n_n n_s k_{ns\to ns'}}_{2} + \underbrace{m_s \sum_{s'} n_n n_{s'} k_{ns'\to ns}}_{3} - \underbrace{m_s \alpha_s n_e n_s}_{4} \tag{2.10}$$

In **Equation 2.10** the subscripts s and s' refer to the three ion fluids, the subscript *n* refers to neutral O_2, and subscript *e* refers to electrons. The symbol $\nu_{n\to s}^{\mathrm{io}}$ gives the combined electron impact and photoionization rate; this rate is zero for the magnetospheric O^+ fluid (see **Section 2.3.1**). The symbol $k_{ns\to ns'}$ refers to charge exchange between the ion fluids and neutrals (see **Section 2.3.2**). In our model we consider only resonant charge exchange between O_2 and O_2^+, and therefore *k* is zero for other values of s or s'. The symbol α_s gives the ion-electron recombination rates (see **Section 2.3.3)**. Therefore, in **Equation 2.10** term 1 gives the mass added to each ion fluid by ionization of neutral O_2, term 2 gives the mass lost by charge exchange, term 3 gives the mass gained by charge exchange, and term 4 gives the mass lost to recombination. Term 1 is active only for the ionospheric fluids, terms 2 and 3 together sum to zero and apply only to the O_2^+ fluid, and term 4 applies to all the ion fluids.

The sources of momentum for each ion fluid (right hand side of **Equation 2.2**) are as follows:

$$\begin{aligned}\frac{\delta \rho_s \vec{u}_s}{\delta t} = {} & \underbrace{m_s \nu_{n\to s}^{\mathrm{io}} n_n (\vec{u}_n - \vec{u}_s)}_{1} + \underbrace{m_s n_n \sum_{s'} n_{s'} k_{ns'\to ns} (\vec{u}_n - \vec{u}_s)}_{2} - \underbrace{m_s \bar{\nu}_{se} n_s (\vec{u}_s - \vec{u}_e)}_{3} \\ & + \underbrace{m_s n_s \sum_{s'} \bar{\nu}_{ss'} (\vec{u}_{s'} - \vec{u}_s)}_{4} + \underbrace{m_s n_s \bar{\nu}_{sn} (\vec{u}_n - \vec{u}_s)}_{5} + \underbrace{\frac{\delta \rho_s}{\delta t} \vec{u}_s}_{6}\end{aligned} \tag{2.11}$$

In **Equation 2.11** the symbols $\bar{\nu}$ with different subscripts refer to elastic momentum transfer collision rates between the ions, electrons, and neutrals as indicated by the subscripts *s*, *e*, and *n*. Term 1 gives the momentum added by newly ionized neutrals and term 2 gives the momentum added by the mass added through charge exchange. Terms 3, 4, and 5 give, respectively, the momentum exchanged with electrons, with other ions, and with neutrals through elastic collisions. Term 6 gives the momentum change due to the net change in mass (**Equation 2.10**).

The sources of pressure for each ion fluid (right hand side of **Equation 2.3**) are as follows:

$$\begin{aligned}\frac{\delta p_s}{\delta t} = &\underbrace{-p_s \sum_{s'} n_n n_s k_{ns\to ns'}}_{1} \underbrace{- p_s \alpha_s n_e}_{2} + \underbrace{2\sum_{s'} \bar{\nu}_{ss'} \frac{m_s}{m_{s'}+m_s} n_s k_B (T_{s'} - T_s)}_{3} \\ &+ \underbrace{\frac{2}{3}\sum_{s'} \bar{\nu}_{ss'} \frac{m_s m_{s'}}{m_{s'}+m_s} n_s (\vec{u}_{s'} - \vec{u}_s)^2}_{4} + \underbrace{2\bar{\nu}_{sn} \frac{m_s}{m_n+m_s} n_s k_B (T_n - T_s)}_{5} \\ &+ \underbrace{\frac{2}{3}\bar{\nu}_{sn} \frac{m_s m_n}{m_n+m_s} n_s (\vec{u}_n - \vec{u}_s)^2}_{6} + \underbrace{2\bar{\nu}_{se} n_s k_B (T_e - T_s)}_{7} + \underbrace{\frac{2}{3}\bar{\nu}_{se} m_e n_s (\vec{u}_e - \vec{u}_s)^2}_{8} \\ &+ \underbrace{\frac{1}{3} m_s \nu^{\mathrm{io}}_{n\to s} n_n (\vec{u}_n - \vec{u}_s)^2}_{9} + \underbrace{\frac{1}{3} m_s \sum_{s'} n_n n_{s'} k_{ns'\to ns} (\vec{u}_n - \vec{u}_s)^2}_{10}\end{aligned} \tag{2.12}$$

Here we assume an adiabatic index of $\frac{5}{3}$. Terms 1 and 2 give the loss of pressure due, respectively, to mass lost by charge exchange and ion-electron recombination. Terms 3-8 account for changes in pressure caused by elastic momentum transfer collisions between ions, electrons, and neutrals; these terms depend on the masses of the participating particles and tend to equilibrate the temperatures and bulk velocities between them. Our treatment of these collision terms is identical to Rubin et al. (2015), with the same rates applied for the magnetospheric and ionospheric O^+ fluids. The collision terms depend on the masses of the participating particles

such that $\bar{\nu}_{ss'} \neq \bar{\nu}_{s's}$. Terms 9 and 10 account, respectively, for pressure added by mass added by ionization and charge exchange.

The sources of pressure for the electron fluid (right hand side of **Equation 2.4**) are as follows:

$$\frac{\delta p_e}{\delta t} = \underbrace{-p_e n_e \sum_s \alpha_s n_s}_{1} + \underbrace{\frac{1}{3} m_e \sum_s \nu_{n\to s}^{\mathrm{io}} n_n (\vec{u}_n - \vec{u}_e)^2}_{2} + \underbrace{\frac{2}{3} \sum_s \nu_{n\to s}^{\mathrm{io,ph}} n_n Q_{n\to s}^{\mathrm{exc}}}_{3}$$
$$\underbrace{-\frac{2}{3} \sum_s n_e \nu_{n\to s}^{\mathrm{io,e}} n_n Q_{n\to s}^{\mathrm{pot}}}_{4} + \underbrace{2 \sum_s \bar{\nu}_{es} \frac{m_e}{m_s} n_e k_B (T_{s'} - T_e)}_{5}$$
$$\underbrace{+\frac{2}{3} \sum_s \bar{\nu}_{es} m_e n_e (\vec{u}_{s'} - \vec{u}_e)^2}_{6} + \underbrace{2 \bar{\nu}_{en} \frac{m_e}{m_n} n_e k_B (T_n - T_e)}_{7} + \underbrace{\frac{2}{3} \bar{\nu}_{en} m_e n_e (\vec{u}_n - \vec{u}_e)^2}_{8} \tag{2.13}$$

The symbols $\nu_{n\to s}^{\mathrm{io,ph}}$ and $\nu_{n\to s}^{\mathrm{io,e}}$ refer to the separate photoionization and electron impact ionization rates, respectively (**Section 2.3.1**). The symbols $Q_{n\to s}^{\mathrm{exc}}$ and $Q_{n\to s}^{\mathrm{pot}}$ refer, respectively, to the excess energy of photoelectrons and the potential energy supplied to electron impact ionization by magnetospheric electrons. Term 1 gives the reduction in electron pressure by ion-electron recombination. Term 2 accounts for the electrons added by electron impact ionization. Terms 3 and 4 respectively account for the energy added by photoelectrons and the energy lost to electron impact ionization. Terms 5-8 account for the energy transferred through elastic momentum transfer collisions.

2.3.1 Electron impact ionization and photoionization

We have updated the calculation of the electron impact ionization rate to include ionization by suprathermal electrons from the Io plasma torus. We fix the temperature of the electron fluid to 20 eV, the typical temperature of thermal electrons near Europa (Bagenal and

Dols, 2020), at the outer boundaries of the simulation domain. Perturbations to this temperature then develop self-consistently in our multi-fluid simulation according to the electron pressure equation (**Equation 2.4**) which includes the effects of the electron pressure source terms and field-aligned electron heat conduction.

We use the method of Schilling (2006) and Rubin et al. (2015) to calculate the electron impact ionization rate for the ionospheric O_2^+ fluid based on the temperature of the thermal electron MHD fluid. We integrate the product of the normalized Maxwellian energy distribution, the electron impact ionization cross section ($\sigma_{n\to s}$) via Hwang et al. (1996), and the speed of the electrons over the energy of the electrons.

$$\nu_{n\to s}^{\mathrm{io,e}} = \int_{Q_{n\to s}^{\mathrm{pot}}}^{\infty} f_e(E, T_e)\sigma_{n\to s}(E)v_e(E)\, dE \tag{2.14}$$

Here the Maxwell-Boltzmann energy distribution is $f_e(E, T_e) = 2\sqrt{\frac{E}{\pi}}\left(\frac{1}{k_B T_e}\right)^{\frac{3}{2}} \exp\left(\frac{-E}{k_B T_e}\right)$. The speed of an electron with energy E is $v_e(E) = \sqrt{2E/m_e}$. The integration lower bound $Q_{n\to s}^{\mathrm{pot}}$ ensures that only electrons with sufficient energy contribute to electron impact ionization; for ionization of O_2^+, $Q_{n\to s}^{\mathrm{pot}}$ =12.0 eV while for O^+ $Q_{n\to s}^{\mathrm{pot}}$ =18.8 eV (Samson and Gardner, 1975).

We then add a uniform electron impact ionization rate that is calculated by evaluating **Equation 2.14** for the suprathermal population of electrons with low density (2 cm^{-3}) and high temperature (250 eV) that originate from the Io plasma torus (Bagenal and Dols, 2020), after the method of Saur et al. (1998). We estimate the ionospheric O^+ electron impact ionization rate to be 10% of the O_2^+ rate (Rubin et al., 2015). In the *Galileo* flyby simulations, the average O_2^+ electron impact ionization rate over all the grid cells within 200 km of Europa's surface is 1.1×10^{-6} s^{-1}.

We apply the photoionization frequencies by Huebner et al. (1992) and scale them to Jupiter's orbit at 5.2 AU such that the frequency is 1.70×10^{-8} s^{-1} for O_2^+ and 4.07×10^{-9} s^{-1} for O^+. The excess energy associated with the photoelectrons ($Q_{n\to s}^{\mathrm{exc}}$) is 16 eV and 32 eV respectively for photoionization that produces O_2^+ and O^+.

Photoionization is applied uniformly over the whole simulation domain instead of being excluded from Europa's shadow as in Rubin et al. (2015). We found that the shadow made little difference in the steady state solution as the photoionization rate is 2 orders of magnitude lower than the electron impact ionization rate.

2.3.2 Charge exchange

We include resonant charge exchange between O_2 and O_2^+. The rate given by Schunk and Nagy (2009) for this reaction (see Table 4.5 therein), where subscript *n* refers to O_2 and *s* refers to O_2^+, is (in units of m^3s^{-1}, with temperatures T_n, T_s in units of Kelvin):

$$k_{ns\to ns} = 2.59\times10^{-17} n_n \sqrt{\frac{T_n+T_s}{2}}\left(1-0.073\cdot\log_{10}\left(\frac{T_n+T_s}{2}\right)\right)^2 \tag{2.15}$$

2.3.3 Recombination

We implement dissociative ion-electron recombination for all three ion fluids in the model using the rates given by Schunk and Nagy (2009). We apply the same recombination rate to magnetospheric and ionospheric O^+: $\alpha_{O^+} = 3.7\times10^{-18}\left(\frac{250}{T_e}\right)^{0.7}$. We apply the combined rate for the recombination reactions involving O_2^+ listed in **Table 2.1**: $\alpha_{O_2^+} = 2.4\times10^{-13}\left(\frac{300}{T_e}\right)^{0.7}$.

2.4 Boundary conditions

Proper boundary and initial conditions are crucial to maintain stability as the simulation converges toward the steady-state solution. At the outer boundary we fix the plasma and magnetic field conditions according to Europa's location in Jupiter's magnetosphere at the moment represented by the steady state simulation. For the simulations of the *Galileo* E4 and E14 flybys, these values are informed by *in situ* data collected by the spacecraft. The Jovian background magnetic field ($\vec{B}_J$) was determined by linearly fitting the flyby magnetometer data, excluding the perturbed values within ~10 minutes of closest approach, and selecting the linear fit magnetic field values at closest approach; for E4, $\vec{B}_J$ = [55, -173, -412] nT and for E14, $\vec{B}_J$ = [10, -216, -409]. We used the magnetic moment values reported by Kivelson et al. (2000) for the E4 and E14 flybys; for E4, $\vec{M}$ = [-27, 88, 0] nT and for E14, $\vec{M}$ = [-5, 108, 0]. Paterson et al. (1999) reported an upstream total ion density of 20 cm^{-3} and upstream velocity of 100 km/s for the E4 flyby, and therefore, we used these parameters for the E4 simulation. In the absence of published PLS data for the E14 flyby, we used the E4 flyby plasma parameters. For both simulations we set the temperature of the O^+ ion fluid to 129.2 eV, resulting in an Alfvénic Mach number of 0.18.

The inner boundary of the simulation domain represents Europa's icy surface, and we therefore treat the plasma properties and the magnetic field differently from the outer boundary. We treat the velocity of the plasma fluids similarly to the method of Jia et al. (2009) to ensure that the flow of the MHD fluids is consistent with the magnetic field. We set each fluid velocity equal to the charge-averaged, field-perpendicular velocity

$$\vec{u}_{q,\perp} = \vec{u}_q - (\vec{u}_q \cdot \hat{b})\hat{b} \tag{2.16}$$

where $\hat{b}$ is the unit vector pointing along the local magnetic field $\vec{B}$.

If $u_{q,\perp}$ has a radially inward component, we impose a floating boundary condition such that the gradient of each fluid's density and pressure is zero, in effect modeling the absorption of plasma by Europa's surface. Where $\vec{u}_{q,\perp}$ has a radially outward component we limit the density and pressure to very small values so that the inner boundary is not a significant source of plasma.

We specify conditions for the magnetic field such that there is zero gradient across the inner boundary. The value of the magnetic field that is calculated by solving the magnetic induction equation (**Equation 2.9**) in the layer of cells adjacent to the surface is copied into the boundary cells. We prescribe Europa's induced magnetic field to be a dipole centered at the moon's origin with the moment directed in the XY plane. The direction and strength of the dipole moment correspond to the instantaneous induced field for each steady-state simulation.

2.5 Neutral atmosphere

We adopted the same functional form for the static neutral atmosphere as that used by Rubin et al. (2015), which is also similar to those used in previous models for Europa's plasma interaction (e.g., Saur et al., 1998; Schilling et al., 2008; Jia et al., 2018). The choice of surface densities and scale heights is informed by the precedent set by previous models for the plasma interaction and updated according to recent modeling of the neutral atmosphere using Monte Carlo methods (e.g., Plainaki et al., 2013; Teolis et al., 2017a; Vorburger and Wurz, 2018; Oza et al., 2019).

The functional form used to prescribe Europa's neutral atmosphere is

$$n_L = n_0 \cdot \exp\left(-\frac{|\vec{r} - \overrightarrow{r_E}|}{H_0}\right) + n_1 \cdot \exp\left(-\frac{|\vec{r} - \overrightarrow{r_E}|}{H_1}\right)$$
$$n_T = n_L \cdot (1 + A \cdot \cos\alpha) \tag{2.17}$$

The parameters n_L and n_T refer to the number density of O_2 on the leading and trailing hemispheres, respectively. The neutral atmosphere for the simulations in this chapter has a surface density of $n_0 = 2.5\times10^7$ cm^{-3}, and a scale height of $H_0 = 100$ km. **Figure 2.1d** shows the density of the atmosphere close to Europa's surface in the Z=0 plane as it decreases with distance from Europa's surface. We did not use the secondary population in these simulations (n_1 and H_1 in **Equation 2.17**). Instead, we increased the scale height of the primary population, in keeping with the results of Teolis et al. (2017a). We also decreased the surface density. The minimum and maximum column densities of this atmosphere are 2.5×10^{14} cm^{-2} on the leading/downstream hemisphere and 7.5×10^{14} cm^{-2} at the apex of the trailing/upstream hemisphere. These values are within the range of observed O_2 column densities reported by Hall et al. (1998) of $(2.4\text{-}14)\times10^{14}$ cm^{-2} based on whole-limb observations of Europa's oxygen atmosphere by the Hubble Space Telescope.

On the upstream/trailing side of the moon, the density of the neutral atmosphere is enhanced by a factor of $1+A$ at the apex of the trailing hemisphere. This enhancement then decreases according to the cosine of the angular distance from the apex of the trailing hemisphere (α). For these simulations A=2, in agreement with the results of Cassidy et al. (2013), who studied the generation of Europa's atmosphere by sputtering and implemented enhanced sputtering on the trailing hemisphere due to increased precipitation of magnetospheric plasma.

The density distribution of the neutral atmosphere controls the rate at which mass is loaded to the different ion fluids by the source terms discussed in **Section 2.3** of this chapter. The global mass-loading rate due to photoionization and electron impact ionization of the neutral atmosphere in the *Galileo* E4 and E14 flyby simulations is 3.1 kg/s for the O_2^+ fluid and

0.16 kg/s for the ionospheric O^+. These rates are comparable to the estimate by Saur et al. (1998) of ~7 kg/s for atmospheric loss due to ionization during the E4 flyby. The rate of charge-exchange for the O_2^+ fluid is 5.13 kg/s.

2.6 Model validation: *Galileo* E4 and E14 flybys

To demonstrate the ability of our model to simulate the plasma interaction, we first present two simulations representing the *Galileo* E4 and E14 flybys. The E4 flyby was simulated previously by Rubin et al. (2015) using a two-ion fluid model, and our results demonstrate that the present three-ion model performs at least as well as the previous model. As illustrated in **Figure 2.2**, the E4 flyby passed through Europa's plasma wake on the downstream side, while the E14 flyby passed through the upstream part of the plasma interaction. Additionally, the E14 flyby occurred while Europa was deeper in Jupiter's magnetic lobe. Therefore, these two flybys sampled the upstream and downstream features of the interaction under different driving magnetic field conditions, testing the model's performance at different locations and under different conditions.

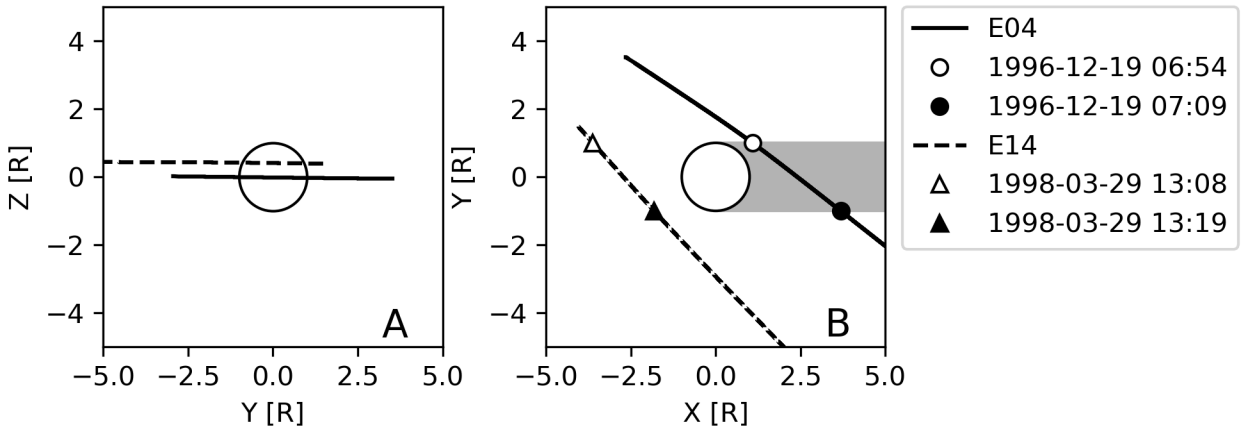

Figure 2.2: The E4 and E14 flyby trajectories in the (A) YZ and (B) XY planes. In Panel B symbols mark the points when the spacecraft entered and exited the region of Y = [1, -1]. The grey shaded region marks Europa's downstream geometric wake.

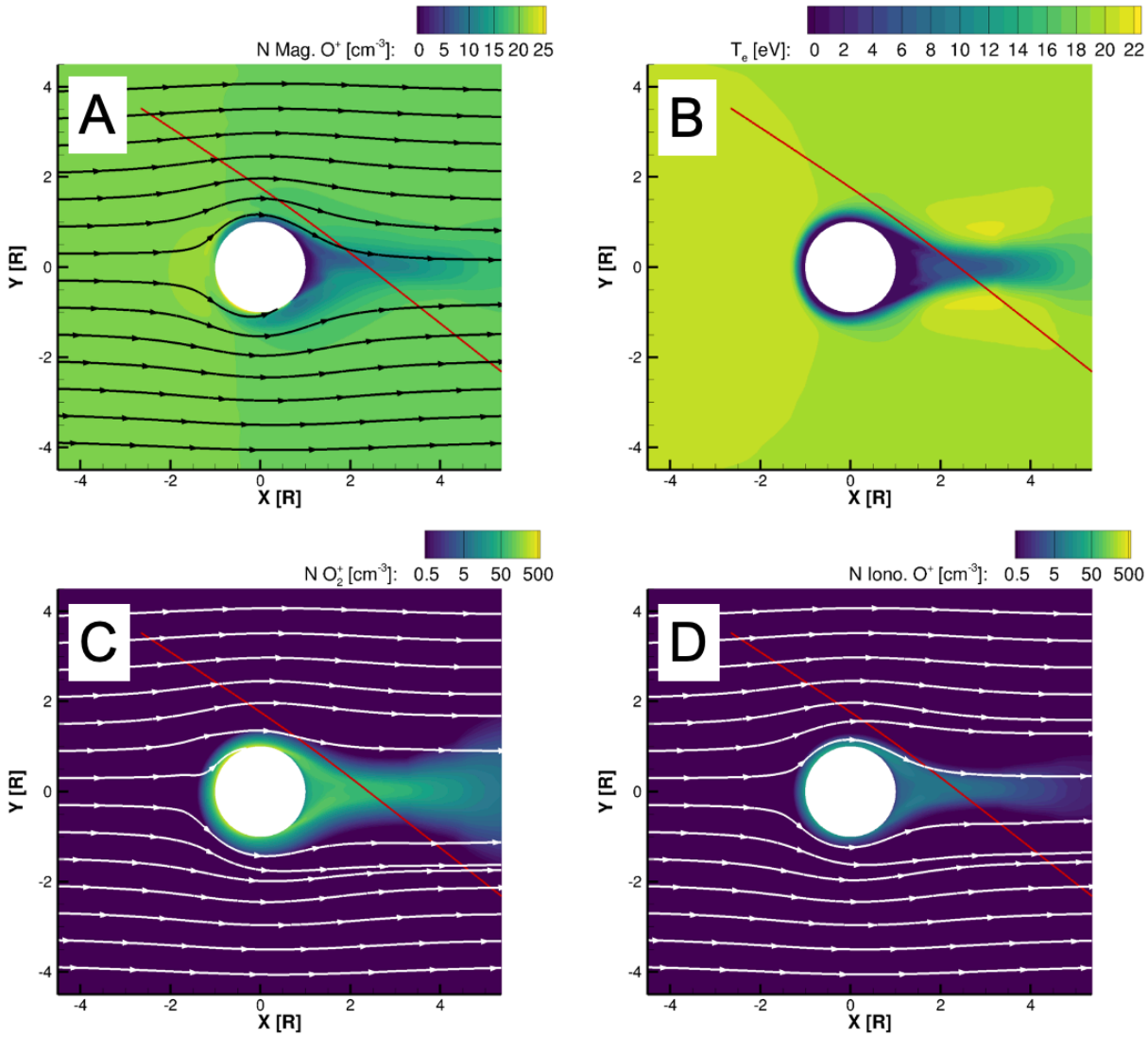

Figure 2.3: Density contours of the three ion fluids (A, C, D) and electron temperature (B) in the Z=0 plane from the simulation of the *Galileo* E4 flyby. Panel A shows the number density of magnetospheric O^+, Panel B shows the temperature of electrons, Panel C shows ionospheric O_2^+, and Panel D shows ionospheric O^+. In Panels A, C, and D the black or white lines with arrows show velocity streamlines of the corresponding ion fluids in the Z=0 plane. In all panels the trajectory of the E4 flyby is marked by a red line.

Figure 2.3 shows the density and velocity streamlines of the three ion fluids, as well as the temperature of the electron fluid, in the Z=0 plane for the E4 simulation. On the upstream side of the plasma interaction the density of magnetospheric O^+ increases slightly (**Figure 2.3a**) and streamlines of all the ion fluids are diverted around Europa toward the sub- and anti-Jovian directions. Close to Europa's surface the electron temperature is low as it is cooled by electron impact ionization of the atmosphere (**Equation 2.13**, **Figure 2.3b**). Correspondingly, the density of the ionospheric fluids is high near Europa's surface as mass is added to these fluids due to electron impact ionization (**Figure 2.3c,d**). In the plasma wake the density of magnetospheric O^+ is depleted (**Figure 2.3a**), as the streamlines that carry the magnetospheric plasma from the upstream simulation boundary were diverted around the moon and do not recover until > 4 R_{Eu} downstream. Conversely, the density of the ionospheric fluids is enhanced in the plasma wake (**Figure 2.3c,d**) as these fluids are generated close to Europa's surface and are then carried downstream. While the electron temperature is generally low in the plasma wake, it increases to a few eV farther downstream as heat is conducted from the north and south towards the equator along magnetic field lines (**Equation 2.4**). The features of the E14 simulation are generally similar, with minor differences caused by the different magnetic field configuration.

2.6.1 The E4 flyby

The E4 flyby occurred on 1996-12-19 from 06:54–07:09 UT. The spacecraft passed through Europa's wake with closest approach distance of 0.4 R_{Eu}. Europa was located in the northern lobe of Jupiter's magnetosphere, above the plasma sheet at 6.5˚ magnetic latitude (Kivelson et al., 2000). **Figure 2.4** compares the magnetic fields observed by the *Galileo* magnetometer with the model results extracted from the E4 simulation along the spacecraft trajectory, while **Figure 2.5** shows the simulation magnetic fields in context in the Z=0 plane. **Figure 2.4** illustrates that

during the E4 flyby the X and Y components of the magnetic field were dominated by Europa's induced magnetic field. Both components vary smoothly near closest approach, then return to their background values as the spacecraft exited the wake. In the center of the wake the model B_y field (**Figure 2.4**, second panel) dips, then peaks before exiting the wake. This could be a distortion of a similar feature observed in the magnetometer B_y data, where there is a shallow dip followed by a peak of ~20 nT at 07:00 UT. In the Z component of the magnetic field there is very little contribution from the induced field, as it is represented by a dipole moment directed in the XY plane and the E4 flyby was nearly confined to the XY plane. Therefore, the perturbations in B_z are caused predominantly by the magnetic fields associated with the plasma interaction. The *Galileo* magnetometer observed a weakening of the Z component and the overall magnitude of the magnetic field just before closest approach, then a slow return to background values as the spacecraft passed through the wake and moved away from the moon. Our simulation shows the same change in B_z including the depletion in magnetic field strength near closest approach and the same recovery through Europa's plasma wake.

While the magnetic field weakened near closest approach, **Figure 2.6** shows that the density of plasma in the wake was enhanced during the E4 flyby. The PLS reports that while the number density of the upstream magnetospheric plasma was 20 cm^{-3}, the density began to rise just prior to closest approach and in the center of Europa's wake the plasma density abruptly increased by a factor of three. Our simulation exhibits similar features. Prior to closest approach the density begins to increase due to the presence of O_2^+, though the increase is slower and less dramatic in the model. We also observe that the modeled plasma density peaks in the center of the wake, though the modeled peak is wider than the single data point of the PLS measurements. Paterson et al. (1999) note that this peak is likely significant despite the single data point due to a

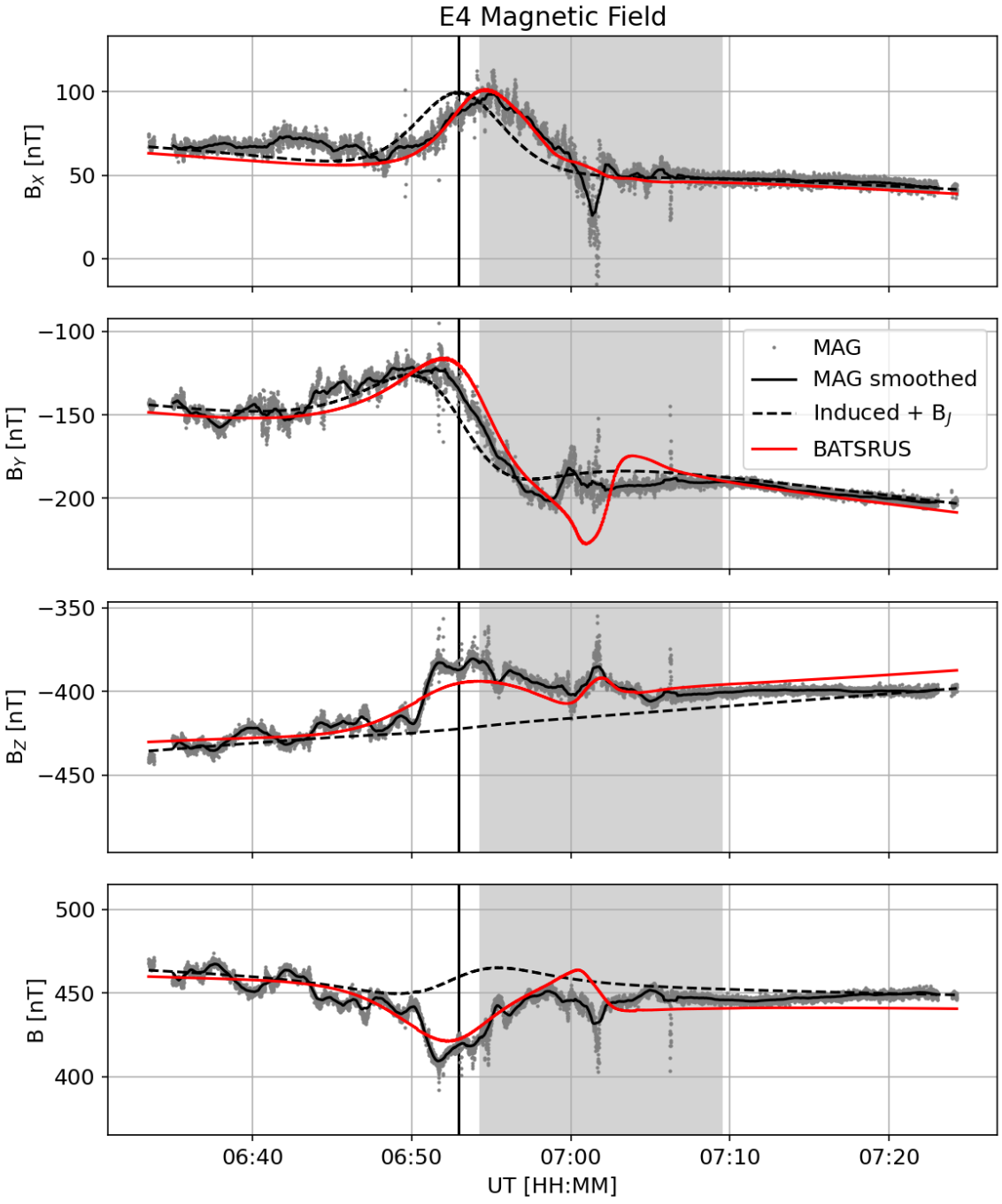

Figure 2.4: Comparison of simulated magnetic fields to the *Galileo* magnetometer observations for the E4 flyby. Gray dots indicate the *Galileo* magnetometer data, while the solid black line shows the data smoothed with a rolling boxcar average of 50 seconds. The black dashed line indicates the sum of the dipole representing the induced field background Jovian magnetic field. The red solid line gives the simulated magnetic field summed with the trend in the background magnetic field as determined from the data. The vertical black line indicates the time of closest approach, while the gray shaded area spans the time that the spacecraft spent in the region of -1 $R_{Eu} < Y < 1\ R_{Eu}$.

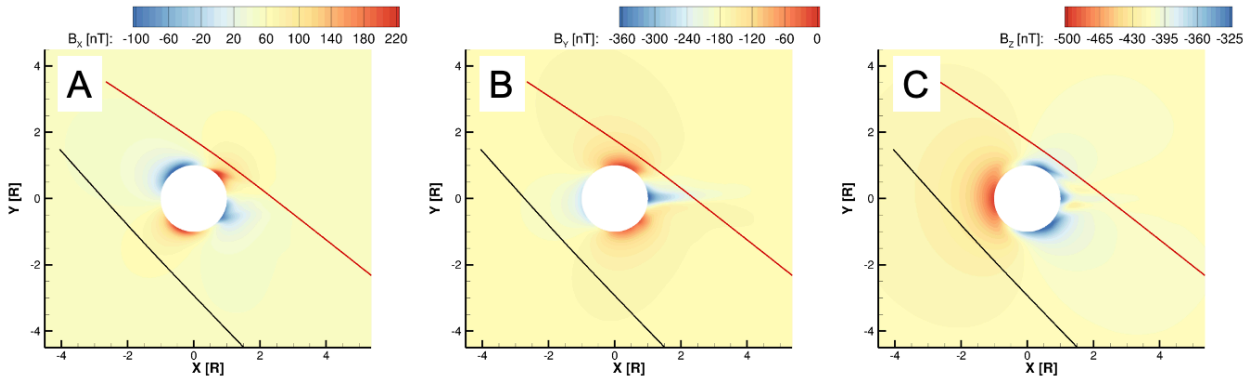

Figure 2.5: Color contours showing the B_x (A), B_y (B), and B_z (C) components of the simulation magnetic field from the E4 simulation in the Z=0 plane. In all panels the trajectory of the E4 flyby is marked by a red line. A black line marks the projection of the E14 flyby into the Z=0 plane.

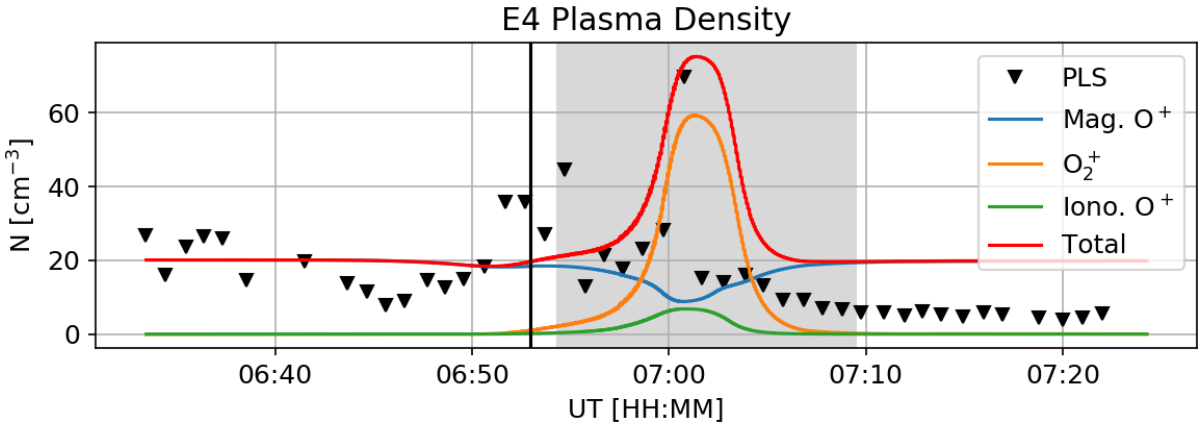

Figure 2.6: Comparison of the simulated plasma densities to the *Galileo* PLS total plasma density observations for the E4 flyby. The observed PLS densities are given by black triangles while the color curves show the number density of the Jovian magnetospheric O^+ (blue), O_2^+ (orange), ionospheric O^+ (green), and the total ion number density (red) which is equivalent to the electron density. Other annotations are as described for **Figure 2.4**.

simultaneous increase in temperature. **Figure 2.3** shows these different fluid densities in context in the equatorial plane. By separately tracking different ion fluids in the simulation, our multi-fluid model shows that the ionospheric species are responsible for this density increase. As some of the ambient magnetospheric O^+ is absorbed by Europa on the upstream side, this leads to a depletion of magnetospheric O^+ in Europa's wake region relative to the upstream densities. The ionospheric fluids are abundant near Europa's surface where the neutral atmosphere is densest, so these fluids are transported downstream to fill the wake and are then observed on the flyby trajectory as shown in **Figure 2.6**, causing the peak in number density.

The time of closest approach for the E4 flyby occurred as the spacecraft was moving from the flank of the interaction region to the sub-Jovian edge of the wake. **Figure 2.7** shows that the X component of the plasma velocity was enhanced as the spacecraft passed through the fast flows on the flank, then decreased and returned to the ambient values through the wake. Our simulation has accurately modeled the enhanced speeds on the flank. However, there is a systematic offset in the Y component of the velocity between our simulation and the data, with the PLS seeing more positive flow in the Y direction by about 20 – 30 km/s compared to the simulation. An exploratory simulation was run to investigate the effects of adding a Y component of 25 km/s to the velocity boundary condition in the simulation. We found that while the agreement with the Y component of the velocity was improved, the data-model comparison between the magnetic fields worsened. Therefore, we do not think that a constant Y component in the flow of the ambient background plasma is responsible for this discrepancy.

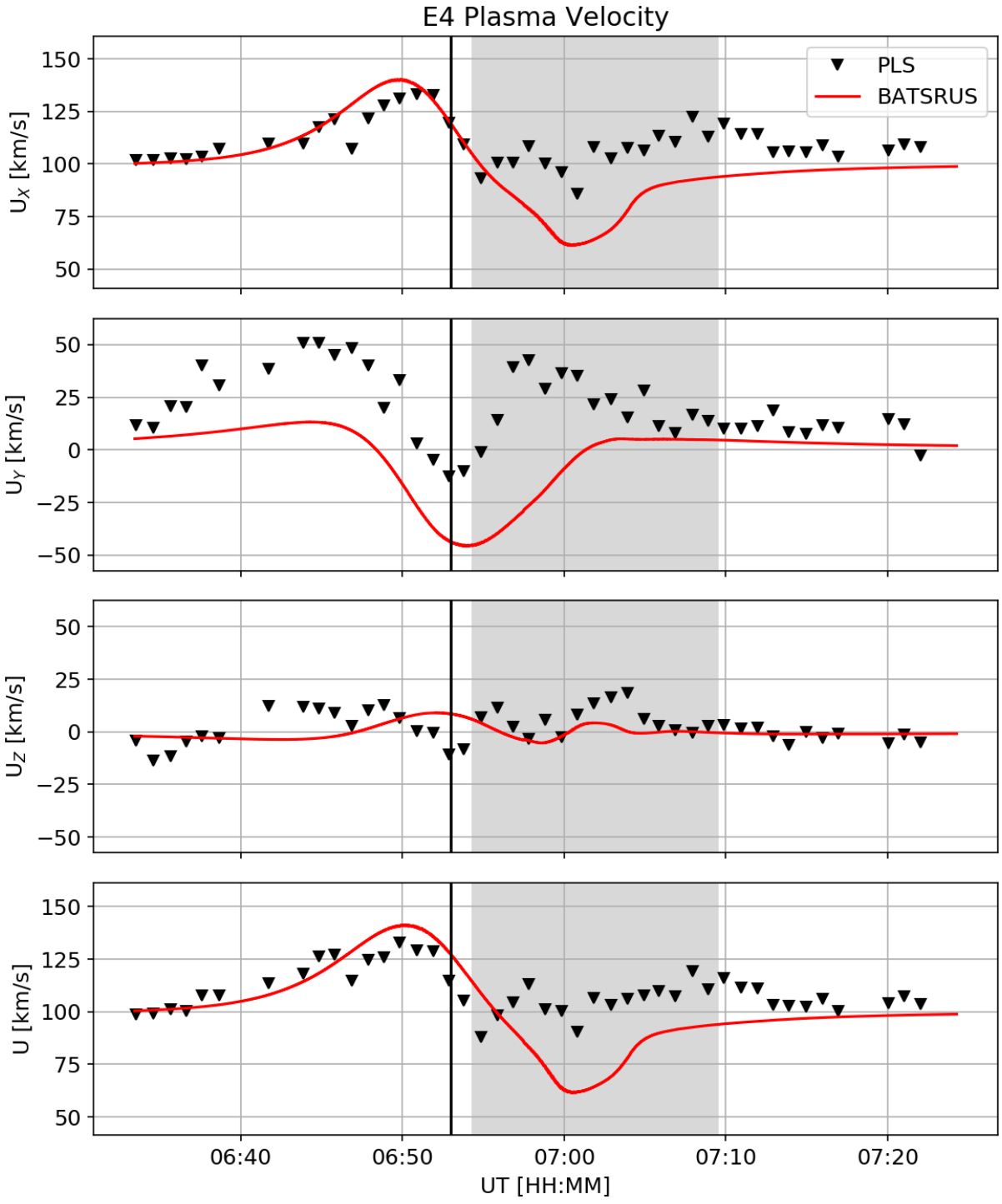

Figure 2.7: Comparison of the simulated charge-averaged fluid velocity (red curve) to the *Galileo* PLS total plasma velocity observations for the E4 flyby (Paterson et al., 1999) (black triangles). Other annotations are as described for **Figure 2.4**.

2.6.2 The E14 flyby

On 1998-3-29 from 13:05–13:40 UT the *Galileo* spacecraft conducted the E14 flyby across the upstream part of Europa's plasma interaction, as shown in **Figure 2.2**. The distance of closest approach was 1.05 R_{Eu}, and Europa was positioned deeper in Jupiter's northern lobe at 9.2˚ magnetic latitude (Kivelson et al., 2000). **Figure 2.8** shows a good agreement to within a few nT between the simulated magnetic fields and the observations from the magnetometer. **Figure 2.8** shows that, as for the E4 flyby, the variations of the X and Y components of the magnetic field are dominated by the induced magnetic field, but the model accurately simulates the magnetic effects of the plasma interaction, closing the gap between the induced field and the data. Similarly, in the Z component there is good agreement between the data and the model as the spacecraft passes through the enhancement of magnetic field strength upstream of the moon, caused by the slowing of the plasma flow and piling-up of magnetic field lines on the upstream side of the interaction. This feature is illustrated in **Figure 2.5c**. Between the E4 and the E14 simulations, the differences in the magnetic fields are primarily in the background values; the perturbations from the background are similar. While the upstream pile-up of magnetic field is roughly symmetric about the XZ plane, the E14 flyby trajectory passes through the -Y side of the interaction, causing the spacecraft to observe the peak in magnetic field strength not when the spacecraft passes through Y=0 (the center of the grey span in **Figure 2.8**), but later, closer to the time of the spacecraft's closest approach.

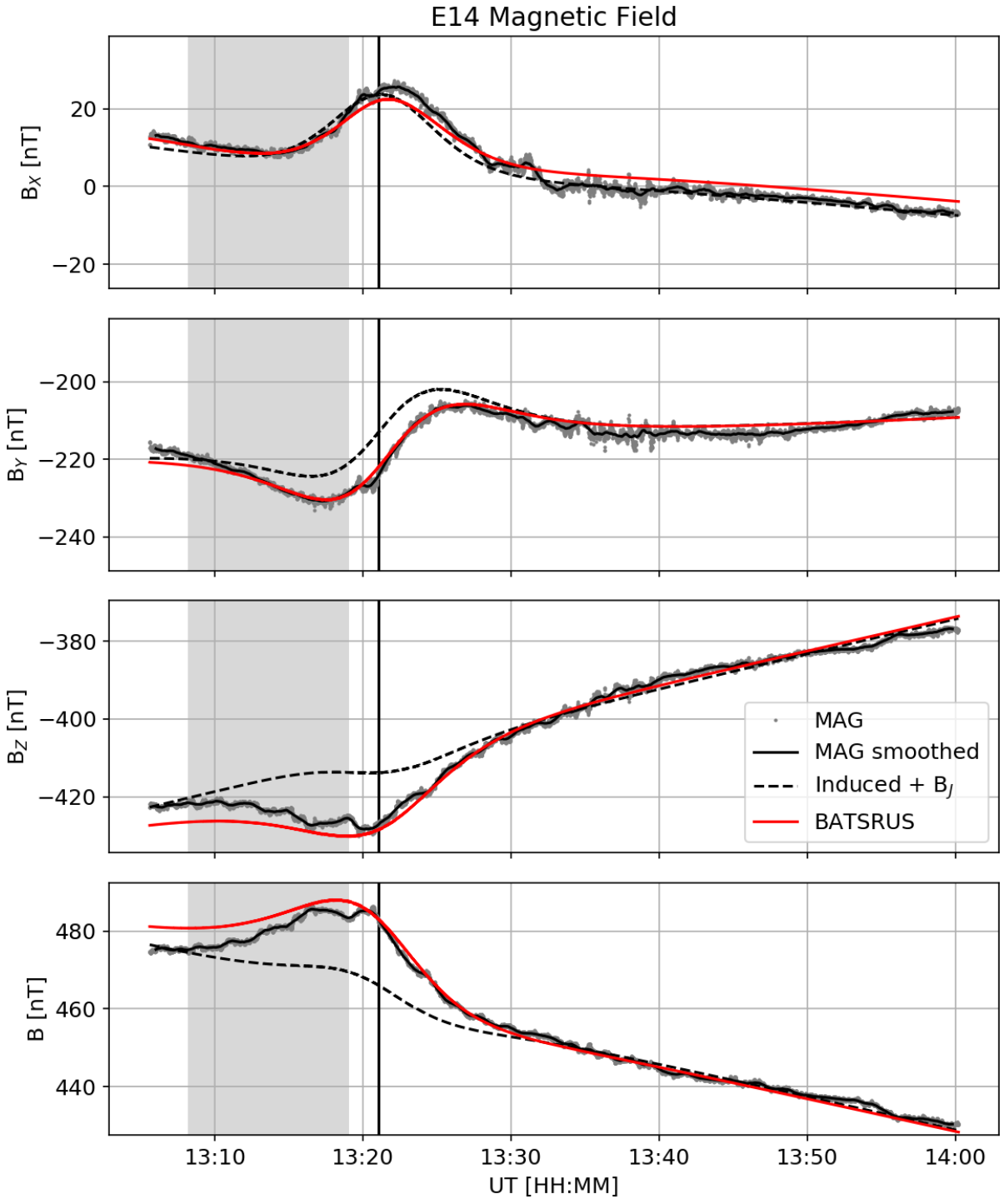

Figure 2.8: Comparison of simulated magnetic fields to the Galileo magnetometer observations for the E14 flyby. Annotations are as described for **Figure 2.4**.

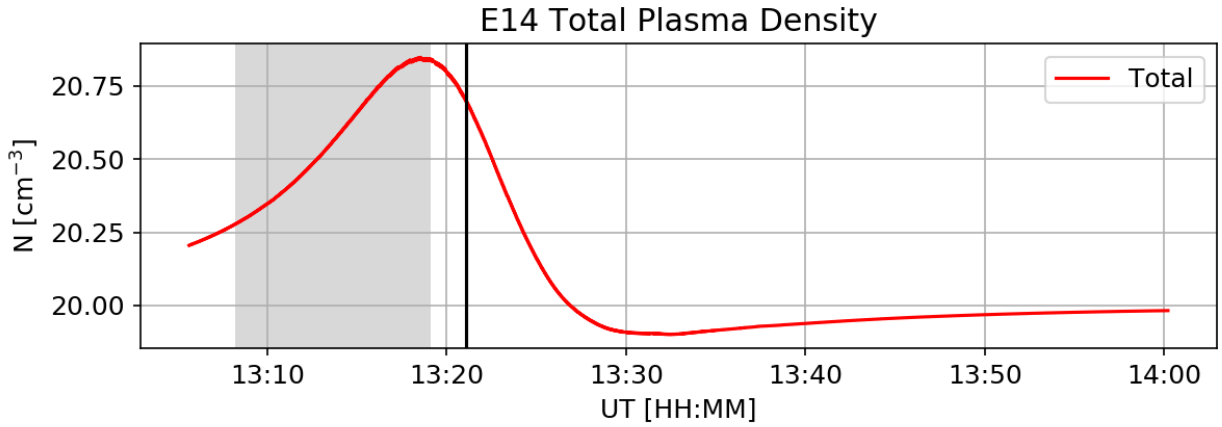

Figure 2.9: Simulated plasma density for the E14 flyby. Published PLS densities are not available for this flyby. Annotations are as described for **Figure 2.6**.

In **Figure 2.9** and **Figure 2.10** we show the E14 simulated density and velocity, though no published PLS plasma moments are available for this flyby. The closest approach of the E14 flyby occurred at 1.05 R_{Eu} from the surface on the upstream side, more than twice as far as the distance of closest approach for the E4 flyby. At these distances, the densities of the ionospheric fluids in the simulation are negligibly small along the spacecraft trajectory (~2×10^{-3} cm^{-3}), and, therefore, we omit the densities of the ionospheric fluids in **Figure 2.9**. However, we see that there is a slight enhancement in the total number density due to the magnetospheric O^+ fluid on the upstream side of the plasma interaction, again caused by the slowing-down of the flow (**Figure 2.10**) and piling-up of the magnetic field (**Figure 2.8**) ahead of the moon. The trajectory then proceeds through the anti-Jovian flank, where the flow speed increases, before moving away from Europa. The density and velocity have returned to their ambient values by the end of the flyby.

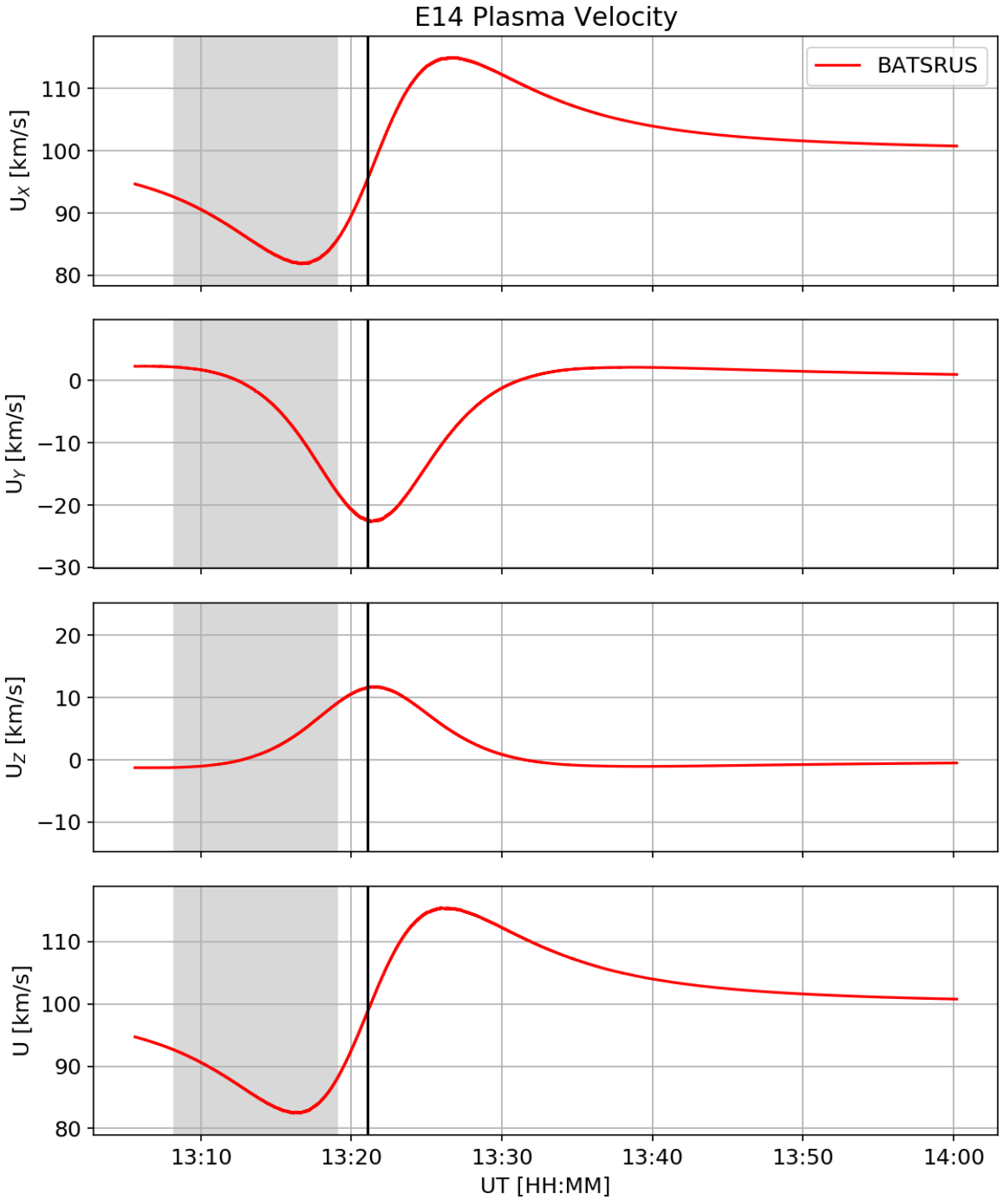

Figure 2.10: Simulated charge-averaged plasma velocity for the E14 flyby. Published PLS velocities are not available for this flyby. Annotations are as described for **Figure 2.6**.

The good data-model comparison between our simulations and the *Galileo* observations for these flybys demonstrates that our model can accurately represent the large-scale features of the plasma interaction, and can contend with the changing conditions throughout Jupiter's magnetosphere.

2.7 Conclusions

We have extended and refined a multi-fluid MHD model for Europa's plasma interaction, based on the BATS-R-US code, to separately model the bulk properties of Jupiter's magnetospheric plasma (represented by O^+) and the plasmas originating from Europa's atmosphere (O_2^+ and O^+). This was accomplished by adding to the model a new ion fluid to represent thermal magnetospheric O^+. The new ion fluid is treated differently in some ways from the ionospheric fluids; mainly, no magnetospheric O^+ is generated by ionization, but instead enters the simulation from the upstream boundary. Other improvements were made to the implementation of electron impact ionization to better model the effects of the Io plasma torus on the electron pressure. The scheme by which the multi-fluid MHD equations are solved was also improved, reducing numerical diffusion in the model in order to model the transport of plasma more accurately. In general, the new model separately treats the major plasma populations of Europa's space environment and more accurately models the behavior of these different populations in the plasma interaction.

We have validated the model by simulating the *Galileo* E4 and E14 flybys and comparing our simulated magnetic fields, plasma density, and plasma velocity to the spacecraft observations. The favorable comparison between the data and the model for these two flybys demonstrates that the model is capable of accurately representing Europa's plasma interaction under different magnetic configurations, and that the representation is good on both the upstream

and downstream sides of the moon. With this tool now verified, we are ready to apply it to more general questions and investigations of Europa's plasma interaction in the subsequent chapters.

Chapter 3 Effect of Jovian Magnetospheric Conditions on Precipitation of Thermal Plasma to Europa's Surface

To improve our understanding of Europa's plasma interaction and its relationship with Europa's atmosphere and surface, as well as with Jupiter's magnetosphere, we conducted a parameter study to characterize the precipitation of thermal magnetospheric plasma to Europa's surface under different magnetospheric conditions. The precipitation of magnetospheric plasma is significant in the generation of Europa's atmosphere because thermal magnetospheric ions are responsible for ejecting a significant amount of neutral particles from the ice (Cassidy et al., 2013; Vorburger and Wurz, 2018). Conditions in Jupiter's magnetosphere drive the plasma interaction, affecting the magnetic fields and bulk plasma properties near Europa, and therefore we expect variations in magnetospheric conditions to control how magnetospheric plasma reaches Europa's surface.

Europa's tenuous atmosphere is composed of H_2O, H_2, and O_2 (Hall et al., 1995, 1998), with O_2 being the dominant component (McGrath et al., 2009). Neutrals are liberated from Europa's icy surface by a number of processes, including sputtering, radiolysis, sublimation, and, potentially, water plumes (see a recent review by Plainaki et al., 2018). Among these processes, sputtering by thermal magnetospheric ions (<100 eV) is expected to be more strongly affected by the plasma interaction (Johnson et al., 2009). Sputtering impacts by energetic ions tend to be uniformly distributed over Europa's surface (Pospieszalska and Johnson, 1989; Paranicas et al., 2002; Breer et al., 2019). However, sputtering by cooler, thermal plasma tends to be distributed asymmetrically, mainly impacting the trailing hemisphere as the corotating thermal population

flows past Europa, leaving a wake with much-reduced plasma density on the downstream side (Saur et al., 1998; Cassidy et al., 2013). Thermal particles sputter fewer neutrals per impact due to their lower energies, but the number flux of thermal plasma precipitating onto Europa's surface is much higher than that of energetic particles, potentially yielding a significant contribution to the total amount of sputtered neutrals (Cassidy et al., 2013; Vorburger and Wurz, 2018). The precipitation of thermal plasma is therefore an important factor in the yield of neutral O_2 and the subsequent generation of Europa's ionosphere. To understand this process, we must first characterize the precipitation of the thermal magnetospheric plasma. The spatial distribution and rate of thermal plasma precipitation onto Europa's surface are sensitive to the plasma interaction with Europa's ionosphere, which tends to divert some of the ambient flow of magnetospheric plasma around the moon, partially shielding the surface from direct impact. Understanding the precipitation of the thermal magnetospheric plasma onto Europa's surface and how it varies with the external conditions therefore requires self-consistent modeling of the different plasma populations present in the system and their coupling to the electromagnetic fields.

To study the effects of variations in external, magnetospheric conditions on the plasma interaction and, subsequently, on the patterns of precipitation of thermal plasma, we designed a parameter study. Using the multi-fluid MHD model for Europa's plasma interaction described in **Chapter 2**, we conducted nine different simulations spanning the range of external conditions that Europa is subjected to within Jupiter's magnetosphere.

In this chapter we begin by describing in **Section 3.1** the principles on which the parameter study was designed and how the model described in **Chapter 2** was applied. In **Section 3.2** we present the results of the simulations and describe how the precipitation of

thermal plasma was derived from them. In **Section 3.3** we identify trends in the results to explain how the external conditions of Jupiter's magnetosphere affect the precipitation. We finish the chapter in **Section 3.4** by summarizing our results.

3.1 Methods

In this section we describe the methods by which the outer boundary plasma and magnetic field conditions, and the values for Europa's induced field, were selected for each simulation. The input values are summarized in **Table 3.1**.

To select the boundary conditions for the parameter study simulations we relied on the results from the empirical plasma model of Bagenal et al. (2015) and the Jupiter magnetic field model of Khurana (1997) at Europa's orbit. We selected the magnetic field and plasma density from the models at three System III longitudes chosen to represent Europa's location while it is deep in Jupiter's southern magnetic lobe (19˚ SIII longitude, -9.6˚ Magnetic latitude), transitioning from the southern lobe to the center of the plasma sheet (76˚ SIII longitude, -5.6˚ Magnetic latitude), and in the center of the plasma sheet crossing from the southern to the northern lobe (110˚ SIII longitude, -0.3˚ Magnetic latitude). The corresponding scenarios in the northern lobe would have differed only in the direction of the background magnetic field and the direction of the induced field. This would cause the magnetic features of the interaction to be mirrored about the XZ and YZ planes and we do not expect this to significantly affect the overall precipitation of plasma. We therefore limited the complexity of the study by omitting the northern cases.

Table 3.1: Simulation boundary conditions. Magnetic field and plasma parameters for the outer boundary and induced dipole moment for each simulation.

	Case 1			Case 2			Case 3		
S3 Lon. [˚]	19	76	110	19	76	110	19	76	110
Mag. Lat. [˚]	-9.6	-5.6	-0.3	-9.6	-5.6	-0.3	-9.6	-5.6	-0.3
B_{Jx} [nT]	42.1	93.8	93.1	42.1	93.8	93.1	42.1	93.8	93.1
B_{Jy} [nT]	226.3	126.9	0	226.3	126.9	0	226.3	126.9	0
B_{Jz} [nT]	-400	-400	-400	-400	-400	-400	-400	-400	-400
M_x [nT]	-21.1	-46.9	-46.5	-21.1	-46.9	-46.5	-21.1	-46.9	-46.5
M_y [nT]	-113.2	-63.5	0	-113.2	-63.5	0	-113.2	-63.5	0
M_z [nT]	0	0	0	0	0	0	0	0	0
N_{O+} [cm^{-3}]	51.9	59.0	63.6	99.0	130.4	159.9	140.0	205.2	293.2
$U_{O+,x}$ [km/s]	100	100	100	100	100	100	100	100	100
T_{O+} [eV]	245.1	222.7	210.6	151.2	122.9	105.5	116.6	87.5	66.9
M_A	0.29	0.33	0.35	0.39	0.49	0.56	0.47	0.61	0.76

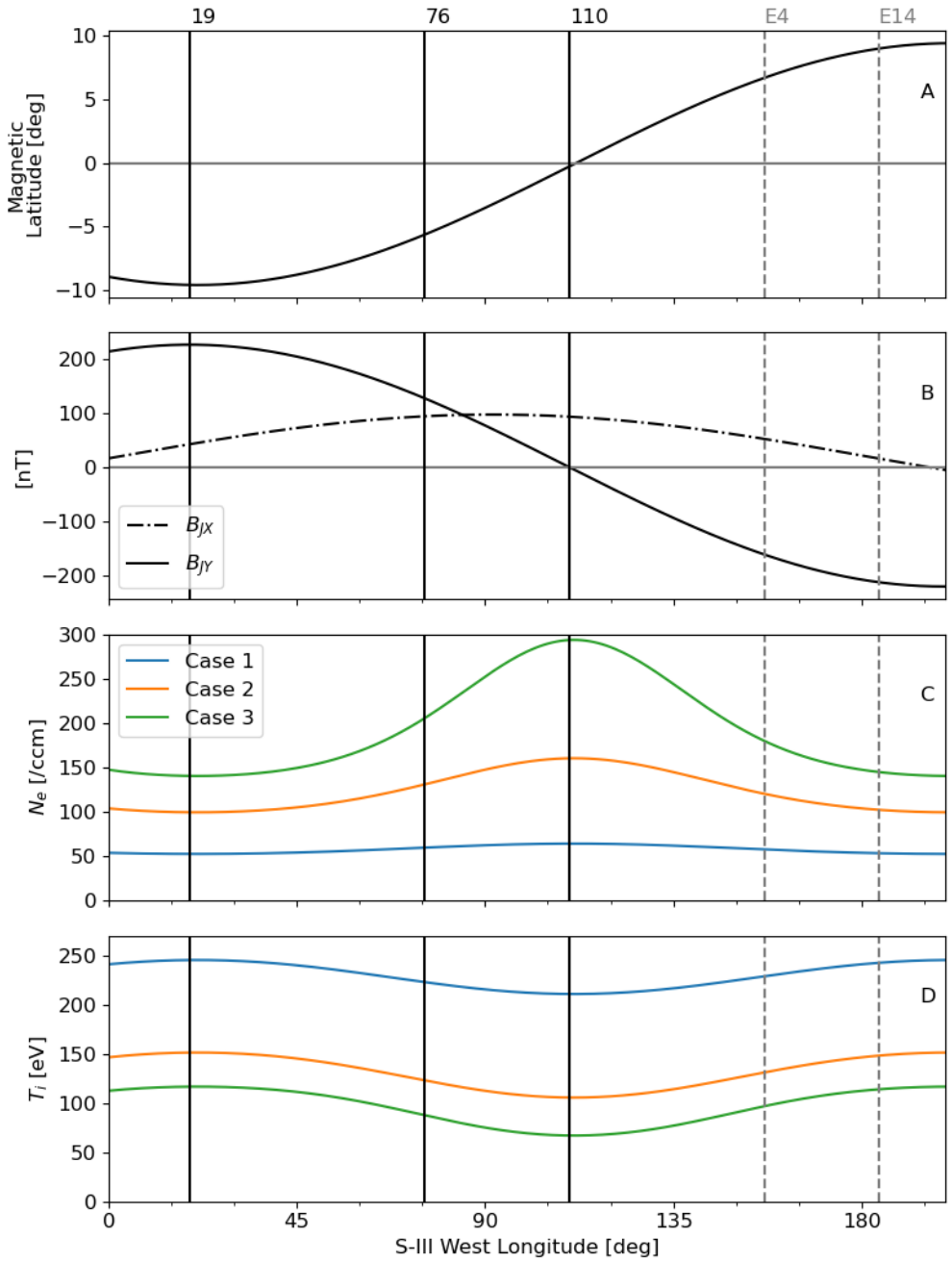

Figure 3.1: The range of parameters for the nine simulations at different magnetospheric conditions at Europa: (A) Magnetic latitude, (B) models for the Jovian magnetic field and (C and D) plasma conditions at Europa's orbit. Vertical black lines indicate the System III longitudes at which parameters for 9 simulations were selected. In panels C and D the blue, orange, and green lines correspond respectively to the magnetospheric states 1, 2, and 3 of *Bagenal et al.* (2015). The vertical dashed grey lines indicate the longitudes of the *Galileo* E4 and E14 flybys.

The temperature of the Jovian magnetospheric ions for the parameter study simulations was determined using the power-law relationship between electron density and ion temperature that Bagenal et al. (2015) identified. In addition to selecting three locations, we considered three different global states of Jupiter's magnetosphere, which result in different upstream plasma conditions at Europa's orbit. As Bagenal et al. (2015) report three cases for the general state of the Jovian magnetosphere (Case 1: Low density and high temperature plasma; Case 2: Medium density and temperature plasma; Case 3: High density and low temperature plasma), this results in a total of nine simulations, as illustrated in **Figure 3.1**.

In setting the background Jovian magnetic field for the simulations, to reduce the number of varying parameters we chose to fix the Z component of the ambient magnetic field (B_{Jz}) to -400 nT. We then calculated the magnetic moment of Europa's induced dipole assuming 100% induction efficiency by the time-varying components of the magnetospheric magnetic field (B_{Jx} and B_{Jy}) such that M_X [nT] = -B_{Jx}/2 and M_Y [nT] = -B_{Jy}/2. Here the magnetic moment is given as a magnetic field vector with the equatorial strength of the magnetic field at Europa's surface as in Kivelson et al. (2000); in conventional units of A m^2 the moment is $4\pi R_{Eu}^3 \mathbf{M}/\mu_0$, where μ_0 is the magnetic permeability.

We set the speed of the corotating magnetospheric plasma relative to Europa to 100 km/s for all simulations. We also set the electron temperature to 20 eV for all the simulations, as previously described in **Chapter 2**.

We selected a relatively low density of the upstream plasma for the *Galileo* flyby simulations in **Chapter 2** when compared to the upstream density in the parameter study simulations. For the nine simulations used in the parameter study, we set the upstream plasma density according to the electron densities reported by Bagenal et al. (2015), which were derived

from the upper hybrid resonance frequencies as measured by the Galileo Plasma Waves Subsystem (PWS) (Kurth et al., 2001). As pointed out by Bagenal et al. (2015), the PWS-derived densities are generally higher than the PLS measurements. Since published plasma moments from PLS are available only for few close Europa flybys (e.g., E4 in Paterson et al., 1999), we based our choice of the upstream plasma densities for the parameter study on the PWS results (e.g., Kurth et al., 2001; Bagenal et al., 2015). As a result, the densities in our parametric study presented in this chapter are consistently higher than the PLS density we used for the *Galileo* flyby simulations in **Chapter 2**.

The flyby simulations in the previous chapter were intended to represent Europa's plasma interaction at the specific time of the corresponding flybys for the purpose of validating the model against the *Galileo* dataset. The parameter study simulations in this chapter do not represent any specific instant in time, but rather demonstrate the range of different responses of Europa's plasma interaction to the normal variations of the plasma and magnetic field in Jupiter's magnetosphere. The chosen input parameters span the known ranges for the Jovian magnetic field and plasma density and temperature at Europa's orbit (e.g., Kivelson et al., 2009; Bagenal et al., 2015; Bagenal and Dols 2020) and the associated Alfvén Mach numbers for all but the two most extreme simulations fall within the expected range of $M_A = \frac{u}{v_A} = \frac{u\sqrt{\mu_0 \rho}}{B}$ =0.08–0.59 (Kivelson et al., 2004), where v_A is the Alfvén speed, u is the velocity of the ambient magnetospheric plasma, and B is the magnitude of the magnetospheric magnetic field. Therefore, while the selected upstream plasma densities do differ systematically between the flyby and the parameter study simulations, the parameter study simulations provide a realistic representation of the variability of the plasma interaction.

To facilitate comparison with the simulations in **Chapter 2**, we have included them in many of the figures in this chapter.

3.2 Results

To study the response of the plasma interaction to the variable driving conditions at Europa through one synodic rotation, we have conducted nine simulations. Each simulation represents the plasma interaction at one of three representative locations relative to the center of Jupiter's plasma sheet (lobe, transition, and plasma sheet), with three different possible cases of the magnetospheric state after Bagenal et al. (2015) (low density Case 1, medium density Case 2, and high density Case 3). See **Table 3.1** for the detailed input parameters for the parameter study simulations. In several of the figures we include the simulations from **Chapter 2** to demonstrate how the *Galileo* flyby simulations compare to the parameter study simulations.

Figure 3.2 shows the X component of the charge-averaged velocity (**Equation 2.7**) in the XZ plane for each simulation. The XZ plane intersects the Alfvén wing structure of the plasma interaction (Neubauer, 1998), though in the lobe and transitional magnetic configurations (left and center columns of **Figure 3.2**) there is a non-zero Y component to the background magnetic field, which causes the Alfvén wings to tilt out of the XZ plane at approximately the same angle as the YZ component of the background magnetic field. This tilt causes the fast flows of plasma that are diverted to either side of the Alfvén wings to pass through the XZ plane and appear in the leftmost panels in **Figure 3.2**.

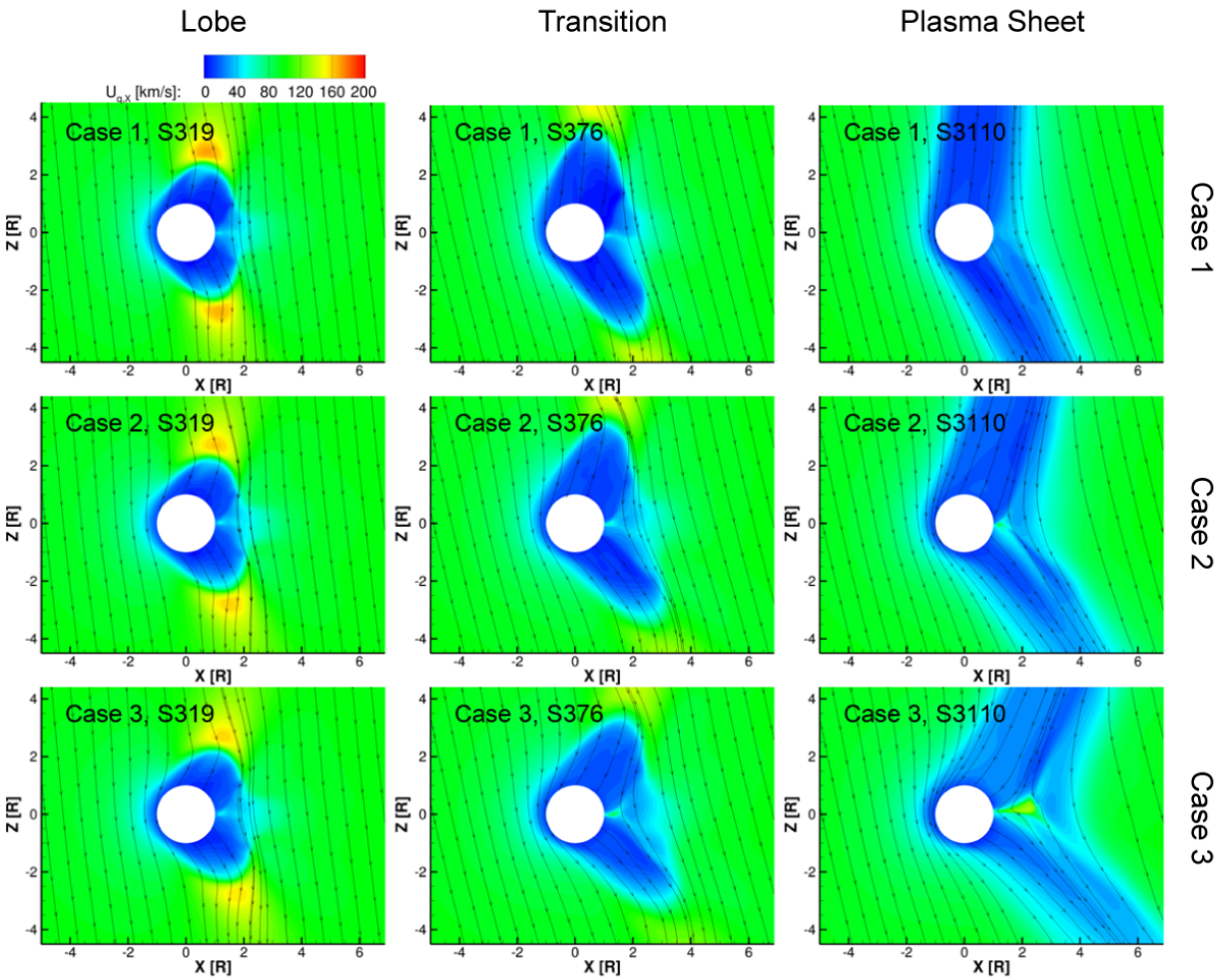

Figure 3.2: Contours of u_{qx} overlaid with B_{XZ} field lines in the Y=0 plane for each of the 9 parameter study simulations.

Within the Alfvén wings the plasma velocity slows on the field lines that are connected to Europa's ionosphere (Neubauer, 1998; Volwerk et al., 2007). This slowing of the flow causes the magnetic field within the Alfvén wings to bend by the angle θ_A relative to the background magnetic field. In the idealized situation where the plasma flow is perpendicular to the background Jovian magnetic field, this angle is related to the Alfvén Mach number by $\theta_A = \tan^{-1} M_A$ (Kivelson et al., 2009), such that as M_A increases θ_A increases as well, and the Alfvén wings are bent at increasingly extreme angles from the background field. While the plasma flow

and the background field are not orthogonal in any of these simulations, we observe that in the plasma sheet simulations (right column of **Figure 3.2**) θ_A increases from Case 1 to Case 3 as the density of the ambient plasma, and thus the corresponding Alfvénic Mach number, increases.

Table 3.2 summarizes the mass-loading and charge exchange rates for the ionospheric fluids in each simulation. In the parameter study simulations the average electron impact ionization rate ranges from (2.4–11.5)×10^{-6} s^{-1}. The global mass loading rates range from 4.1–11.9 kg/s for O_2^+ and 0.21–0.60 kg/s for ionospheric O^+. The mass loading rate depends on the neutral density and the electron bulk parameters. Since the atmosphere is identical in all nine simulations, the variation in these rates is caused by differences in the solutions for the electron temperature and density.

Table 3.2: Mass-loading and charge exchange rates calculated for the ion species in each simulation.

	Case 1			Case 2			Case 3		
S3 Lon. [°]	19	76	110	19	76	110	19	76	110
Mag. Lat. [°]	-9.6	-5.6	-0.3	-9.6	-5.6	-0.3	-9.6	-5.6	-0.3
Mass-loading O_2^+ [kg/s]	4.1	4.6	4.8	5.7	7.2	8.1	7.1	9.6	12.1
Mass-loading O^+ [kg/s]	0.21	0.24	0.25	0.29	0.37	0.41	0.37	0.49	0.61
Charge exchange O_2^+ [kg/s]	6.66	7.29	7.44	9.19	11.45	13.11	11.54	15.97	21.52

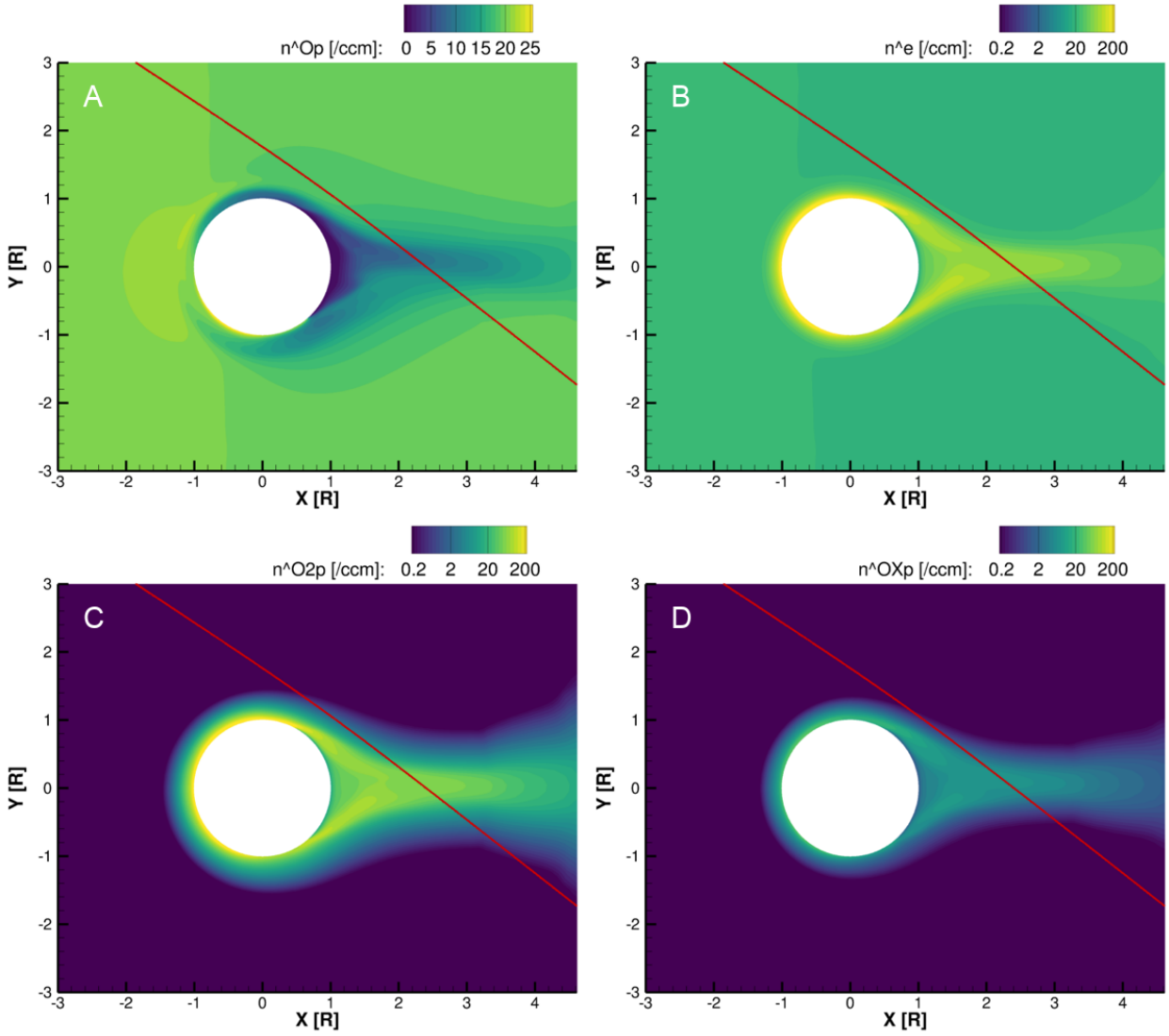

Figure 3.3: Simulated number densities on a logarithmic scale in the equatorial plane of the case 1, plasma sheet simulation for (A) Jupiter's magnetospheric O^+ ions, (B) electrons, (C) O_2^+ ions, and (D) ionospheric O^+ ions.

To illustrate the general features of the plasma interaction as predicted by our multi-fluid simulations, we show the equatorial plane of the Case 1, plasma sheet simulation in **Figure 3.3** and **Figure 3.4**. We have focused on this simulation for two reasons. The first reason is that the Jovian magnetic field is confined to the XZ plane, making the features of the plasma interaction in the equatorial plane easier to interpret since there are no asymmetries associated with the Y

component of the background magnetic field. The second reason is that the Alfvénic Mach number for this simulation (0.35) is close to the average Mach number expected for Europa's plasma interaction (Kivelson et al., 2004), and we therefore expect the features of the plasma interaction in this case to reflect the nominal state.

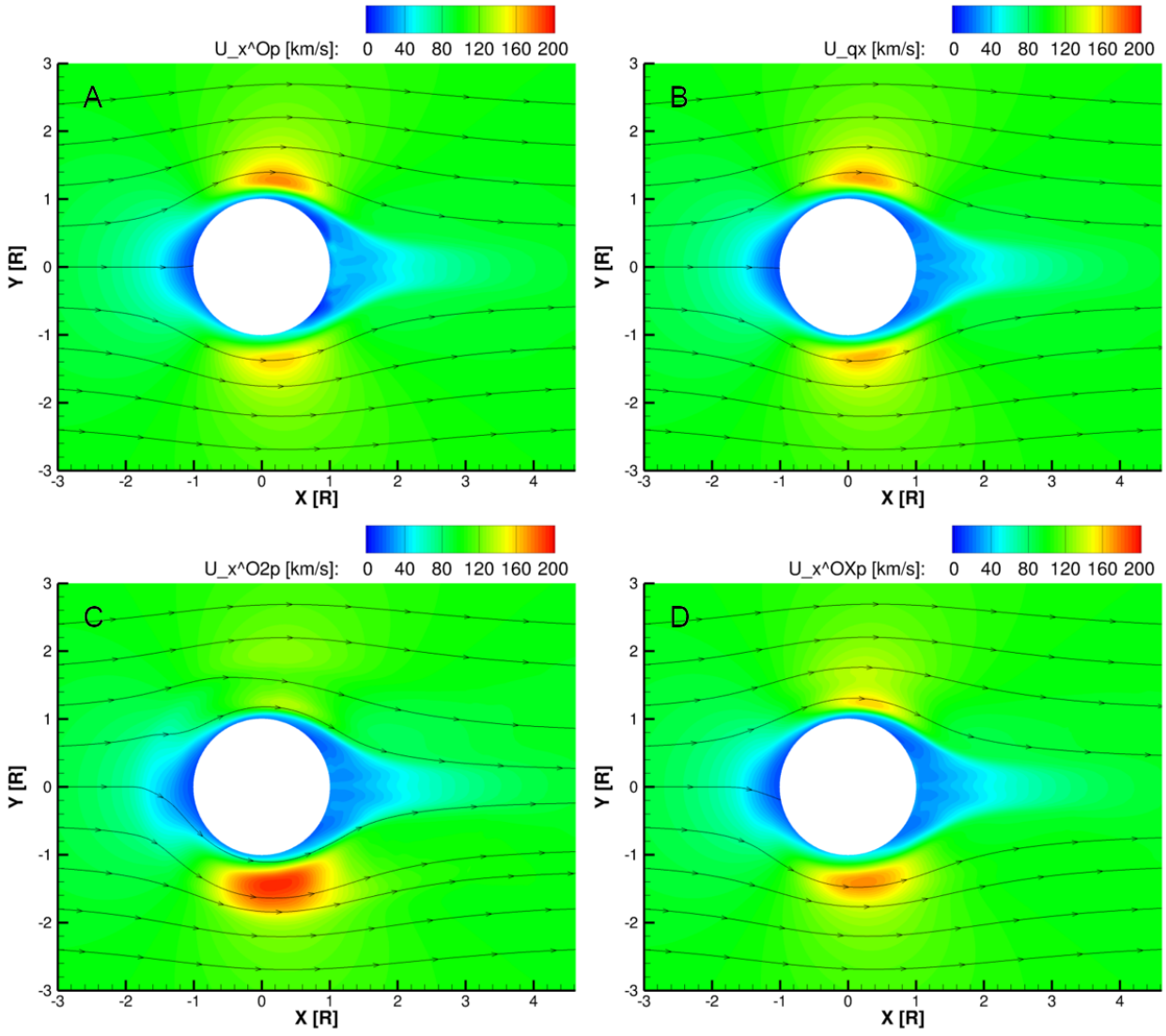

Figure 3.4: Color contours of the X component of the simulated velocity for each ion fluid (A: magnetospheric O^+; C: ionospheric O_2^+; D: ionospheric O^+) and the charge-averaged velocity (B) in the equatorial plane of the case 1, plasma sheet simulation, overlaid with streamlines of the X and Y components of the respective velocities.

In **Figure 3.3** we show the density of each ion fluid and the electron temperature. We see that upstream of the interaction (-X side) the magnetospheric O^+ density increases as magnetic field lines pile up due to the interaction with the cool, dense ionosphere close to Europa's surface. Near the surface O_2^+ and ionospheric O^+ are generated mainly by electron impact ionization of the neutral atmosphere, so their densities are high and the impinging magnetospheric O^+ is partially diverted. On the downstream side of the interaction a wake has formed. The wake is relatively depleted of magnetospheric O^+ and populated with the ionospheric fluids, as we saw in **Chapter 2** for the E4 flyby.

Figure 3.4 exhibits sub- and anti-Jovian asymmetries in the X components of the fluid velocities. The interaction is approximately symmetric close to Europa's surface, in the upstream pile-up region, and in the wake. However, on the flanks the magnetospheric O^+ flows faster around the sub-Jovian side of the interaction while the O_2^+ and ionospheric O^+ flow faster around the anti-Jovian sides. The same asymmetry was observed by Rubin et al. (2015) in their simulation of the E4 flyby. Rubin et al. (2014) investigated similar features in a multi-fluid MHD model for comet-solar wind interactions; while a fluid model is not capable of simulating the full kinetics of particle gyration, they found that multi-fluid MHD does reproduce the separation of the bulk flows of the fluids. In our model, when new ions are introduced by ionization of Europa's extended atmosphere, they are initially cold and immobile. However, the magnetic field flows through the plasma interaction with the charge-averaged velocity, which is dominated by the flow of the magnetospheric O^+ fluid. Therefore, the ionospheric ions have velocity relative to the magnetic field. They are imparted with anti-Jovian directed velocity by the Lorenz force, as can be seen most clearly in **Figure 3.4c** where the O_2^+ streamlines preferentially lean to the -Y direction. Over the flanks the velocity streamlines are compressed due to diversion of the

plasma away from the surface, causing the speed to increase. Because the O_2^+ fluid has been preferentially diverted in the -Y direction the compression is more severe on the anti-Jovian flank, causing the speed to increase more relative to the sub-Jovian flank. This results in the asymmetries seen in **Figure 3.4**.

Figure 3.5 presents altitude profiles of the density of the magnetospheric plasma and of Europa's ionosphere along the upstream line (-X axis) from each simulation. In **Figure 3.5a** the density of the magnetospheric plasma peaks upstream of the moon where the magnetic field lines, and the plasma tied to them, have piled up in front of the ionosphere. The density returns to near-ambient values by ~6240 km (4 R_{Eu}). **Figure 3.5b** shows that the density of Europa's ionosphere peaks near Europa's surface where the plasma is generated by ionization of the neutral atmosphere, then falls off with distance. For the nine simulations presented in this study, the peak ionospheric plasma density near Europa's surface ranges between ~300–2000 cm^{-3}, which falls within the observed range of ionospheric densities from the *Galileo* radio occultation experiment (Kliore et al., 1997; McGrath et al., 2009). In **Figure 3.6** we show the integrated column density of the altitudinal profiles in **Figure 3.5b,** plotted versus the upstream magnetospheric plasma density for each simulation. The Case 3 (high density) simulations produced the densest ionospheres across each location, while the Case 1 (low density) simulations produced the most tenuous ionospheres. Within each case the plasma sheet simulation produced the densest ionosphere.

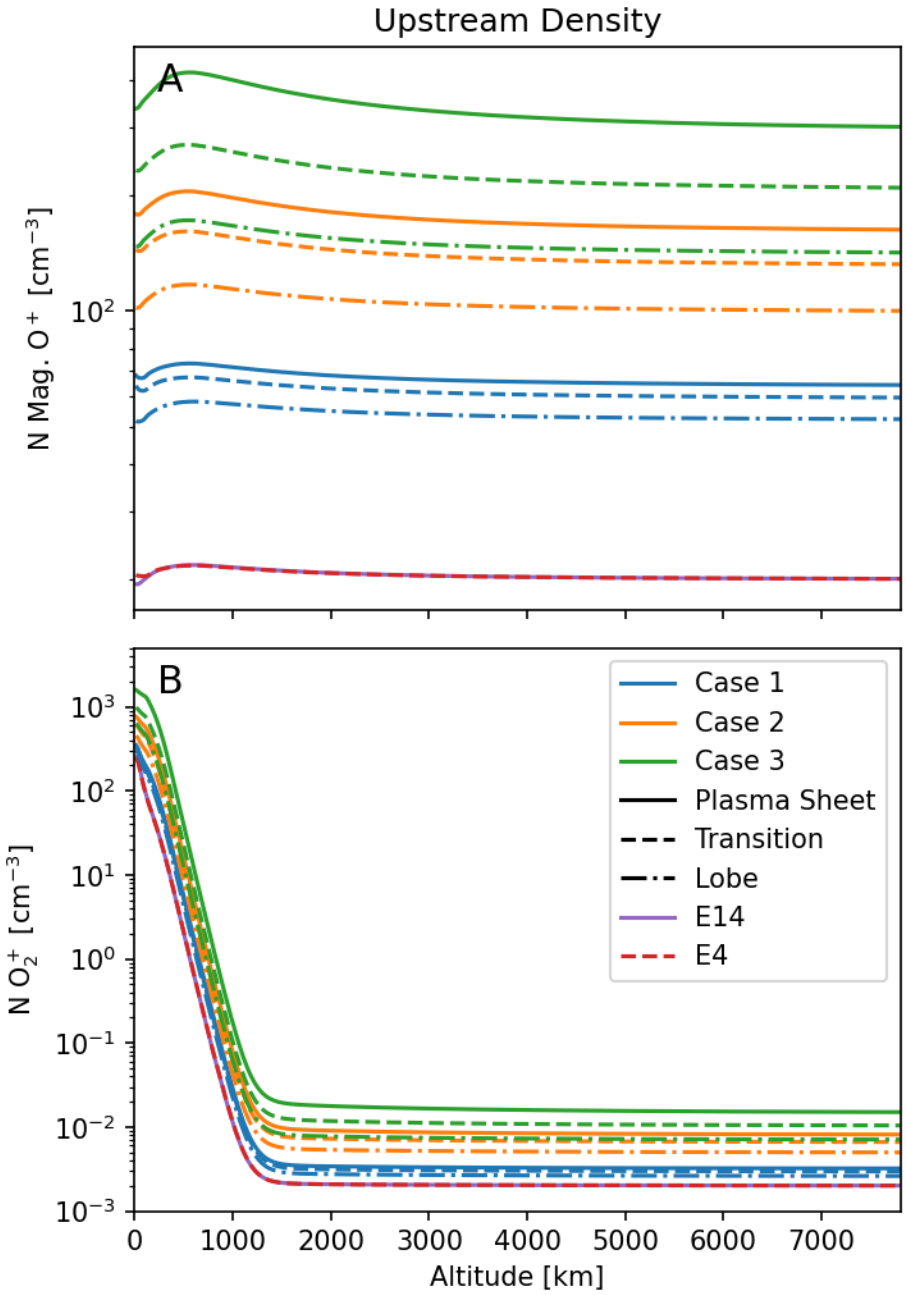

Figure 3.5: Simulated number densities along the -X axis in all simulations for (A) the magnetospheric O+ and (B) the ionospheric O2+ fluids. Blue lines indicate the Case 1 simulations, orange lines indicate Case 2, and green lines indicate Case 3. Solid lines correspond to the simulations in the plasma sheet configuration (19˚ S-III longitude), dashed lines to the transitional configuration (76˚), and dash-dot lines to the lobe configuration (110˚). The flyby simulations are indicated by red dashed lines (E4) and purple solid lines (E14).

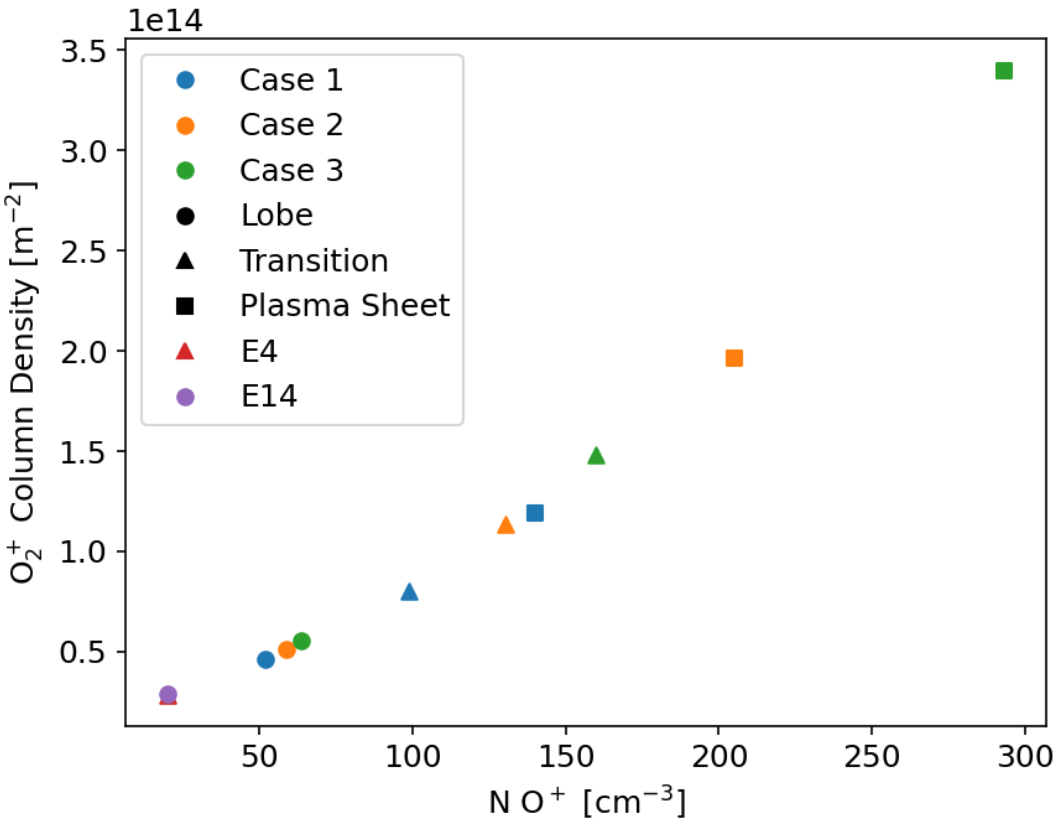

Figure 3.6: Column densities of Europa's ionosphere along the -X axis in all simulations plotted versus the outer boundary magnetospheric O^+ number density. Blue markers indicate the Case 1 simulations, orange markers indicate Case 2, and green markers indicate Case 3. Circle markers correspond to the simulations in the lobe configuration (19° S-III longitude), triangle markers to the transitional configuration (76°), and square markers to the plasma sheet configuration (110°). The flyby simulations are indicated by a red triangle marker (E4) and a purple circular marker (E14).

Figure 3.6 demonstrates that the column density of the ionosphere in each simulation increases with the density of the ambient magnetospheric plasma. The ionospheric plasma is generated mainly by electron impact ionization of the neutral atmosphere, with a minor contribution from photoionization. Therefore, the amount of plasma produced depends on the local density of the neutral atmosphere and, to a large extent, the local electron impact ionization rate. The neutral atmosphere is held constant across all the simulations. The electron impact ionization rate depends on the local electron temperature and density. The electron temperature

at the outer boundary is fixed at 20 eV in all simulations, and it is cooled similarly throughout the neutral atmosphere in all the simulations. However, the electron *density* is calculated to maintain quasi-neutrality with the ions, and therefore varies with the ion density across the different simulations. Since the electron impact ionization rate is directly proportional to the electron density, this causes the density of the ionosphere to increase with the density of the ambient plasma.

3.3 Discussion

The simulations presented in this chapter illustrate the response of Europa's plasma interaction to the driving of Jupiter's magnetospheric plasma at different locations and for different global states of the magnetosphere. The multi-fluid simulations also allow us to obtain a comprehensive description of how the access of magnetospheric plasma to Europa's surface depends on the external magnetospheric conditions, with important implications for surface sputtering by thermal ions. As described previously, Europa's atmosphere is largely sustained by sputtering of magnetospheric charged particles against Europa's ice (see review by Plainaki et al., 2018). Energetic ions tend to sputter with more productive yields per particle, while thermal ions sputter with lower individual yields but with many more incident particles due to the relatively higher density of thermal ions in Jupiter's magnetosphere (e.g., Cassidy et al., 2013; Vorburger and Wurz, 2018). Our multi-fluid MHD model does not simulate energetic particles, but due to the separate tracking of the magnetospheric O^+ fluid it can describe the precipitation of the thermal plasma that contributes to sputtering. Furthermore, with the simulations presented in this chapter we can characterize how thermal plasma precipitation is affected by the electromagnetic fields of the plasma interaction, and how it responds to the range of magnetospheric conditions that Europa experiences.

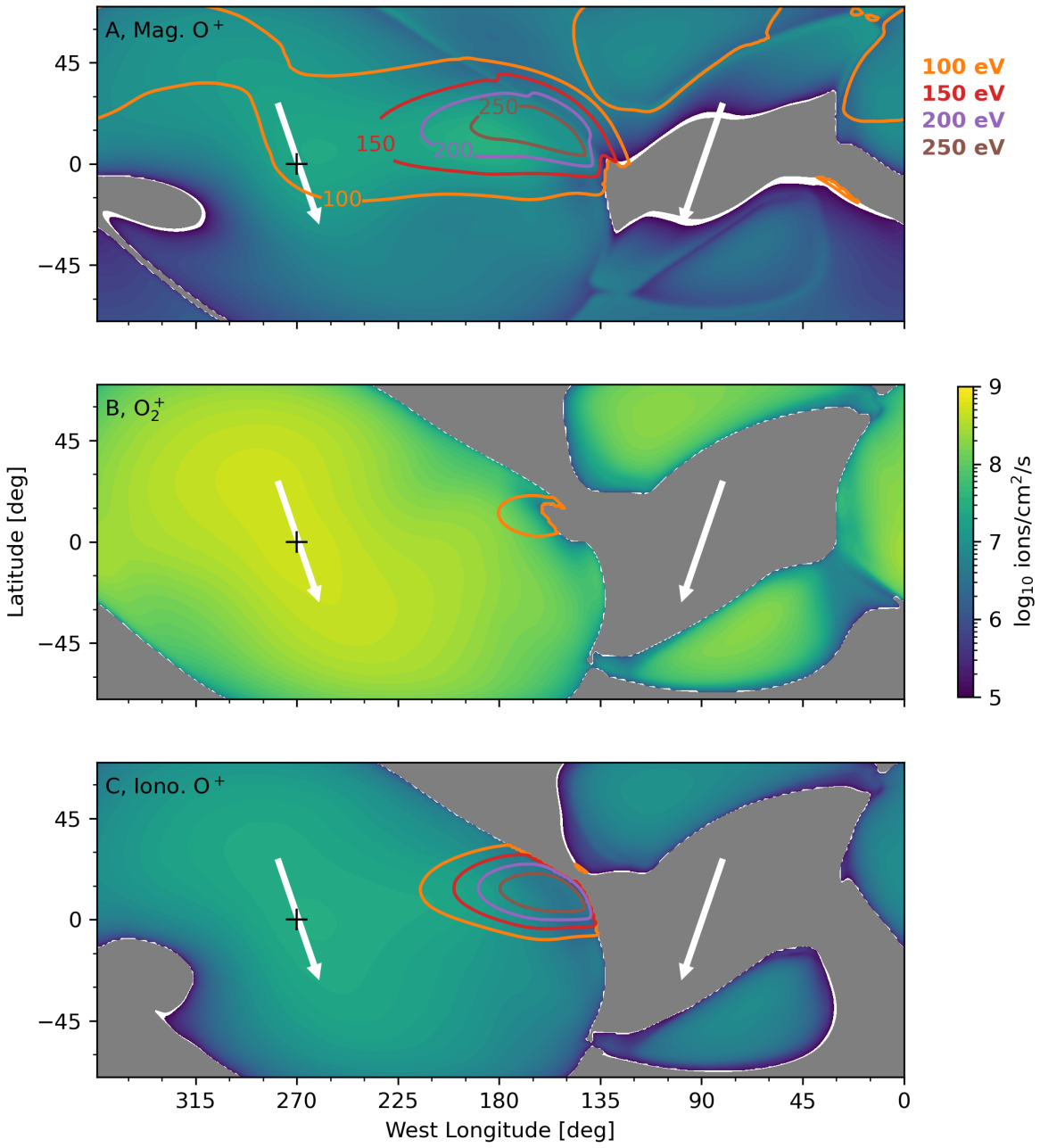

Figure 3.7: Precipitation of individual ion fluids in the E4 simulation. Each panel shows the spatial distribution of downward ion precipitation to Europa's surface. The surface was extracted at R = 1.01 R_{Eu} (15.6 km altitude) at a resolution of 1 point per degree. Gray regions block out upward-traveling ions, while white regions indicate low density precipitation below the color threshold. Black plus symbols mark the center of the trailing/upstream hemisphere at 270˚ West Longitude. The center of the anti-Jovian hemisphere is at 180˚. White arrows at 270˚ and 90˚ longitude show the direction of $B_{J,YZ}$ mapped onto the trailing and leading hemispheres, respectively. In panel A, contour lines indicate the temperature of the precipitating magnetospheric O^+ ions in eV.

3.3.1 Spatial distribution of precipitation

To study the precipitation of plasma onto Europa's surface we interpolated the bulk parameters of the ion fluids, including density, velocity, and pressure, from the 3D simulation results to a spherical surface with radius of 1.01 R_{Eu}. We extract parameters at 1.01 R_{Eu}, leaving a buffer of one layer of grid cells above Europa's true surface at 1.0 R_{Eu}, to avoid potential effects from the imposed inner boundary conditions. In the following discussion we use "flux" to refer to the number of ions passing downward through this spherical surface per unit area, per unit time. We calculate the flux for each ion fluid by multiplying the plasma number density with the radial component of the plasma bulk flow velocity. We then use "precipitation rate" to refer to the total number of ions passing downward through the entire surface per unit time, which we obtain by integrating the above-defined flux of each fluid over the spherical surface area.

In **Figure 3.7** we map the flux of each of the ion fluids from the E4 flyby simulation onto Europa's surface. Cassidy et al. (2013) have previously modeled the flux of magnetospheric plasma to Europa's surface. They traced ions in the vicinity of Europa using simplified assumptions of unperturbed incident plasma flow and uniform Jovian magnetospheric magnetic field, and determined that the result should be a circular bulls-eye pattern of flux centered on the trailing hemisphere. By including the plasma interaction fields self-consistently, our simulations show that while the number flux of all three fluids is, similarly, densest over the trailing hemisphere, the bulls-eye pattern is sheared along the direction of the background magnetic field. The direction of the background magnetic field as it maps onto the apexes of Europa's trailing and leading hemispheres is indicated by white arrows in **Figure 3.7**. The ionospheric fluids (**Figure 3.7b,c**) are much denser near the surface than the magnetospheric O^+ fluid (**Figure 3.7a**), and they precipitate mainly over the trailing hemisphere. **Figure 3.7a** shows the

flux of magnetospheric O^+ onto Europa's surface, which is overlaid with contours of temperature of the magnetospheric O^+ fluid. We find that the temperature of the magnetospheric O^+ tends to increase near the equator, and the hottest patches of flux (greater than 150 eV) are located in the ram to anti-Jovian quadrant (extending from ~ 240˚ West longitude around to 180˚ West longitude). The temperature of the ionospheric fluids (**Figure 3.7b,c**) near the surface does not exceed 100 eV except in small patches near the equator at the anti-Jovian meridian.

Figure 3.8 shows the spatial distribution and temperature of the precipitating magnetospheric O^+ onto Europa's surface in each of the parameter study simulations. We find that the Case 1 simulations, which represent the interaction under high temperature/low density Jovian magnetospheric plasma conditions, exhibit the hottest precipitation, with patches of precipitating plasma hotter than 250 eV over the apex of the anti-Jovian hemisphere. The precipitating magnetospheric O^+ is cooler in Case 2, and cooler still in Case 3 (low temperature/high density conditions). We observe the same trend as the simulations progress within each case from the lobe (where the ambient plasma is sparse and hot) to the plasma sheet (dense and cool). We also observe that the density of precipitating plasma tends to increase in Case 3 relative to Case 1, and in the plasma sheet simulations relative to the lobe simulations.

All of the panels in **Figure 3.8** share common features. We have identified examples of the following features in the bottom-right panel of **Figure 3.8** for the Case 3, plasma sheet simulation with the letters A-D. The points A-D in **Figure 3.8** correspond to the streamlines in **Figure 3.9**, which illustrates how the magnetospheric plasma was transported through the plasma interaction. Magnetospheric O^+ impinges on the upstream side of the moon, penetrating the ionosphere and reaching the surface to form distorted bulls-eye patterns centered on 270˚ longitude (point A). At 90˚ longitude there are grey patches that we use to indicate that the radial

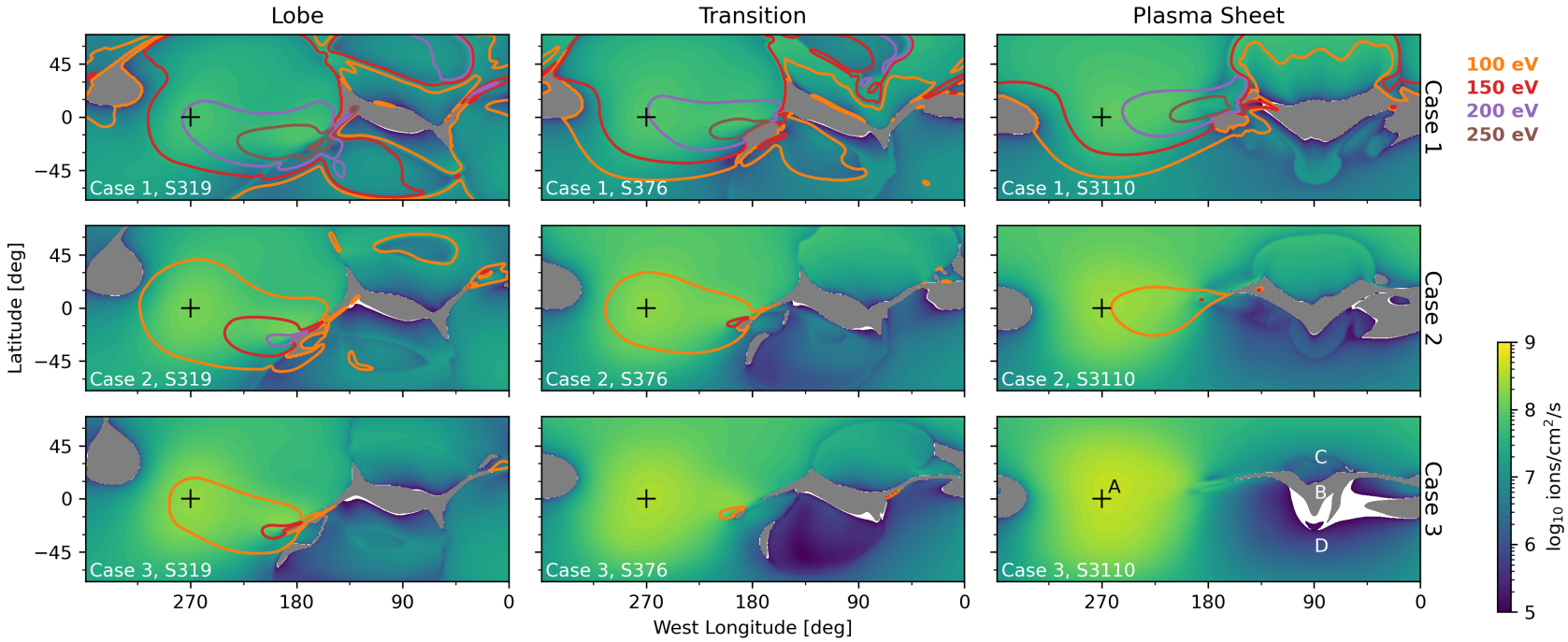

Figure 3.8: Precipitation of the magnetospheric O^+ fluid in the set of 9 parameter study simulations. The format of each panel and the color values are the same as for **Figure 3.7a**. Columns show simulations of the different magnetospheric states, while rows show the lobe, transition, and plasma sheet simulations for each case.

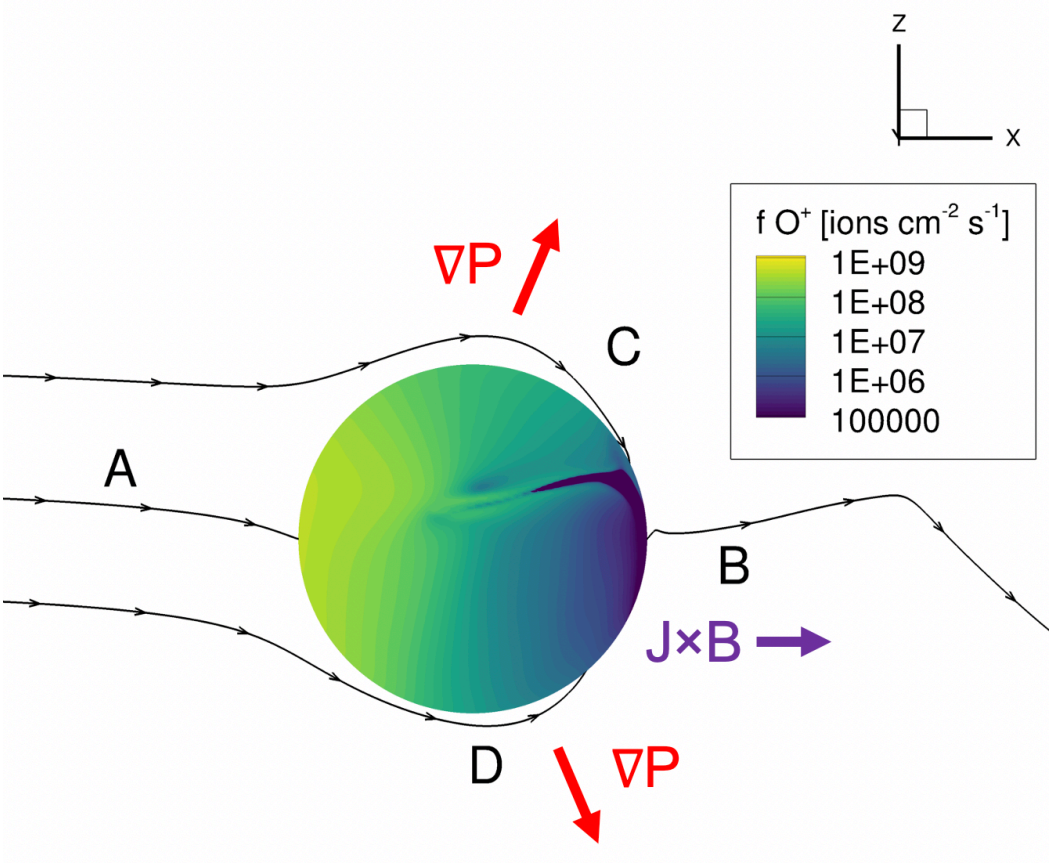

Figure 3.9: Streamlines of magnetospheric O+ in the case 3, plasma sheet simulation. This view looks towards Europa in the +Y direction to observe the anti-Jovian hemisphere. Europa's surface is colored according to the downward flux of magnetospheric O^+. The streamlines are seeded at points on Europa's surface corresponding to the points A-D marked on the case 3, plasma sheet panel in **Figure 3.8**.

velocity component of the magnetospheric O^+ fluid is directed upward, and therefore no downward plasma precipitation occurred (point B). These patches on the downstream side of the interaction are caused by the curvature of the magnetic field lines at the vertex of the Alfvén wings (see **Figure 3.2**). The curved magnetic field geometry leads to currents that flow in the -Y direction; with the mainly southward magnetic field, the currents exert $\vec{J} \times \vec{B}$ force on the MHD fluids that causes them to flow away from the surface. Farther downstream the magnetospheric O^+ rejoins the ambient flow, as illustrated in **Figure 3.3** and **Figure 3.4**, but due to the low density and speed of magnetospheric O^+ near point B it is a negligible source of plasma.

To the north and south of the patches with no precipitation (point B) there are regions of precipitating magnetospheric O^+ on the leading hemispheres at 90˚ longitude (points C, D). These plasmas are carried by the flux tubes that convect from the upstream side over Europa in the +X direction due to the prevailing $\vec{E} \times \vec{B}$ drift. Since Europa's surface and ionosphere do not supply a source of the magnetospheric O^+ ions (see **Figure 3.3a**), there are pressure gradients over the leading/downstream hemisphere that point outward, away from Europa's surface. While plasma convects over Europa, the pressure gradients drive the ambient plasma flows toward the surface where the magnetospheric O^+ pressure is low, parallel to the field line direction in the northern hemisphere, and antiparallel in the south. This causes the magnetospheric O^+ to precipitate onto the surface on the leading/downstream side. We note that in the model of Cassidy et al. (2013) the flux of thermal magnetospheric plasma was limited to the trailing hemisphere, causing the sputtering of O_2 to be limited to the trailing hemisphere as well. Our results indicate that due to the plasma interaction some precipitation does occur on the leading/downstream hemisphere, which should contribute to sputtering of O_2 there.

Every simulation exhibited similar features to those identified by points A-D, though as **Figure 3.8** demonstrates these features are of different shapes, intensities, and temperatures due to the different upstream plasma conditions in each case.

3.3.2 Trends in the total precipitation rate

To measure the precipitation rate of thermal magnetospheric ions to Europa's surface we integrated the downward flux of the magnetospheric O^+ fluid over the R = 1.01 R_{Eu} spherical surface. **Table 3.3** reports the total precipitation of magnetospheric O^+ in each simulation. For comparison, Cassidy et al. (2013) assumed a density of 110 cm^{-3}, speed of 76 km/s, and temperature of ~100 eV for the impinging magnetospheric plasma in their model. Their

parameters are different from the parameters we have used in this study (compare with **Table 3.1**), but the results of the Cassidy et al. (2013) study nevertheless provide a useful point of comparison. They found that the precipitation rate of cold magnetospheric oxygen ions to the surface was 40×10^{24} ions/s. In our parameter study simulations the precipitation rate of thermal magnetospheric ions onto the surface ranges from 5.6–26 $\times10^{24}$ ions/s, while for the E4 and E14 flyby simulations the rate is 1.9×10^{24} ions/s and 1.8×10^{24} ions/s, respectively. In our simulations less plasma reaches the surface because a significant fraction of it is diverted around Europa by the electromagnetic interaction with Europa's ionosphere. We, therefore, consider the results of Cassidy et al. (2013) to be an upper bound on the precipitation rate due to the un-impeded magnetospheric plasma in their model. Our findings show that when the plasma interaction is considered the flux of magnetospheric plasma to the surface is reduced compared to the result of Cassidy et al. (2013), due to the diversion of the upstream flow by the plasma interaction.

Figure 3.10 shows the total precipitation as a function of magnetic latitude and the upstream, ambient ion density. In **Figure 3.10a** we show that for each Case, or state of the global magnetosphere, the precipitation of thermal plasma increases with proximity to the plasma sheet. We also find that the Case 3 (high density/low temperature) simulations see more precipitation than the Case 1 (low density/high temperature) simulations. These trends arise due to the close dependence of precipitation on the upstream ambient plasma density as illustrated by **Figure 3.10b**. Since the precipitation of thermal plasma is used as an input to models for Europa's atmosphere (e.g., Teolis et al., 2017a; Vorburger and Wurz, 2018), the reduction of this precipitation relative to the upstream flux due to the plasma interaction, and its variability, should be taken into account.

Table 3.3: Total magnetospheric O^+ precipitation rate [10^{24} ions/s] in all 9 simulations.

	Lobe	Transition	Plasma Sheet
Case 1	5.6	6.6	7.8
Case 2	9.6	13	16
Case 3	13	19	26

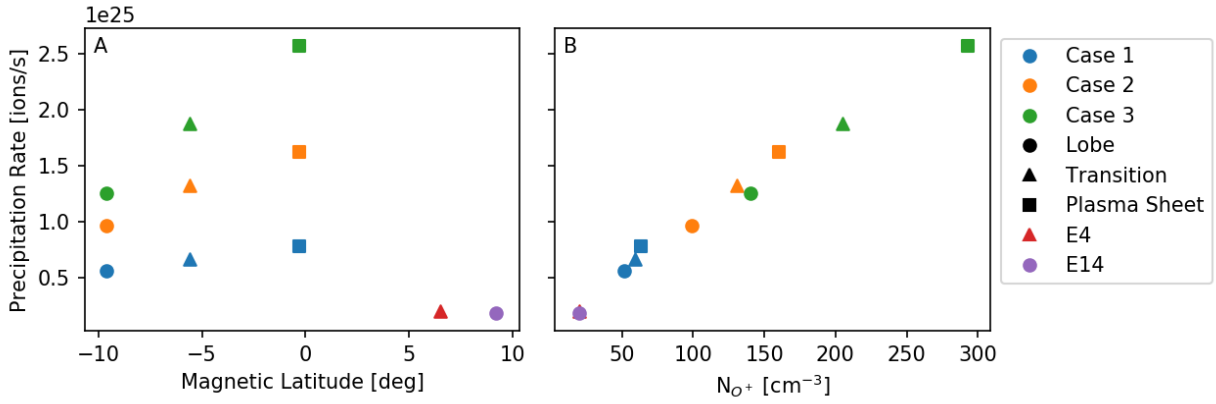

Figure 3.10: Precipitation rate of magnetospheric O^+ versus (A) magnetic latitude and (B) outer boundary magnetospheric O^+ number density. The markers are organized as in **Figure 3.6**.

To understand this dependence, we investigated the diversion of the upstream flow due to the plasma interaction in these simulations. We seeded uniformly spaced 3D streamlines of magnetospheric O^+ velocity on a disc of 1 R_{Eu} radius upstream of Europa at X = -10 R_{Eu}. We then measured the percentage of streamlines that did not intersect the surface of the moon. If the plasma interaction was not present all the streamlines sourced from the disc would have flowed along straight lines through Europa's surface, and none would be diverted. We found that Europa's plasma interaction diverted 88 ± 2% of the impinging magnetospheric O^+ streamlines around the moon in these simulations. This result is consistent with the previous estimate obtained by Saur et al. (1998) using a neutral atmosphere model with similar column densities.

The remaining streamlines reach the surface and the ions streaming along them are counted as precipitation. Since the percentage of diverted streamlines does not vary strongly between the different simulations, the number of precipitating ions is principally controlled by the density of the ambient plasma upstream of Europa.

The consistency of the diversion across all these simulations can be attributed to the feedback loop between the upstream magnetospheric plasma and the ionosphere. When the magnetospheric plasma approaches Europa it may be diverted by the electromagnetic fields of the plasma interaction, but if the magnetospheric plasma is dense enough it will have sufficient momentum to approach Europa's surface where the density of the neutral atmosphere is high. There the magnetospheric plasma will engage in electron impact ionization to produce new ions from Europa's atmosphere. O_2^+ and O^+ ions will be generated at a rate that increases proportionally with the magnetospheric plasma density since the electron impact ionization rate increases with electron density. If the ionosphere had been fixed across all the simulations, the simulations with higher magnetospheric plasma densities and thus more momentum in the magnetospheric plasma would have seen a smaller percentage of diverted streamlines. However, in each simulation the steady-state density of the ionosphere increases with the ambient plasma density due to the dependence of the electron impact ionization rate on the magnetospheric plasma density, as shown in **Figure 3.6**. Thus in simulations where the magnetospheric plasma has more momentum due to increased density, the ionosphere density also increases, so that the ionosphere more effectively slows down and diverts the impinging flow. As a result, the percent of diverted streamlines remained approximately constant over all the simulations.

As an approximation, the magnetospheric ions in our model are assumed to be composed only of O^+. However, S^{2+} ions are also present in Jupiter's magnetospheric plasma at Europa's

orbit (Kivelson et al., 2004; Bagenal and Dols, 2020), and while they have the same mass per charge ratio as O^+, S^{2+} ions tend to sputter more effectively due to their higher mass (Vorburger and Wurz, 2018). Since they are omitted in our current model, any sputtering yield estimated from the precipitation rates presented in this work will likely be underestimated. We additionally note that due to the fluid approximation of the model, our MHD simulations do not capture kinetic effects arising from the gyro-motion of individual charged particles or non-Maxwellian plasma distributions, which may have important effects on estimating the sputtering yields due to the space weathering interaction (Johnson et al., 2009). Therefore, we emphasize that while these results illustrate the range in variability of the precipitation due to external magnetospheric conditions, there are other factors at play that must be accounted for to obtain accurate estimates of sputtering yields.

3.4 Conclusions

In this chapter we presented the results of a parameter study comprised of nine simulations that represent Europa's plasma interaction under different driving conditions in the Jovian magnetosphere. We varied the Jovian magnetic field and bulk plasma properties to model the magnetospheric conditions at three different excursions from the Jovian plasma sheet, and in three different global states of the magnetosphere. This study was designed to range over nominal and extreme conditions for the magnetosphere, thereby producing simulations that represent the possible variations of the plasma interaction.

We examined the trends in precipitation and ion temperature as the Jovian magnetospheric conditions change. We found that the precipitation rate of ions increases with the density of the ambient plasma, while similarly the temperature of the precipitation increases with the temperature of the ambient plasma. However, we note that this result does not account for

changes in Europa's neutral atmosphere, which is expected to vary over time in response to changing solar illumination, changing magnetospheric precipitation, and, potentially, water plumes.

We determined that the total precipitation rate of Jupiter's thermal magnetospheric O^+ ions to Europa's surface ranges from $(1.8–26)\times10^{24}$ ions/s over the parameter space of Jovian magnetospheric conditions that Europa can be expected to experience based on the available observations. These values are significantly smaller than the previous estimate of 40×10^{24} ions/s from the work by Cassidy et al. (2013), which did not include the diversion of the upstream flow due to the plasma interaction. Their result should therefore be considered an upper limit on the precipitation rate.

We conclude that the precipitation of thermal magnetospheric O^+ to Europa's surface is sensitive to changes in the ambient plasma caused by Europa's periodic progression from Jupiter's magnetic lobe to the plasma sheet and back every 11 hours, as well as to changes in the global state of the magnetosphere. The most important controlling factor we identified here for the total precipitation rate was the density of the upstream magnetospheric plasma. These changes in magnetospheric conditions alter the plasma interaction, which controls the density, temperature, and spatial distribution of the precipitating magnetospheric plasma onto Europa's surface. In particular, we have found that thermal plasma can precipitate on the leading hemisphere, though the amount is less than on the trailing hemisphere. Since thermal magnetospheric ions are partially responsible for sputtering neutral O_2 out of Europa's ice and into the neutral atmosphere, this variability should be taken into account in models for Europa's neutral atmosphere.

One element of the plasma interaction which we have not taken into account in this chapter is the variability of Europa's atmosphere. We selected the parameters of the neutral atmosphere for this study based on our model validation efforts using the *Galileo* E4 and E14 flybys (**Chapter 2**) and on previous modeling of the neutral atmosphere. However, it is expected that the density and spatial distribution of the neutral atmosphere will vary with Europa's orbital phase and with Jupiter's synodic period (see review by Plainaki et al., 2018). We consider these effects on the plasma interaction in **Chapter 4** and **Chapter 5**.

Chapter 4 Insights from the *Galileo* E15 Flyby on the Effects of Solar Illumination on Europa's Plasma Interaction

In the previous chapter, we conducted a study of the effects of the changing conditions of Jupiter's magnetosphere on Europa's plasma interaction and the precipitation of thermal plasma to the surface. For that study we held the parameters of Europa's neutral atmosphere constant. However, as described in **Chapter 1**, there are several studies in the literature that expect the atmosphere to change over time.

Europa was situated in the center of the plasma sheet during the *Galileo* E15 flyby, whereas during the E4 flyby Europa was several degrees in Jupiter magnetic latitude above the center of the plasma sheet (Kivelson et al., 2009). Therefore, the external conditions of the magnetospheric plasma and magnetic field were very different during these two flybys. As described in **Chapter 1** and **Chapter 3**, the thermal plasma and energetic charged particles of Jupiter's magnetosphere are ultimately responsible for generating Europa's atmosphere through sputtering. As the plasma conditions were different between the E4 and E15 flybys, it is unlikely that the atmosphere was the same during the two flybys. Roth et al. (2016) analyzed Hubble Space Telescope observations of Europa's oxygen aurora and found variations in the brightness of emissions that could be signatures of this variation with proximity to the center of Jupiter's plasma sheet.

In addition to effects of the magnetosphere, solar illumination is also expected to change the spatial distribution of Europa's atmosphere significantly as Europa orbits Jupiter. Both Plainaki et al. (2013) and Oza et al. (2019) used Monte Carlo simulations to demonstrate that

solar illumination increases the sputtering yield of atmospheric O_2 by heating Europa's ice, causing the neutral atmosphere to vary periodically with the solar illumination conditions as the moon orbits around Jupiter with a long, 84 hour period. They estimated how the density of O_2 and asymmetry of the atmosphere vary as Europa orbits in and out of eclipse, and as the sunlit hemisphere rotates relative to the ram direction of the incident Jovian plasma.

Due to these effects, different configurations between Europa, the Sun, and the flow of Jupiter's magnetospheric plasma can change the spatial distribution and density of the atmosphere in rather complicated ways. For example, when Europa's trailing hemisphere is illuminated (trailing day), the simulations of Plainaki et al. (2013) show Europa's atmosphere to be at its densest because the region receiving the most intense fluxes of thermal plasma and energetic particles is also being heated by solar illumination. Conversely, during the leading day configuration the model predicts an atmosphere that is overall less dense, but enhanced on the leading hemisphere relative to the trailing hemisphere.

The *Galileo* E4 flyby was conducted while Europa was in the trailing day configuration. However, the E15 flyby occurred when Europa was in a trailing dusk configuration. **Figure 4.1** illustrates the differences between the two flyby trajectories and the geometry of solar illumination. Due to these differences, Europa's neutral atmosphere ought to have been very different during the E15 flyby compared to its state during the E4 flyby. The E15 flyby is therefore an appropriate case study with which to investigate the effects of changes in Europa's atmosphere on the plasma interaction.

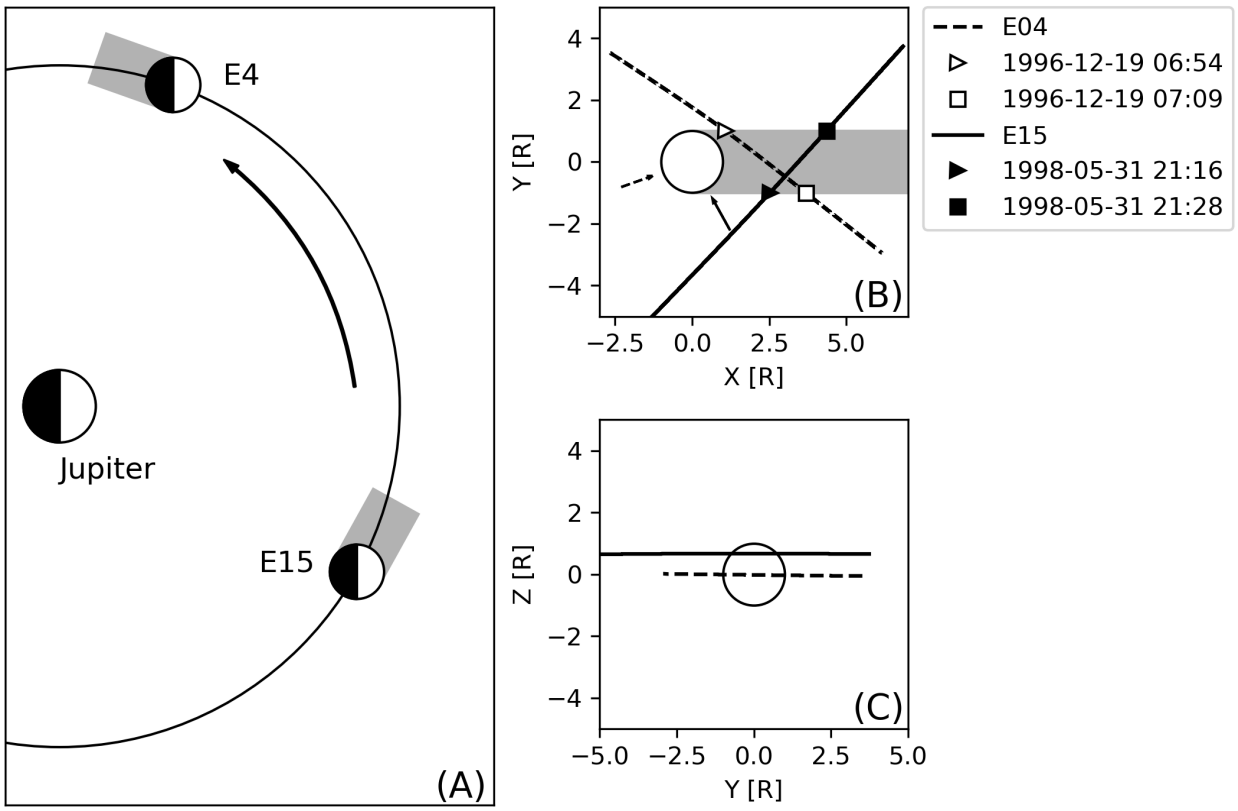

Figure 4.1: Panel A illustrates the configuration of Europa and Jupiter with respect to solar illumination during the *Galileo* E4 and E25 flybys. Panels B and C compare the trajectory of the *Galileo* spacecraft during these flybys.

As described in **Chapter 1**, Europa's atmosphere is intrinsically coupled to the plasma interaction because it provides the source of neutral particles that are ionized to form Europa's ionosphere. Since our model includes this coupling through our implementation of electron impact ionization and charge exchange (See **Section 2.3**), we are equipped to study the effects of changes in Europa's atmosphere on the plasma interaction. We have performed several simulations of the E15 flyby to vary the spatial distribution of the atmosphere and investigate how the modeled magnetic fields along the flyby trajectory are affected. While we were not able to find an atmosphere that modeled the data perfectly, we believe that our results are very

informative in illuminating the effects of illumination-driven atmospheric inhomogeneity on Europa's plasma interaction.

In **Section 4.1** we describe the simulations we conducted to investigate the E15 flyby. In **Section 4.2** we compare the simulations with the *Galileo* data, identify how different features of the atmospheres used in the study affected the plasma interaction, and discuss the extant analysis of the E15 flyby in the literature. We also explain why we consider it unlikely that the E15 magnetometer data include signatures of a water plume. In **Section 4.3** we summarize our conclusions.

4.1 Simulations of the *Galileo* E15 flyby

We conducted several simulations with the same outer boundary conditions but varied the prescribed atmosphere. The Jovian magnetic field and Europa's induced magnetic field were determined by the *Galileo* magnetometer observations during the E15 flyby such that $\vec{B}_J$ = [-66, 31, -380] nT and $\vec{M}$ = [33, -15.5, 0] nT. As was done for the simulations in **Chapter 2** and **Chapter 3**, we set the ambient plasma velocity at the outer boundary to be $\vec{U}$ = [100, 0, 0] km/s. In all other respects, except for the plasma density and the atmosphere, the set-up of the model was identical to that for previous simulations.

For this case study we treated the plasma density differently. In the simulations presented in previous chapters one MHD fluid represented the thermal O^+ plasma of Jupiter's magnetosphere. However, as has been noted previously the composition of Jupiter's thermal magnetospheric plasma includes not only O^+ but also H^+ and S^{2+} (Bagenal et al., 2015). We therefore adjusted the parameters of the model fluids to approximately reflect this composition. We increased the charge of the ambient plasma fluid from 1.0 e to 1.5 e to account for the increased charge contributed by the S^{2+}. Since H^+ is light and S^{2+} is heavy relative to O^+, we

maintained the weight of the fluid to be 16 amu per ion. Based on recent analysis of PLS observations during the E15 flyby, we set the number density of the ambient magnetospheric plasma to be 60 cm^{-3} (Huybrighs, 2018). Assuming that the plasma is quasi-neutral between the ions and electrons, this implies an electron density of 90 cm^{-3}, nearly half the electron density derived from *Galileo* PWS observations (~200 cm^{-3}; Kurth et al., 2001).

The extant data on the upstream plasma conditions for the E15 flyby is limited and somewhat contradictory. Therefore, many possibilities for the external boundary conditions were investigated. During the course of this investigation simulations were performed with the ambient plasma density increased so that the electron density more closely matched the PWS density, but in general this high ambient plasma density caused the simulated magnetic field to be much more perturbed than the magnetometer data. In the end, we used the parameters determined by Huybrighs, (2018) and fixed them for each simulation so that the differences between the simulations could be understood to be caused by the differences in the neutral atmospheres. However, it is possible that different upstream boundary conditions, in combination with the right atmosphere, would more accurately model the flyby. As elsewhere in this thesis, the apparent discrepancies between the *Galileo* PLS and PWS derived plasma densities remain unresolved, and therefore some assumptions are required.

Figure 4.2 shows how the atmosphere varied in each simulation for this study. We label the simulations for this study as follows and describe them further in the subsequent subsections:

- Run 1: E4-like atmosphere
- Run 2: Milillo et al. (2016) atmosphere
- Run 3: Weak base atmosphere with an atmospheric bulge on the leading hemisphere.

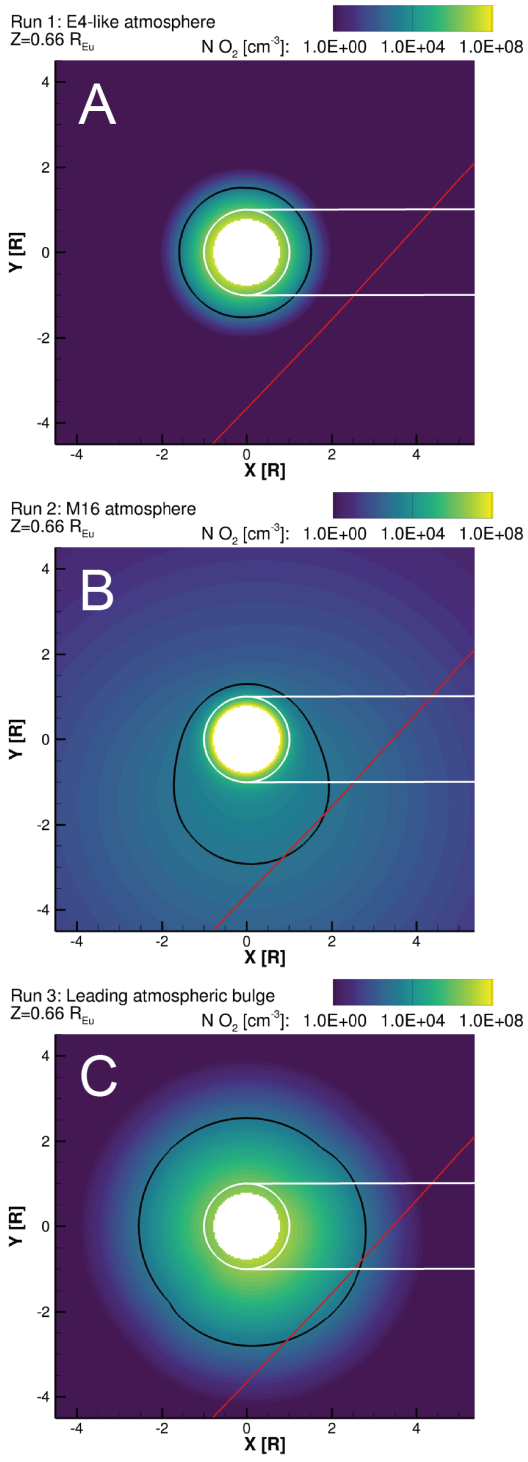

Figure 4.2: The different atmospheres specified for Run 1 (A), Run 2 (B), and Run 3 (C). Each panel shows color contours of the O_2 number density in the E15 plane (Z = 0.66) as prescribed for each simulation. The black contours identify where the density equals 1000 cm^{-3}. The red line shows the E15 flyby trajectory. White lines indicate where R = 1.0 R_{Eu} and the boundaries of the geometric plasma wake at Y = 1.0 R_{Eu} and Y = -1.0 R_{Eu}

4.1.1 Run 1: E4-like atmosphere

We first conducted a simulation where we assumed that during the *Galileo* E15 flyby Europa's atmosphere was unchanged from the E4 flyby. While we consider this scenario unlikely for the reasons described at the beginning of this chapter, it serves as a point of contrast for later simulations. The atmosphere for Run 1 is identical to the atmospheres used for the simulations in previous chapters, with a surface density of $n_0 = 2.5\times10^7$ cm^{-3}, and a scale height of $H_0 = 100$ km, and an enhancement on the trailing hemisphere (A=2).

4.1.2 Run 2: Milillo et al. (2016) atmosphere

Plainaki et al. (2013) simulated Europa's atmosphere under different conditions of solar illumination using a Monte-Carlo model for the irradiation of Europa's surface and the subsequent release of H_2O, O_2, and H_2. Milillo et al. (2016) then fit the model results to a 4-dimensional mathematical function that specifies the density of Europa's O_2 atmosphere in space (3 dimensions) and according to the angle of solar illumination (4th dimension). We conducted Run 2 by specifying the atmosphere with this function, setting the solar illumination angle according to the configuration of Europa relative to the Sun during the E15 flyby.

Figure 4.2b illustrates the density distribution of this atmosphere in an XY cut plane that contains the E15 flyby. In comparison with the atmosphere for Run 1 (**Figure 4.2a**), the Milillo et al. (2016) atmosphere is similarly dense near Europa's surface, with the high density at the surface (~10^8 cm^{-3}) falling by a few orders of magnitude after a few tenths of Europa's radius. Unlike the atmosphere for Run 1, the atmosphere for Run 2 includes a low-density component with a very high scale height. The asymmetry of the atmosphere that corresponds to the angle of solar illumination is expressed by this low density population. In **Figure 4.2b** this asymmetry is

indicated by a black contour line at N_{O2} = 1000 cm^{-3} which shows that the low-density population is enhanced on the anti-Jovian side of the moon.

4.1.3 Leading atmospheric bulge

During this investigation we altered the atmosphere model described by **Equation 2.17** to specify an atmospheric bulge on the leading hemisphere, similar to that predicted by Plainaki et al. (2013). The advantage of this implementation versus the Milillo et al. (2016) atmosphere is the flexibility to independently vary specific aspects of the atmosphere, such as the scale height, as opposed to varying the whole atmosphere at once based on a single parameter. Our method was to test the atmosphere parameters in a simulation and compare the simulated magnetic field and plasma density to the data from the *Galileo* E15 flyby. Then based on discrepancies between the data and the model we adjusted parameters of the atmosphere to improve the comparison. This iterative process entailed over 100 different steady-state simulations of the E15 flyby; here we only present the best result, though the data-model comparison is still imperfect. Because the parameter space for specifying the atmosphere is so large, it may take a significant amount of time to find the optimal parameters of the atmosphere and significantly reduce the error between the data and the model. Nevertheless, we present the results of Run 3 because they exhibit qualitative similarities to the observations of the E15 flyby.

With reference to the parameters listed in **Equation 2.17**, for Run 3 we set the surface density n_0 = 5×10^6 cm^{-3} and the scale height H_0 = 300 km. **Equation 2.17** includes an enhancement, defined by the parameters A and α, that usually represents increased O_2 density on the trailing hemisphere where sputtering is expected to increase. We adapted this enhancement to create an atmospheric bulge on the leading hemisphere, modeling the effects of solar illumination. We increased A, which controls the enhanced density of the atmosphere, from 2 to

4, and calculated α, the angular distance from the center of the enhancement, as centered on 135˚ West longitude, 0˚ latitude, approximately mid-way between the leading meridian and the anti-Jovian meridian (for further description of West longitude, see **Appendix A.4**). In previous simulations, $\alpha = 0$ at 270˚ West longitude and 0˚ latitude, the center of the trailing hemisphere. To select the values for these parameters (n_0, H_0, A, and α), we conducted many simulations and varied the parameters within known constraints. We then compared the model magnetic fields and bulk plasma parameters along the E15 trajectory to the spacecraft data, and selected the simulation that best modeled the flyby.

In general terms, the atmosphere used for Run 3 (**Figure 4.2c**) has a much weaker surface density and a much larger scale height than the atmosphere used for Run 1 (**Figure 4.2a**). The column density of this atmosphere ranges from $(1.5\text{-}7.5)\times10^{14}$ cm^{-2}, falling on the lower end of the range established by Hall et al. (1998). The enhancement that was previously centered on Europa's trailing hemisphere was rotated towards the Sun, and the enhancement was increased to model the effects of solar illumination on the atmosphere in a similar manner to the model of Plainaki et al. (2013). However, whereas the atmosphere for Run 2 (**Figure 4.2b**) specifies a very low density in the asymmetric component far from Europa's surface, the atmosphere selected for Run 3 is still significantly dense even as far away as the distance of closest approach for the E15 flyby (2519.5 km = 1.6 R_{Eu}).

4.2 Results and Discussion

Figure 4.3-4.5 present comparisons of our simulated magnetic fields and plasma densities with the *Galileo* observations for different atmosphere models described above. Before discussing the model-data comparisons, we first highlight the main features in the data that are particularly relevant to understanding Europa's plasma and magnetic environment during the

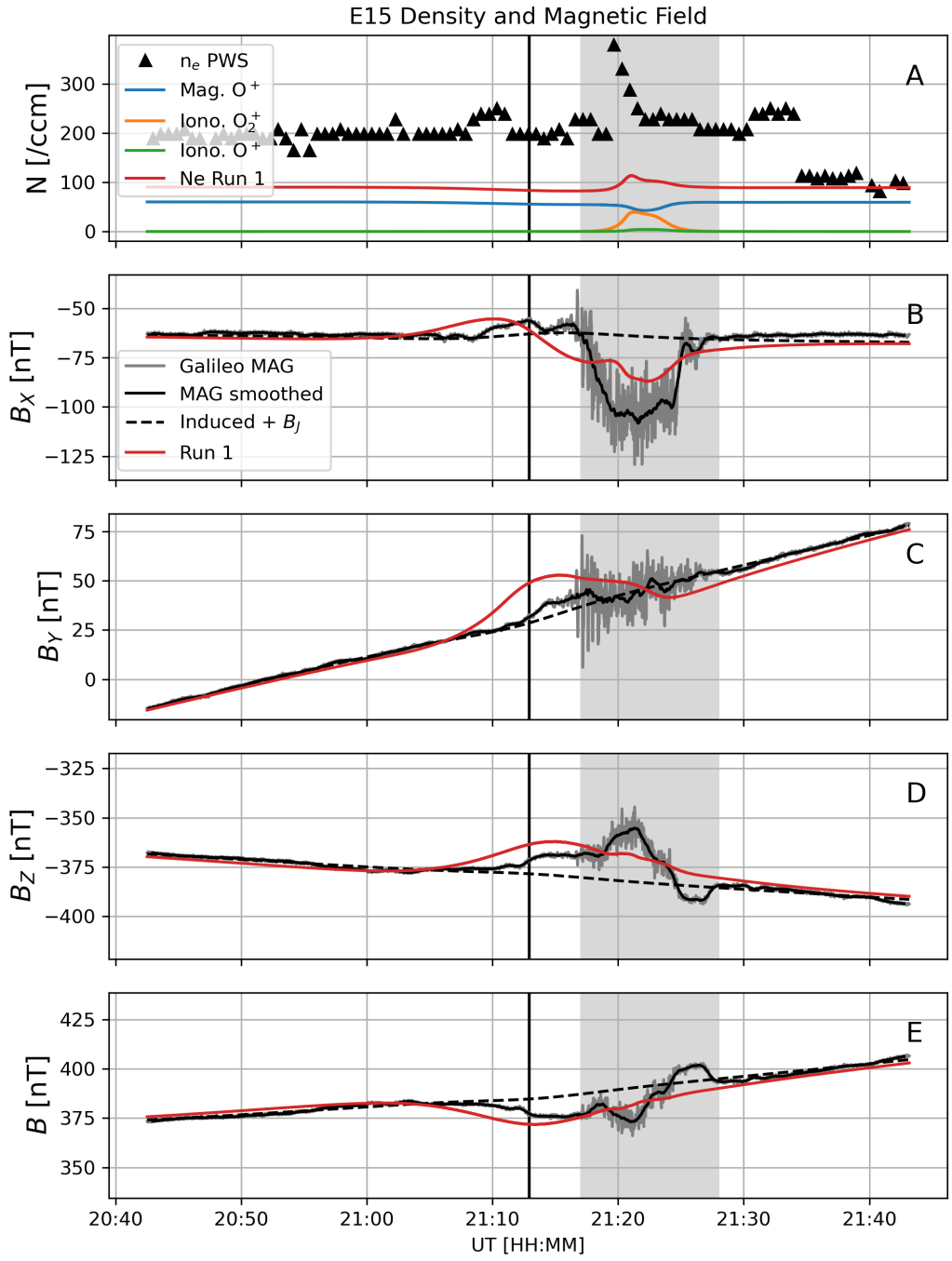

Figure 4.3: Data-model comparison for Run 1. Panel A gives the density of each ion fluid and the electron density along the E15 trajectory. Panels B-D give each magnetic field component, and Panel E gives the magnetic field strength. The vertical black line indicates the time of closest approach, and the grey span indicates the time range that the spacecraft spent in the plasma wake, Y=[-1,1] R_{Eu}. In Panels B-E the solid black line gives a 51-second average of the magnetometer data (grey line).

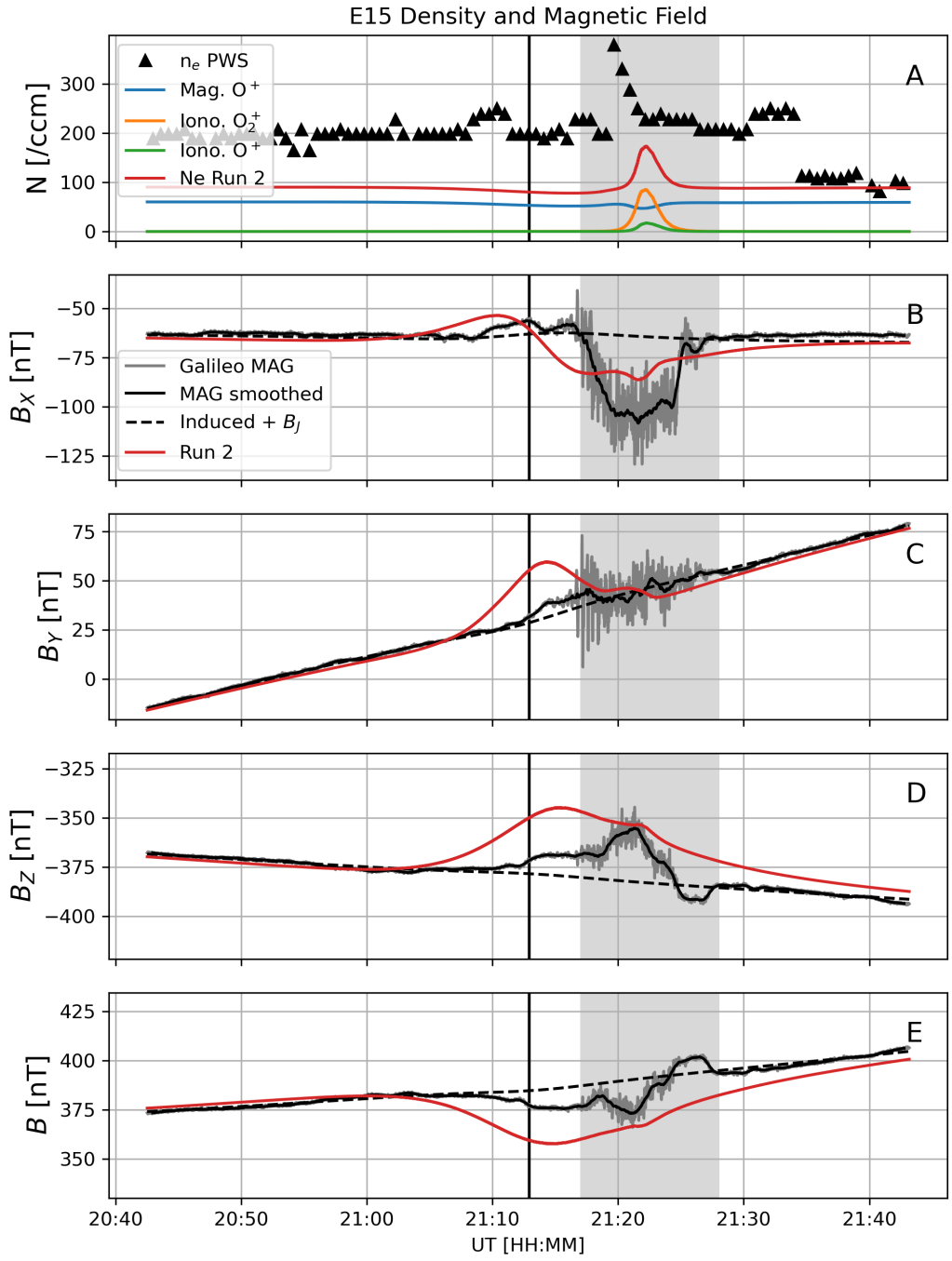

Figure 4.4: Data-model comparison for Run 2. Annotations are as for **Figure 4.3**.

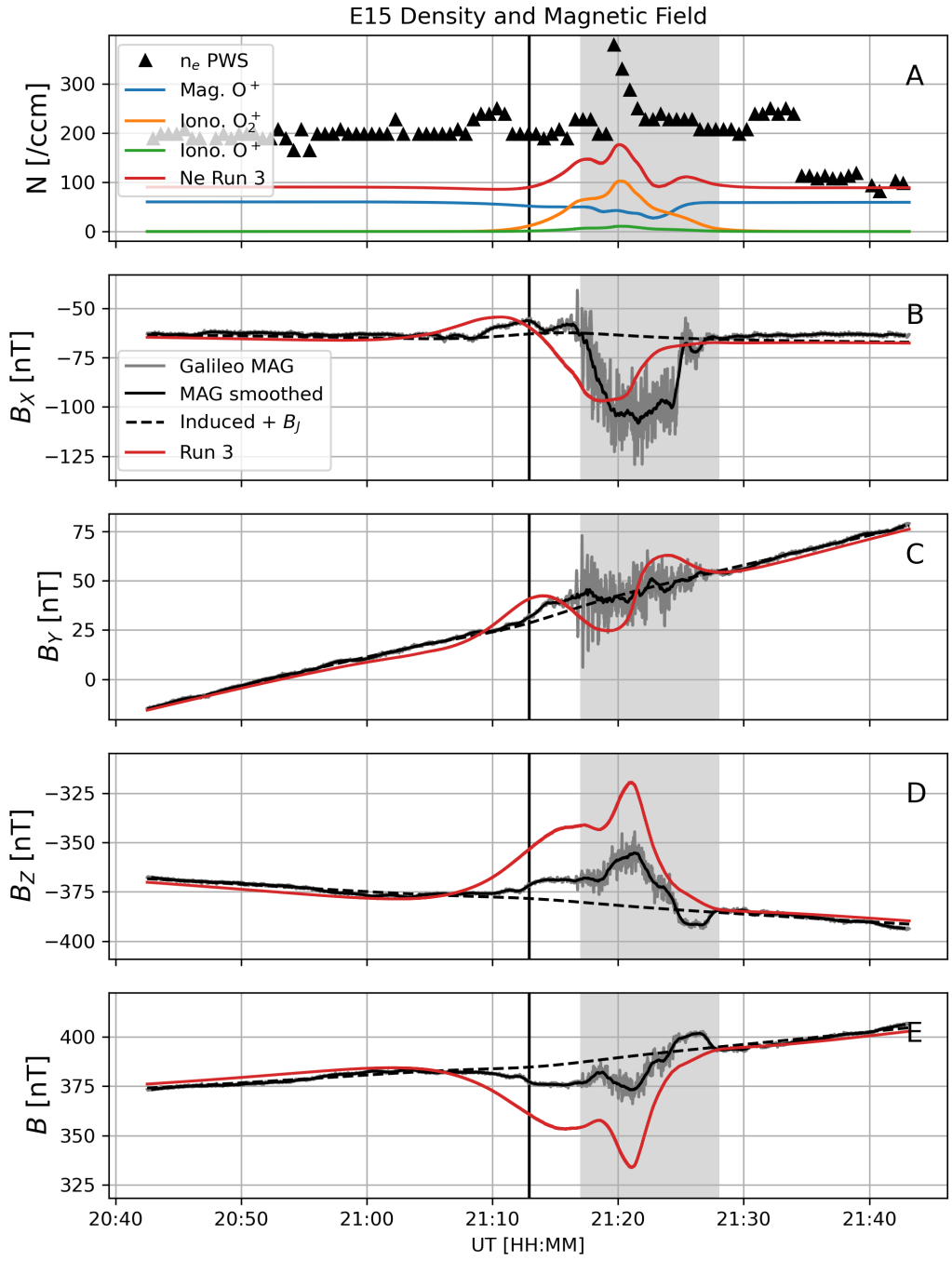

Figure 4.5: Data-model comparison for Run 3. Annotations are as for **Figure 4.3**.

E15 flyby. As can be seen in **Figure 4.3-4.5**, during the E15 flyby the *Galileo* magnetometer observed a broad region of sustained depression of the magnetic field B_X component (~40 nT over ~5 minutes) in Europa's wake. Prior to entering the wake, at the time of closest approach, the B_Z component began a more gradual positive perturbation that peaked in Europa's wake with a maximum perturbation strength of ~20 nT, then recovered to background values as the spacecraft left the wake. While the average values of the B_Y component were almost unperturbed during the flyby, the magnetometer detected strong, high-frequency oscillations as the spacecraft passed through Europa's wake. These oscillations were observed in the B_X component as well, and to a weaker extent in the B_Z component. While there were no published PLS data available for this flyby, the PWS-derived electron densities indicate a sudden increase in the electron density just before UT 21:20, which then quickly return to background values through most of the wake crossing. We discuss the model results and review studies relevant to these features in the following subsections.

4.2.1 Evaluation of the data-model comparisons for Runs 1, 2, and 3

The model magnetic fields of Runs 1 and 2 produced negative perturbations in the B_X component of the magnetic field (**Figure 4.3b, Figure 4.4b**). However, the negative perturbations are shallower than that observed by the magnetometer (~20 nT). **Figure 4.5b** shows that Run 3 produced a negative perturbation in B_X with the right magnitude and duration, but it occurs at an earlier time along the trajectory. **Figure 4.6a-c** shows the B_X component of the model magnetic field in the plane of the E15 flyby for Runs 1, 2, and 3, providing context for the timeseries along the flyby trajectory. We found that varying the azimuthal position of the leading hemisphere atmospheric bulge in the atmosphere was the most important factor in determining

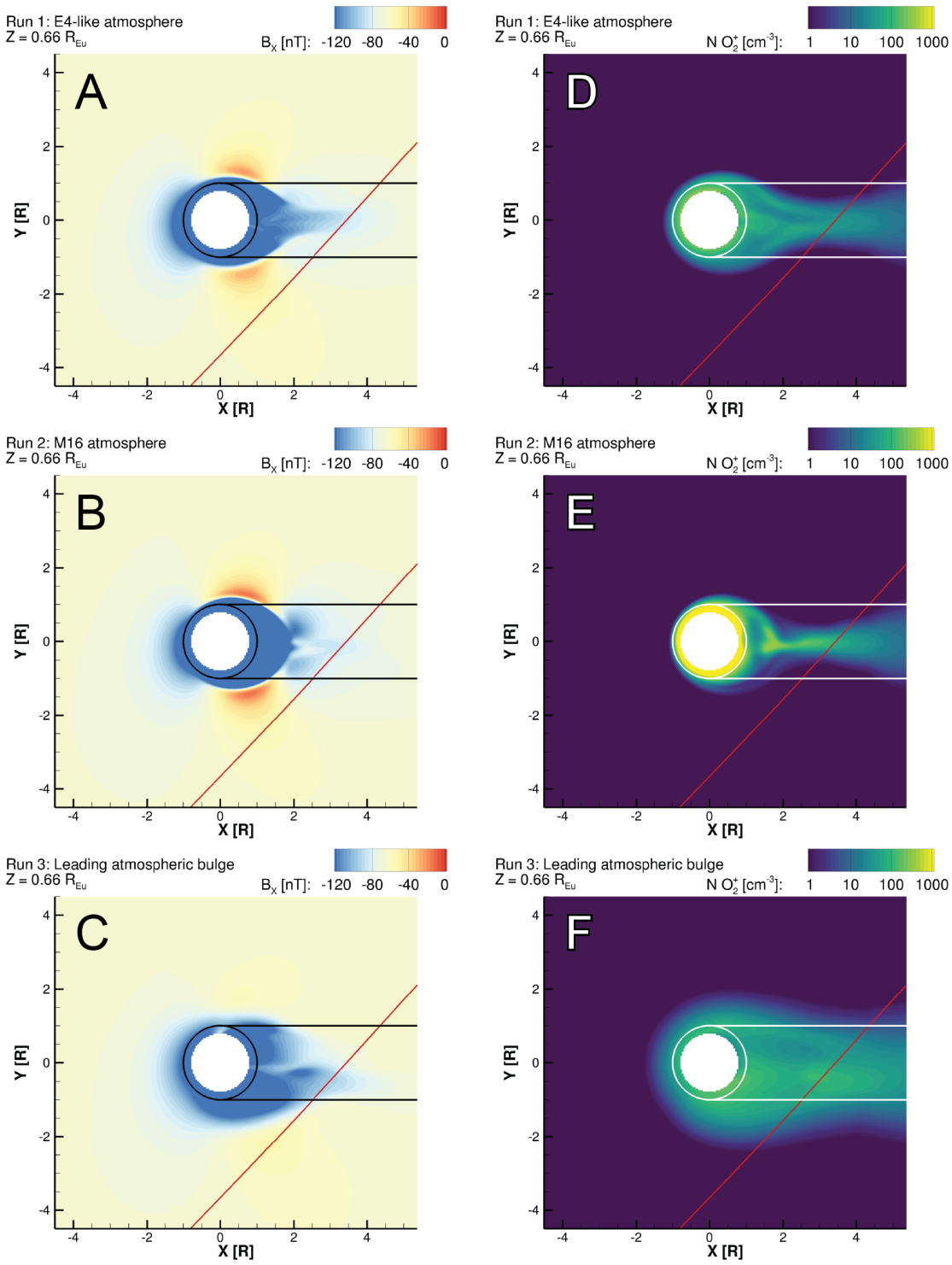

Figure 4.6: The B_X component of the magnetic field for Run 1 (A), Run 2 (B), and Run 3 (C) and the density of the O_2^+ ion fluid for Run 1 (D), Run 2 (E), and Run 3 (F). Each panel shows color contours of the corresponding parameter in the E15 plane (Z = 0.66). Red lines show the E15 flyby trajectory. White lines indicate where R = 1.0 R_{Eu} and the boundaries of the geometric plasma wake at Y = 1.0 R_{Eu} and Y = -1.0 R_{Eu}.

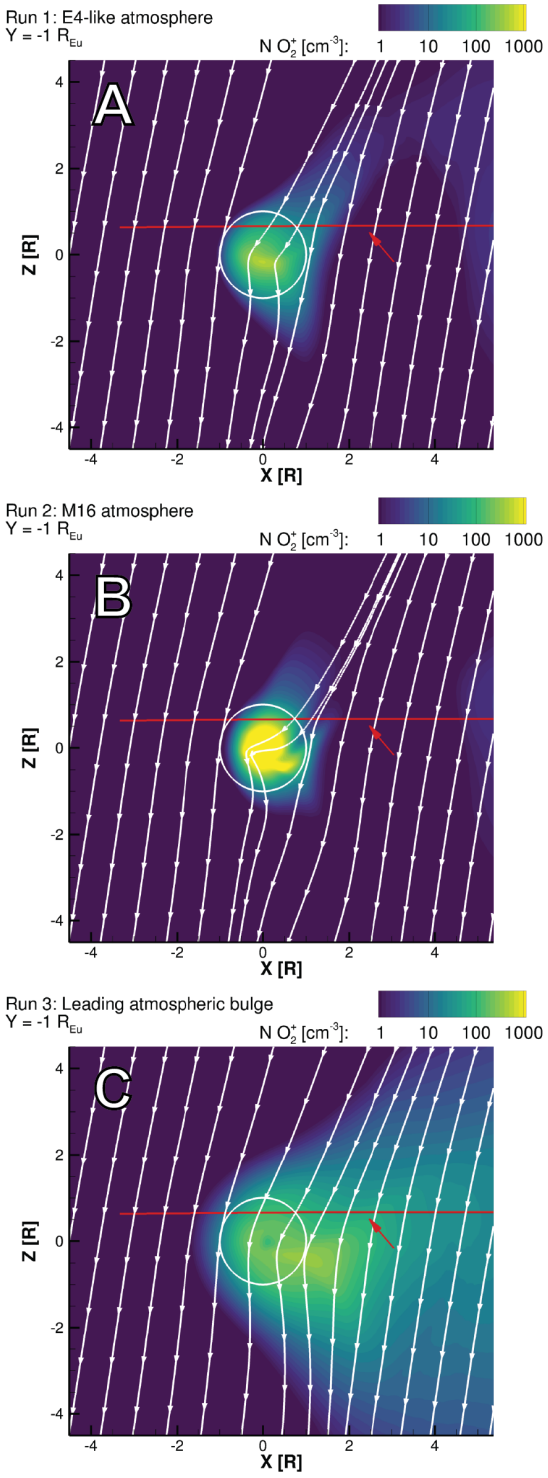

Figure 4.7: The density of the O_2^+ ion fluid for Run 1 (A), Run 2 (B), and Run 3 (C). Each panel shows color contours of the O_2^+ number density in the Y=-1 R_{Eu} plane. Red lines show the E15 flyby trajectory, with the point at which the E15 trajectory intersects the Y=-1 R_{Eu} plane marked with a red arrow. White circles indicate where R = 1.0 R_{Eu}. White streamlines indicate the direction of the parallel components of the magnetic field in the Y=-1 R_{Eu} plane.

where along the trajectory the B_X feature would lie. In Run 3 we note that the negative B_X perturbation occurs in the first half of the spacecraft wake crossing (**Figure 4.6c**) because the atmospheric bulge is located at 135˚ West longitude; therefore the atmosphere is densest in the -Y/+X quadrant (**Figure 4.2c**). **Figure 4.6f** shows the density of O_2^+ in the E15 plane for Run 3, and in particular we note that most of the O_2^+ is produced by electron impact ionization on the -Y side of the plasma interaction due to the relatively high density of the atmosphere there. The loading of mass causes the magnetic field to bend, as shown in **Figure 4.7**, resulting in the negative perturbation to B_X.

This bending is a signature of the Alfvén wing structure of the plasma interaction, with the apex of the bend in the magnetic field located near where mass is loaded onto magnetic field lines as they convect through the plasma interaction. Note that in Runs 1 and 2 the atmospheres are denser near Europa's surface, and therefore the field lines are more acutely bent near where the mass is concentrated (**Figure 4.7a,b**). However, in Run 3 the mass-loading is more spread out due to the large scale height of the prescribed atmosphere. Farther downstream, near where the E15 trajectory intersects this plane, more O_2^+ has accumulated, and therefore the negative perturbation to B_X is stronger and sustained over ~5 minutes in this simulation (**Figure 4.7c)**. The atmospheres used for Runs 1 and 2 did not result in a significant amount of plasma density farther downstream, and therefore B_X is not so significantly perturbed along the E15 trajectory.

For the B_Z component, each simulation produced different results. **Figure 4.3d** shows that Run 1 matches the data to within ~5 nT until the trajectory enters the wake, where the simulated magnetic fields do not exhibit the positive and negative perturbations observed by the magnetometer. The modeled B_Z component for Run 2 (**Figure 4.4d**) is weaker than the magnetic field observed by the data everywhere, at most by ~25 nT just after closest approach. Run 3

(**Figure 4.5d**) also exhibits a weaker B_Z magnetic field, or a stronger positive perturbation, at all points on the trajectory, but notably the shape of the magnetic field perturbation resembles that in the data.

For the B_Y component of the magnetic field, Runs 1 and 2 show a stronger perturbation from background values at closest approach than was observed in the data (**Figure 4.3c, Figure 4.4c**). **Figure 4.5c** demonstrates that in Run 3 the B_Y component was not strongly perturbed at closest approach, in agreement with the data. This was achieved by decreasing the surface density of the prescribed atmosphere.

All of the simulations exhibit peaks in the modeled electron density along the trajectory (**Figure 4.3a, Figure 4.4a, Figure 4.5a**). In all cases there is a shallow depression in the density of the ambient magnetospheric fluid (labeled Mag. O^+ in the plot legends) and the bulk of the peak is caused by enhanced density of the O_2^+ fluid. Run 1 exhibits the smallest peak (**Figure 4.3a**) and Run 2 exhibits the narrowest peak that most closely resembles the data (**Figure 4.4a**), but both are offset by 1-3 minutes, occurring later along the trajectory than the peak in density observed in the data. The peak in density in Run 3 (**Figure 4.5a**) is much broader than that in the data, but the modeled peak is seen at the same location as in the data at UT 21:20.

Figure 4.6d-f provides context for the time series of the magnetic field and plasma density discussed above. We note that because the scale heights of the atmospheres in Runs 1 and 2 are smaller, the modeled density of O_2^+ is more closely confined near Europa's surface and in the narrow plasma wake (**Figure 4.6d,e**). Additionally, because the densest parts of these atmospheres are approximately symmetric near Europa's surface around the Y-axis (**Figure 4.2a,b**), the plasma wake is centered along the X axis. While the low density portion of the Milillo et al. (2016) atmosphere used in Run 2 is markedly asymmetric around the Y-axis, the

density of O_2 at large distances from Europa is so low that it doesn't contribute significant amounts of O_2^+ farther away from Europa (**Figure 4.6e**). By contrast, in Run 3 the large scale height of the atmosphere and the added atmospheric bulge on the leading hemisphere (**Figure 4.2c**) together make more O_2 available for ionization at large distances downstream of Europa. This results in a broad plasma wake with a strong peak in density, and the location of the atmospheric bulge affects the location of the peak in density so that it occurs at the same location along the trajectory that a peak in density was registered by the *Galileo* PWS (**Figure 4.5a**).

4.2.2 Evidence of enhanced ion pick-up during the E15 flyby

The relatively high-frequency oscillations observed in the *Galileo* magnetometer data for the E15 flyby were investigated previously by Volwerk et al. (2001). Those oscillations have been identified as ion cyclotron waves associated with pick up of freshly generated ions in Europa's atmosphere, including a variety of positively charged and negatively charged ions. The authors transformed the magnetometer data into field-aligned coordinates and applied a ray-tracing technique to determine the origin of the wave signatures. They traced the location of the wave source to Europa's leading hemisphere, implying that a significant amount of ionization occurred on Europa's leading hemisphere. The authors also estimated the amount of pick-up during the E15 flyby and compared it to the amount of pick-up during the E11 flyby. They found that more pick-up occurred during E15, and attributed this to Europa's position at the center of the Jovian plasma sheet, whereas during E11 Europa was located outside the plasma sheet (Kivelson et al., 2009). This finding is also consistent with the high atmospheric density on the leading hemisphere predicted by the model of Plainaki et al. (2013) for the solar illumination configuration of the E15 flyby (and illustrated by the Milillo et al. (2016) atmosphere shown in **Figure 4.2b**).

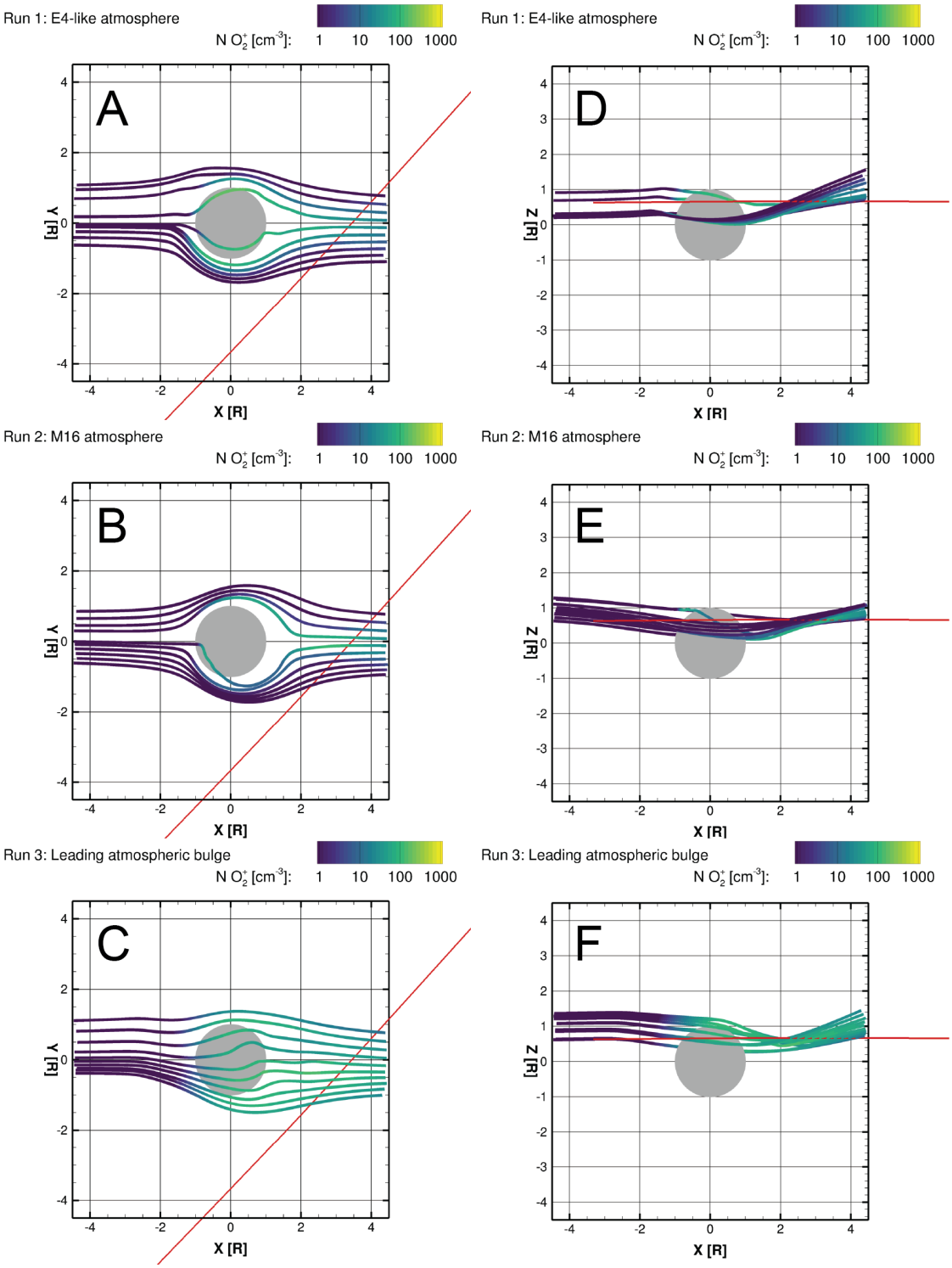

Figure 4.8: Streamtraces of O_2^+ velocity for Run 1 (A, D), Run 2 (B, E), and Run 3 (C, F). Each panel shows 3D streamtraces of the O_2^+ fluid velocity that were seeded on the E15 trajectory during the wake crossing. The streamtraces flow from left to right and are colored according to the density of O_2^+. The E15 trajectory is indicated by a red line. The left panels (A, B, C) show the XY plane, while the right panels (D, E, F) show the XZ plane.

Volwerk et al. (2001) estimated a lower limit for mass loading of O_2^+ in Europa's plasma wake to be 0.08 kg/s. The authors emphasized that, due to the limitations of the ray tracing technique, this estimate only counts the mass loading associated with the ion cyclotron waves emanating from a particular region on Europa's leading hemisphere that reach the spacecraft. For comparison, the global rates of mass loading of O_2^+ in our simulations are 5.6 kg/s for Run 1, 15 kg/s for Run 2, and 10 kg/s for Run 3. To compare the model results with the analysis of Volwerk et al. (2001) in a more qualitative sense, we seeded flow streamlines of the O_2^+ ions along the wake portion of the E15 flyby trajectory, as shown in **Figure 4.8**. We observe that for Run 2 (**Figure 4.8b,e**) none of these streamlines encountered Europa's leading hemisphere; the plasma that appears in the narrow peak in **Figure 4.4a** instead originates primarily from Europa's flanks. In Run 1 (**Figure 4.8a,d**), and more so in Run 3 (**Figure 4.8c,f**), we note that the plasma which forms the peak in O_2^+ density along the E15 trajectory was picked up near Europa's surface and on the leading hemisphere, in general agreement with the conclusions of Volwerk et al. (2001).

4.2.3 Likelihood of a water plume during the E15 flyby

As described in **Section 1.2.4**, water plumes have been implicated as a possible explanation for sudden, strong changes in the magnetic fields of Europa's plasma interaction during the *Galileo* flybys (see, for example, Blöcker et al. (2016) and Arnold et al. (2019) on the E26 flyby, as well as Jia et al. (2018) on the E12 flyby). In these studies plumes were modeled as an enhanced O_2 population that were very localized (a few tenths of Europa's radius in width) and extremely dense relative to the base atmosphere. In the case of Jia et al. (2018), the surface density of the model plume is 2×10^9 cm^{-3} while the surface density of the base atmosphere is 4×10^7 cm^{-3}. The small spatial scale of the model plumes was based on the analysis of Roth et al.

(2014), who estimated the height of a water plume on Europa to be no more than 200 km based on observations from the Hubble Space Telescope (HST). Sparks et al. (2016) analyzed subsequent HST observations with an independent technique and confirmed this estimate.

However, we do not consider a water plume to be a likely explanation for the magnetic field signatures of the E15 flyby. This is because we found that to reasonably model the magnetic field signatures of the E15 flyby required an atmospheric enhancement with characteristic spatial scales much broader than those associated with putative plumes identified in telescopic or in-situ observations (**Figure 4.2c**). Furthermore, **Figure 4.5b-e** show that even an atmosphere with a relatively weak enhancement (in the case of Run 3, by a factor of a few) will produce magnetic field signatures at the distances sampled by the E15 flyby that are more perturbed compared to the data (**Figure 4.5e**). Based on these considerations, we conclude that an atmospheric feature with the general characteristics previously identified in HST images and those used to model water plumes in Europa's atmosphere is not a likely cause for the magnetic field signatures of the E15 flyby.

4.3 Conclusions

As none of the simulations presented here produced magnetic field signatures that match the data observed by the *Galileo* magnetometer, we cannot make any definitive conclusions about the state of Europa's atmosphere during the E15 flyby. However, based on our investigation we can make several observations.

It does not seem likely that Europa's atmosphere did not change between the E4 flyby and the E15 flyby. As described at the beginning of this chapter, Plainaki et al. (2013) predict very different atmospheres for the trailing day configuration of the E4 flyby and the leading dusk configuration of E15 due to the effects of different solar illumination. Our results support this

claim, as our results for Run 1 show that the atmosphere that modeled the E4 magnetic signatures well in the simulation presented in **Chapter 2** did not perform well for the E15 flyby (compare **Figure 2.4** and **Figure 4.3**).

Plainaki et al. (2013) concluded that the densest part of Europa's atmosphere should occur near where the surface is illuminated by the Sun. We implemented the functional form of the corresponding atmosphere as described by Milillo et al. (2016) to evaluate the appropriateness of this model for Europa's atmosphere during the E15 flyby. When evaluated against the *Galileo* data, this atmosphere model improves on the atmosphere for Run 1 in some ways, but doesn't explain all the observations. The density of plasma in Europa's wake increased due to the increased density of the atmosphere near Europa's surface, better resembling the densities derived from the *Galileo* PWS data (compare **Figure 4.3a, Figure 4.4a**). However, this high concentration of mass-loading near Europa's surface caused the magnetic perturbations near closest approach in B_Y and B_Z to significantly exceed the perturbations observed by the data (**Figure 4.6b**).

Because the Milillo et al. (2016) atmosphere is controlled by a single parameter, the angle of solar illumination, this atmosphere cannot be varied to account for other effects such as the plasma conditions in Jupiter's magnetosphere. Therefore, while it is a useful tool for understanding how the atmosphere is likely to vary as Europa moves to different local times with respect to Jupiter and the Sun, it does not appear to be suitable to model the specific conditions of the E15 flyby. In developing the atmosphere model for Run 3, we were informed by the results of Plainaki et al. (2013) to design an atmosphere with an atmospheric bulge collocated with solar illumination, but freely varied the shape and magnitude of the atmospheric bulge and the underlying base atmosphere. We then iteratively varied the atmosphere and evaluated the

simulation results against the *Galileo* data to understand how different aspects of the atmosphere control the signatures of the plasma interaction.

Because of lack of direct observational constraints and the large number of free parameters involved in specifying the atmosphere distribution, there is a vast parameter space to explore in order to fully understand how asymmetries in the atmosphere would affect Europa's interaction. In this project we have conducted a number of simulations using different atmosphere models. While some simulations yielded good model-data comparisons for some of the features in the data, none of the simulations presented here were able to explain all of the main features identified in the data. Nonetheless, the results of Run 3 demonstrate that an atmosphere with a leading atmospheric bulge, consistent with the observations of Volwerk et al. (2001) and similar to the atmosphere determined by Plainaki et al. (2013), has the potential to explain the features of the E15 flyby. With continued exploration of the parameter space of different likely atmospheres for Europa, improved understanding of how changes in the atmosphere affect the magnetic fields of the plasma interaction, and closer integration with models for Europa's neutral atmosphere, we expect a high-quality solution will eventually be identified in future work.

Chapter 5 Effects of Variation in Europa's Atmosphere on the Plasma Interaction

Europa's plasma interaction is inextricably coupled to its atmosphere. As demonstrated by the results presented in **Chapter 4**, while the physical mechanisms that couple Europa's atmosphere to the plasma interaction are reasonably well understood, in practice it is difficult to predict how changes in the neutral atmosphere will affect the 3D magnetic fields and bulk plasma properties of the plasma interaction. Therefore, to better understand this system we must characterize how changes in the atmosphere affect the plasma interaction by systematically exploring the parameter space of reasonable variation in the atmosphere.

In **Chapter 4** we investigated how changes in the atmosphere caused by solar illumination of Europa's icy surface could have affected the plasma interaction during the *Galileo* E15 flyby. The central mechanism for these atmospheric changes is that solar illumination increases the yield of neutral particles from each sputtering interaction by increasing the temperature of the ice. Another mechanism that increases the total amount of sputtered particles, and therefore affects the atmosphere, occurs when Europa is bombarded by a higher flux of impinging particles from Jupiter's magnetosphere.

In **Chapter 3** we demonstrated that the flux of thermal plasma impinging on Europa's surface increases with the density of the ambient plasma of Jupiter's magnetosphere. Various models for the neutral atmosphere attribute a significant fraction of neutral O_2 to sputtering by thermal plasma (e.g. Cassidy et al., 2013 and Vorburger et al., 2018). Therefore we would expect the density of Europa's atmosphere to increase when Europa is located at the center of Jupiter's dense plasma sheet (Bagenal et al., 2015), or when the global state of Jupiter's magnetosphere is

such that the density of the ambient plasma at Europa's orbit is elevated. The latter may occur in connection with increased volcanic activity at the inner Galilean moon Io, which provides the primary source of thermal plasma in Jupiter's magnetosphere (Bagenal et al., 2020; Yoshioka et al., 2018).

However, most of the O_2 in Europa's atmosphere is likely generated in sputtering interactions between energetic ions and electrons and Europa's icy surface (Johnson et al., 2009). Jupiter's magnetosphere is populated with energetic charged particles with energies ranging from several keV to tens of MeV (Paranicas et al, 2009). Energetic particle populations in Jupiter's magnetosphere have been shown to change on time scales of years and decades (see, for example, the depletion in ring current ion populations during the *Galileo* mission era discussed by Mauk et al., 2004). Short time-scale variations can be caused by energetic particle injections (e.g. as recently observed by the *Juno* spacecraft and reported by Mauk et al., 2020). Therefore, we anticipate that the populations of sputtering particles at Europa, including thermal ions and energetic electrons and ions, will be variable in time, and therefore can cause the density of Europa's atmosphere to vary.

Remote observations of Europa's oxygen aurora place constraints on the column density of the atmosphere of $(2.4–20)\times10^{14}$ cm^{-2} (Hall et al., 1995; 1998). Assuming a hydrostatic structure of the atmosphere, the column density can then be decomposed into two parameters: surface density and scale height. The surface density and scale height of the atmosphere must be varied with each other to constrain the column density within the reasonable range. However, neither of these parameters have been definitively constrained independantly. Roth et al. (2016) estimated the scale height to be ~100 km based on HST observations, while Monte Carlo type

models for the atmosphere have predicted scale heights as low as 20 km (see, for example, Cassidy et al., 2007, and others cited in the recent review by Plainaki et al., 2018).

In recent years models for Europa's plasma interaction have prescribed atmospheres with a wide range of parameters, employing different surface densities and scale heights as well as different degrees of asymmetry between the trailing and leading hemispheres. The result is that between different models the atmosphere density may vary by an order of magnitude or more at the same location. For example, the density of O_2 at the apex of Europa's trailing hemisphere, including the sputtering enhancement, is 1.5×10^9 cm^{-3} in the simulations presented by Rubin et al. (2015), 1.2×10^8 cm^{-3} in the simulation of Jia et al. (2018), 1×10^8 cm^{-3} and 1×10^9 cm^{-3} in the two cases presented by Arnold et al. (2019), and 7.5×10^7 cm^{-3} in the simulations presented in **Chapter 2** and **Chapter 3**.

In this chapter we study the effects of variation in Europa's atmosphere on the plasma interaction. As in **Chapter 3**, we pay particular attention to the effects on the precipitation of thermal plasma onto Europa's surface. To accomplish this we conducted a parameter study bounded by the existing observations of the atmosphere. In **Section 5.1** we describe the setup of the simulations and the parameters that were varied for the study. In **Section 5.2** we present and compare the results from each simulation. In **Section 5.3** we discuss the effects of the different properties of the atmosphere on the generation of Europa's ionosphere, and on the precipitation of thermal plasma. In **Section 5.4** we present our conclusions.

5.1 Methods

To better understand how changes in Europa's atmosphere affect the plasma interaction we conducted several simulations to span the parameter space of reasonable atmosphere

variation for Europa. The setup of these simulations differs in two ways from the previously shown simulations: grid resolution refinements, and the atmosphere parameters.

In previous simulations the minimum grid resolution near Europa's surface was ~15 km (**Figure 2.1**). Since we decided to study atmospheres with small scale heights of 33 km, we added a layer of refinement such that the cells closest to Europa's surface are ~7 km long, allowing for about 4 layers of cells inside the first 33 km of the atmosphere.

The other difference is that in prescribing the atmosphere we have included the secondary population of O_2 described in **Equation 2.11** by the parameters n_1 and H_1. In the simulations with atmospheres of small scale heights in the primary population (H_0) the density of O_2 falls off quickly with distance. Therefore, to avoid unphysically low densities at large distances from Europa we applied the secondary population, setting the parameters equal to $n_1=4\times10^3$ cm^{-3} and H_1=600 km. These parameters were selected to model the tall scale height O_2 population shown in the results of Teolis et al. (2017a), Figure 5.

Most parameters of the simulations shown in this chapter were held constant across the study. At the outer boundary of the simulation we set the ambient plasma velocity to [100, 0, 0] km/s. To simplify the analysis of the simulation results and eliminate asymmetries associated with the magnetic environment, we set the Jovian magnetic field to B_J=[0, 0, -400] nT and correspondingly did not include Europa's induced field. Thus the trends observed between the different simulation results are all due to variations in the atmosphere and the self-consistent generation of the ionosphere. We set the charge of the ambient magnetospheric plasma fluid to 1.5 e as described in **Chapter 4**, and the temperature of the ambient plasma to 129 eV. The properties of the electrons and the calculation of source and loss terms associated with ionization, recombination, and charge exchange, as well as other numerical details, are the same

as described in **Chapter 2**. The parameters that *do* vary between the different simulations are the ambient plasma density and the primary component of the atmosphere (n_0 and H_0).

The parameter study consists of 18 simulations covering the variation of three parameters. First, we varied the ambient plasma density such that nine simulations were conducted with a low ambient density of 20 cm^{-3}, and nine with 100 cm^{-3}. Our choice of low ambient plasma density corresponds to the density observed by the *Galileo* PLS during the E4 flyby (Paterson et al., 1999). Our choice of high plasma density is more consistent with the densities derived from the *Galileo* PWS observations over many flybys, and may be a more nominal case for the magnetospheric plasma density at Europa's orbit (Kurth et al. 2001; Bagenal et al., 2015).

Within each of the two sets of simulations, we varied the scale height of Europa's atmosphere to be either 33 km, 100 km, or 330 km. We then varied the surface density of the atmosphere to be either 2.5×10^7 cm^{-3}, 5.0×10^7 cm^{-3}, or 7.5×10^7 cm^{-3}. **Figure 5.1** illustrates how these nine different atmospheres span the range of Europa's column density determined by Hall et al. (1995; 1998), and **Table 5.1** gives the average, minimum, and maximum column densities for each atmosphere. The observations used by Hall et al. (1995; 1998) to determine this range were conducted in 1994 and 1996, and therefore if the structure of the atmosphere varied over this time period the range would encompass that behavior. Note that the two atmospheres in this study with the most extreme column densities (the lowest and the highest) fall outside the ranges established by Hall et al. (1995; 1998). The simulations that use these atmospheres provide edge cases and upper/lower bounds on the results.

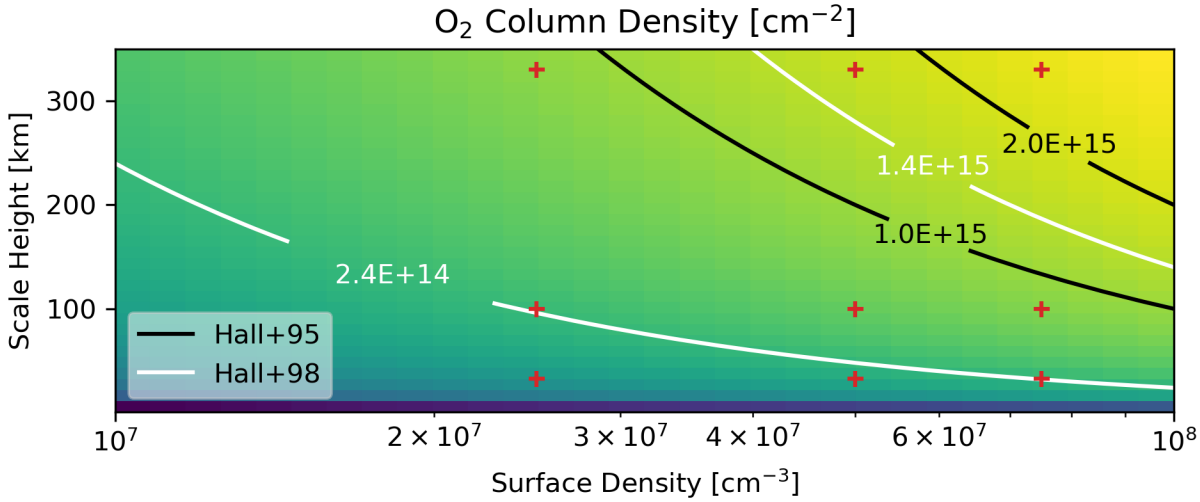

Figure 5.1: Probable O_2 column densities for Europa's atmosphere. Black and white contours describe the upper and lower limits on the column density of Europa's atmosphere determined from observations of Europa's oxygen aurora by the HST (Hall et al., 1995; 1998). Red pluses mark the column density of the primary atmosphere component for each simulation in the parameter study.

Table 5.1: O_2 column density over Europa's surface for each of 9 atmospheres in the parameter study. In each cell we give the average column density over the whole surface followed by the minimum and maximum column densities in parentheses. In each atmosphere the maximum occurs at the apex of the trailing hemisphere, while the minimum occurs on the leading hemisphere.

Av. (Min.–Max.) [10^{14} cm^{-2}]	Low surface density, 2.5×10^7 cm^{-3}	Medium surface density, 5.0×10^7 cm^{-3}	High surface density, 7.5×10^7 cm^{-3}
Large scale height, 330 km	11.6 (8.25–24.8)	23.2 (16.5–49.5)	34.7 (24.8–74.3)
Medium scale height, 100 km	3.51 (2.50–7.51)	7.02 (5.00–15.0)	10.5 (7.50–22.5)
Small scale height, 33 km	1.16 (0.83–2.48)	2.32 (1.65–4.96)	3.48 (2.48–7.43)

5.2 Results

Figure 5.2 and **Figure 5.3** show the density of O_2^+ in the equatorial plane for, respectively, the simulations with low and high ambient plasma density. In the simulations O_2^+ is the primary component of Europa's ionosphere and indicates its boundaries and features. In general, we see that the simulations with high ambient plasma density (**Figure 5.3**) developed denser ionospheres; this is in agreement with the results of **Chapter 3**, where we found that the column density of the upstream ionosphere increased approximately linearly with the ambient plasma density (**Figure 3.10**). In both **Figure 5.2** and **Figure 5.3** we see that the simulations with the largest scale height atmospheres extend far from Europa's surface and load the plasma wake with higher densities of ions (top rows of **Figure 5.2** and **Figure 5.3**). Where the atmosphere scale height is small, the ionosphere is confined close to Europa's surface.

Figure 5.4 and **Figure 5.5** show the B_Z component of the magnetic field and streamlines of the charge-averaged velocity U_q in the equatorial plane. The simulated perturbations are roughly symmetric around the X-axis as a result of our choice of symmetric Jovian background field as input for all simulations presented here. For these simulations the strength of perturbations to B_Z primarily indicate the strength of the disturbance that the ionosphere presents to the ambient flow of plasma. Indeed, we see that in **Figure 5.4**, which shows the simulations with low ambient plasma density, the upstream magnetic field pile-up (red) is weaker than in **Figure 5.5**, which shows the simulations with high ambient plasma density and consequently higher ionosphere densities. In both figures we observe that the spatial extent of the upstream magnetic field pile-up, as well as the distance from Europa's surface at which streamlines start diverting from their ambient, straight paths, increases with the scale height of the atmosphere, and the subsequent increased extent of the ionosphere.

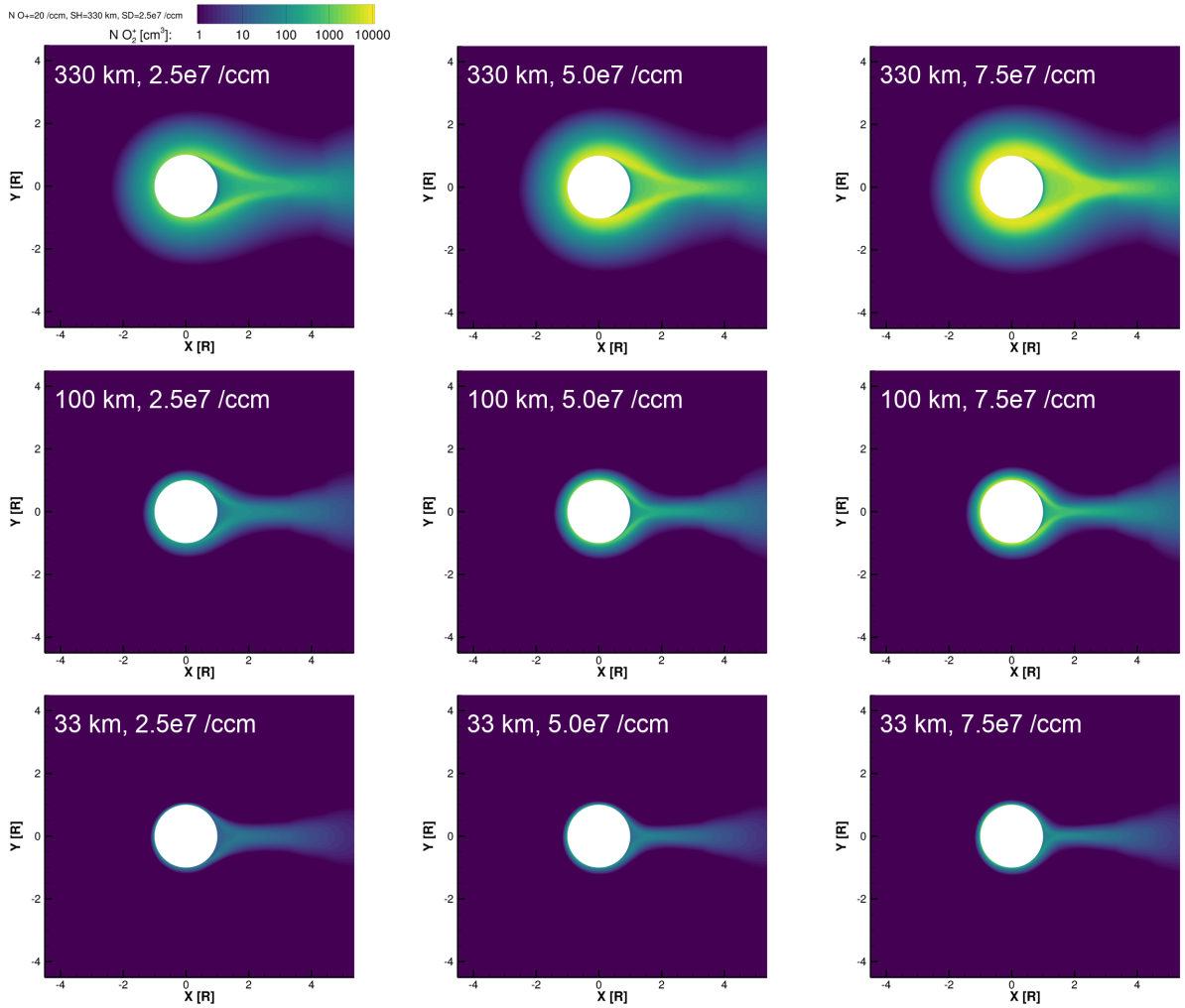

Figure 5.2: Density of O_2^+ in the equatorial plane for the simulations with low ambient plasma density.

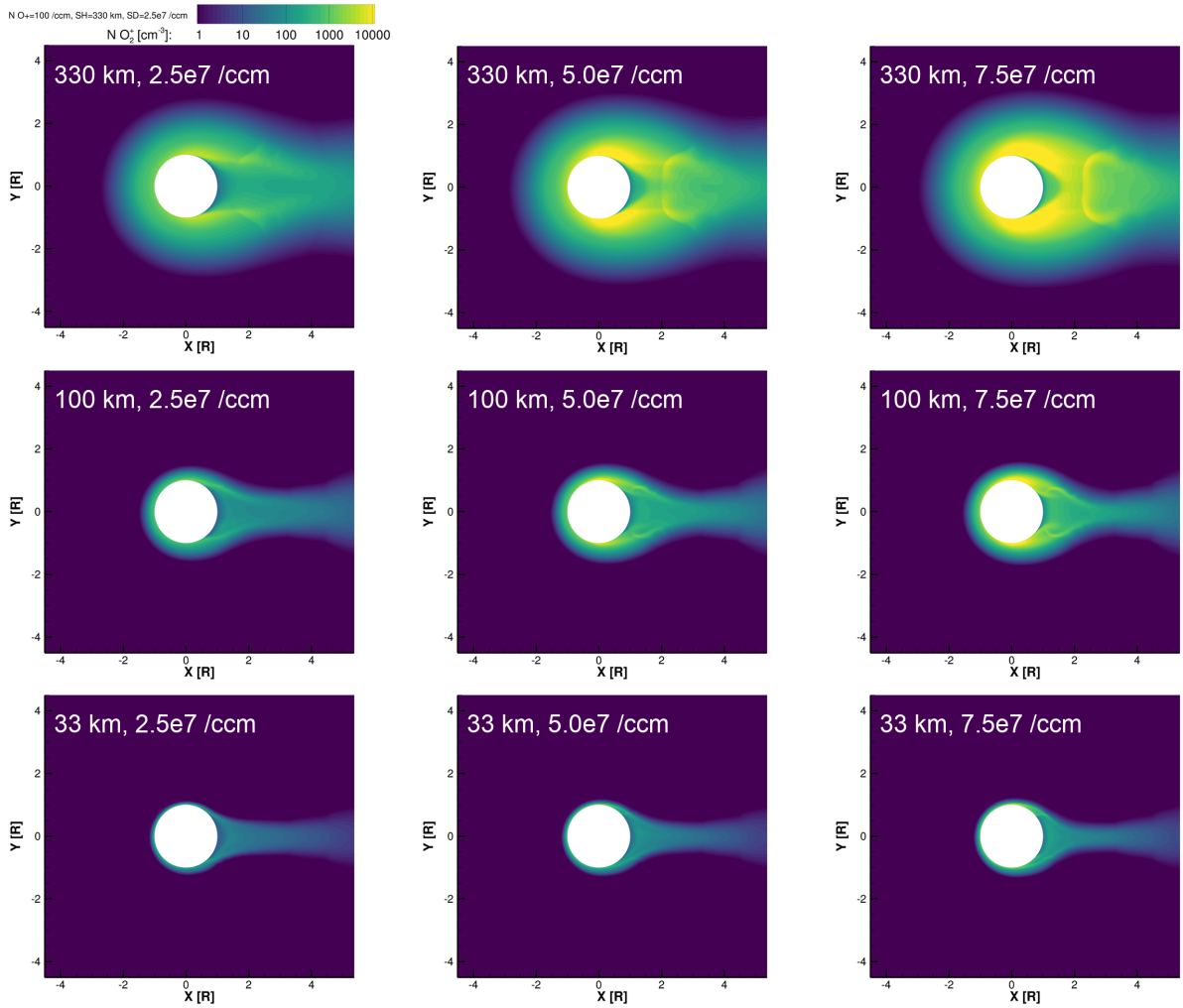

Figure 5.3: Density of O_2^+ in the equatorial plane for the simulations with high ambient plasma density.

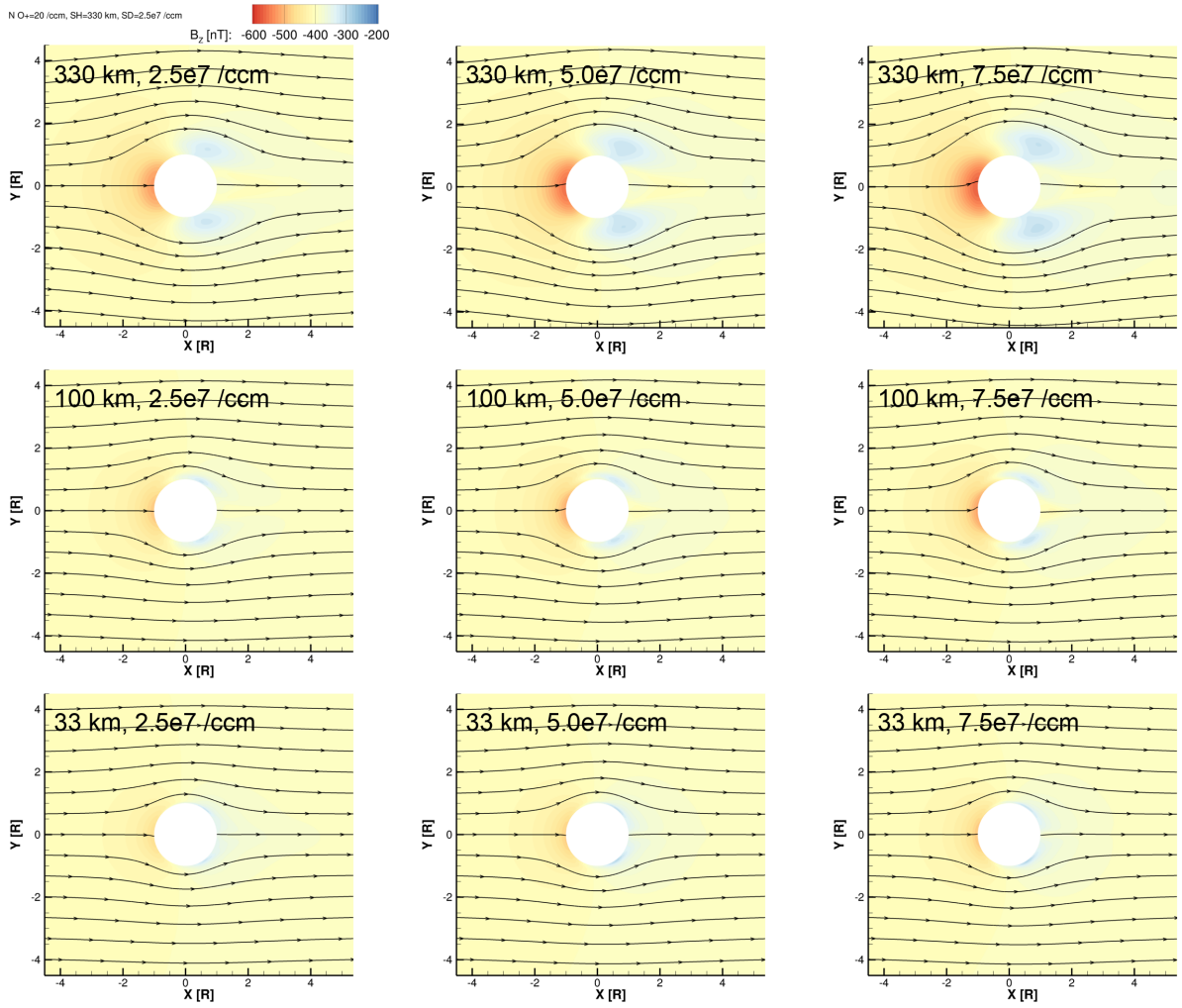

Figure 5.4: Color contours show the magnetic field in the equatorial plane for the simulations with low ambient plasma density. Streamlines indicate the direction of the charge-averaged velocity U_q in the XY plane.

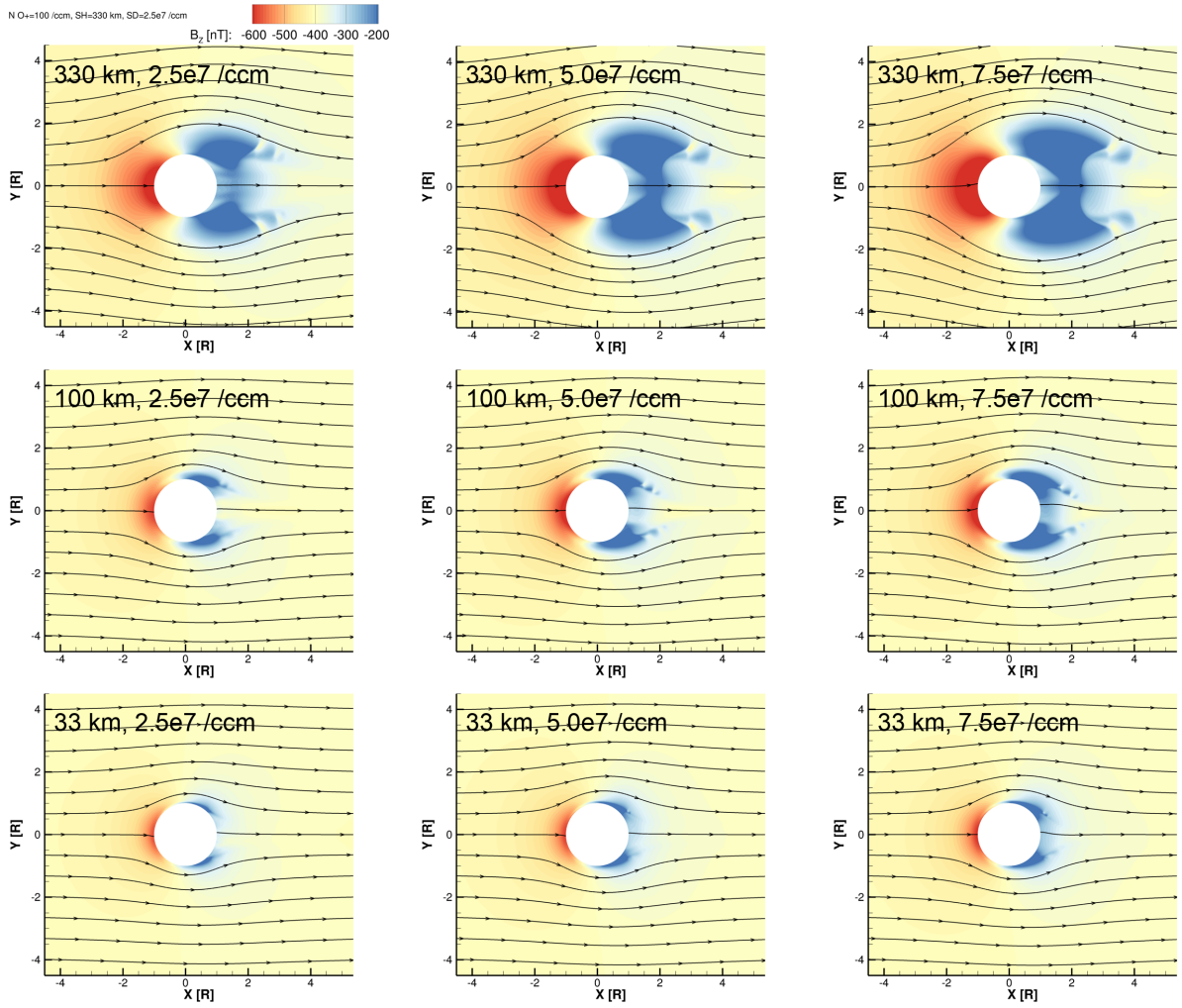

Figure 5.5: Color contours show the magnetic field in the equatorial plane for the simulations with high ambient plasma density. Streamlines indicate the direction of the charge-averaged velocity U_q in the XY plane.

In both **Figure 5.4** and **Figure 5.5** we observe that on the downstream side of the interaction, where the magnetic field is relatively depressed (blue), there are two local minima of the B_Z magnetic field, one on the sub-jovian (+Y) side and one on the anti-jovian (-Y) side. By comparing **Figure 5.2** with **Figure 5.4**, and **Figure 5.3** with **Figure 5.5,** we observe that the size and strength of the regions of depressed magnetic field correspond with the locations where the ionosphere density is highest in each simulation. These features occur due to increases in pressure in the ionospheric ion fluids, shown in **Figure 5.6c** for O_2^+. Two factors act to increase

the pressure on Europa's flanks. Close to Europa's surface the plasma pressure increases as the ionosphere density increases due to ionization (see Term 9 in **Equation 2.12**). Farther from the surface, the pressure increases as ionospheric plasma is transported downstream at increased speeds (**Equation 2.3**, **Figure 5.6b**), as discussed in **Section 3.2**. To maintain the balance between the plasma pressure ρu^2 and the magnetic pressure $B^2/2\mu_0$, the magnetic field strength decreases where the pressure increases due to these effects.

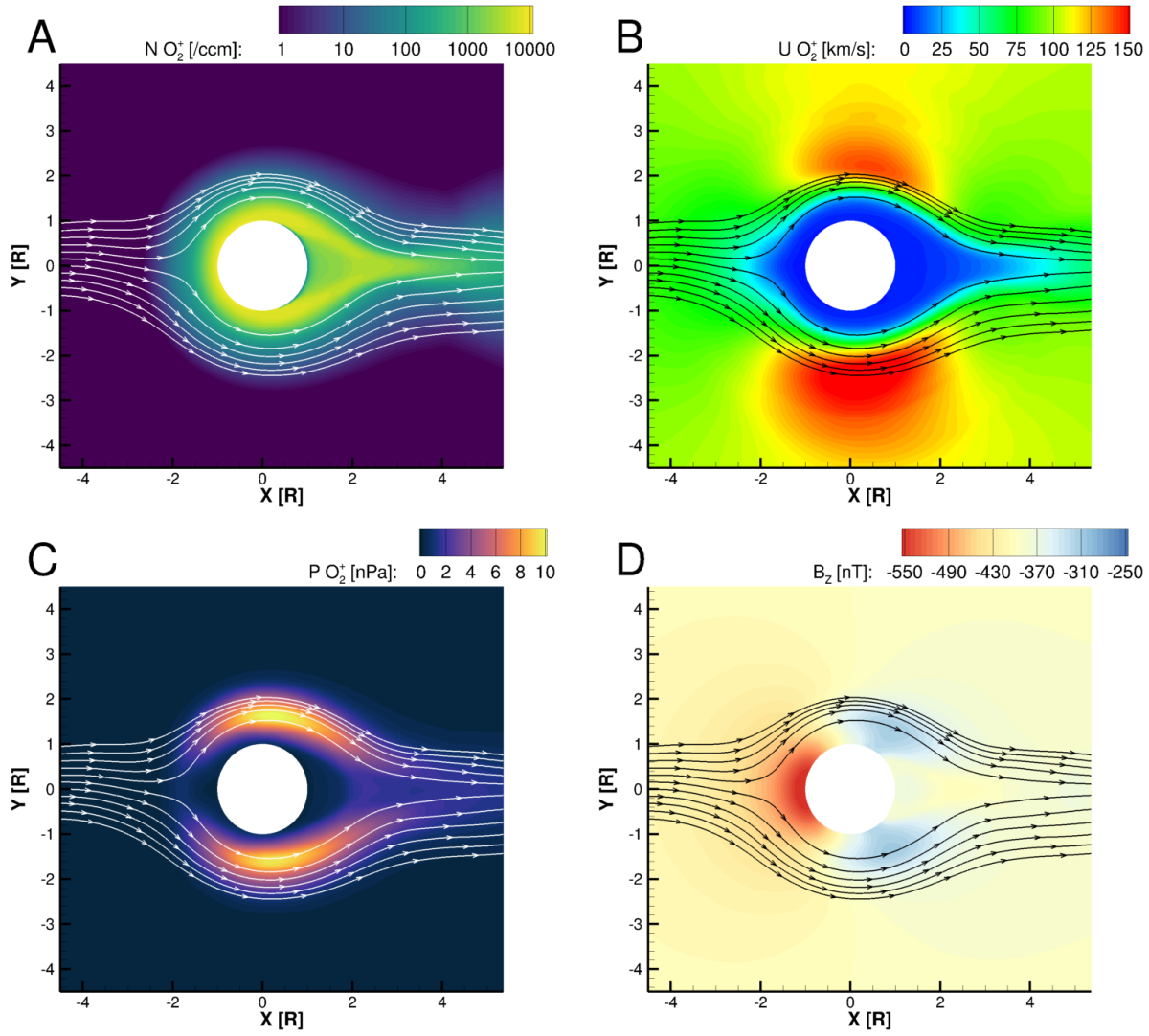

Figure 5.6: Bulk plasma properties of O_2^+ and B_Z in the equatorial plane for the low ambient plasma density, high atmosphere surface density, high atmosphere scale height simulation (top right panel in **Figure 5.2** and **Figure 5.4**). Panels A, B, and C show respectively the number density, speed, and pressure of the O_2^+ MHD fluid, while Panel D shows B_Z. Streamlines in all four panels indicate the velocity of O_2^+ in the equatorial plane.

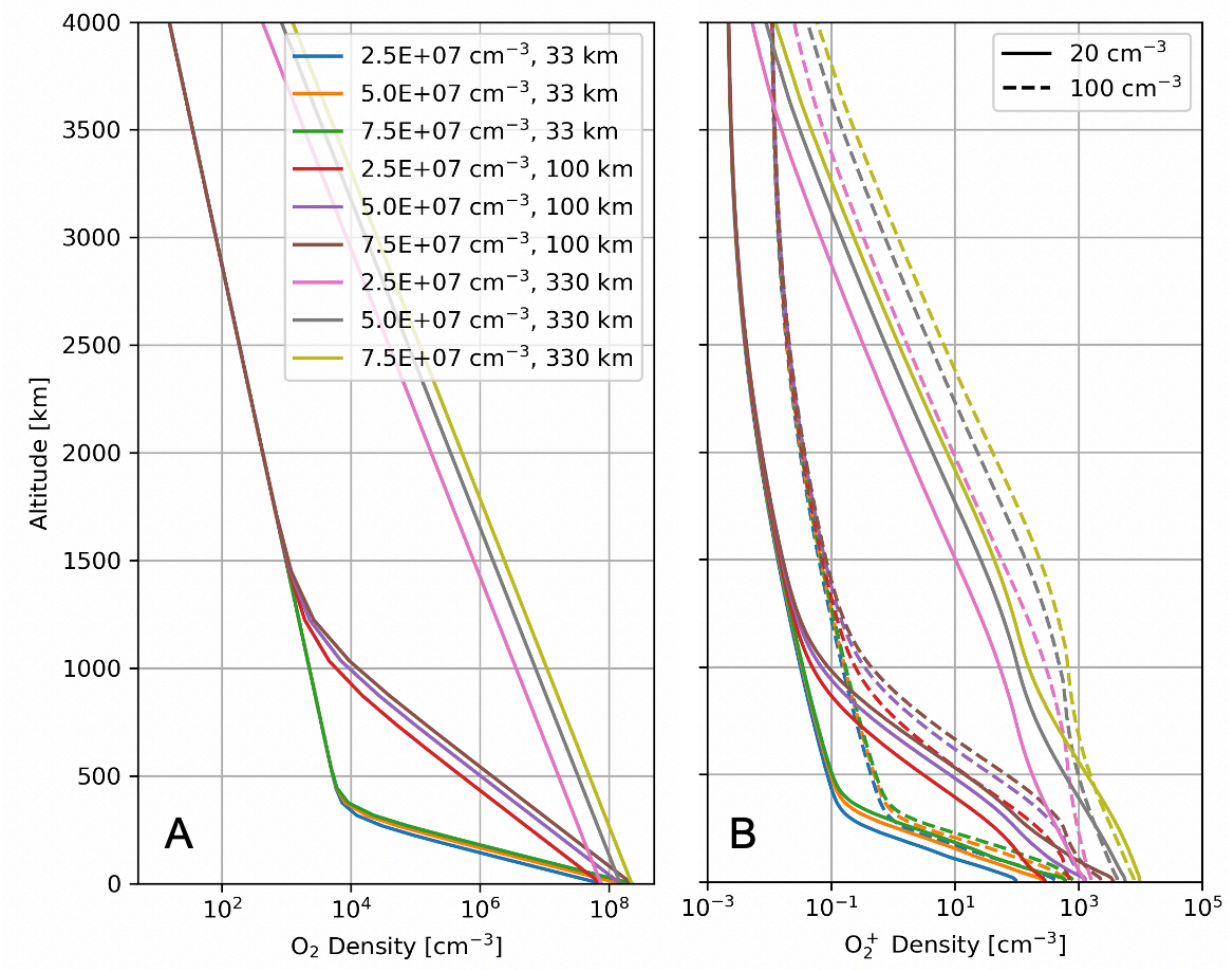

Figure 5.7: Comparison of atmosphere and ionosphere density profiles in the upstream direction, along the negative X axis. Panel A shows the O_2 density for each atmosphere in the study. Panel B shows the corresponding density of O_2^+. In Panel B solid lines give the density from the simulations with low ambient plasma density, while the dashed lines correspond to simulations with high ambient plasma density.

To better compare the densities of plasma between simulations, in **Figure 5.7** we show altitude profiles of the density of the atmospheres and ionospheres for every simulation in the study. In **Figure 5.7a** we see the prescribed density of the atmospheres in the upstream direction. The density decreases monotonically with distance from the surface. After several atmosphere scale heights, the rate of decrease in density drops as the primary population of the atmosphere becomes less significant than the secondary, low density population. For the highest scale height

simulations, this change in slope occurs at higher altitudes than shown in the figure. In **Figure 5.7b** we show the corresponding density of the ionosphere in each simulation. Near Europa's surface the density of O_2^+ is primarily controlled by the ion production rate, which is proportional to the density of the atmosphere. Therefore the rate at which the density of O_2^+ decreases changes at the same altitudes where the changes occurred in the atmosphere, at about 400 km for the 33 km scale heights, about 1250 km for the 100 km scale heights, and at farther distances for the 330 km scale heights.

Figure 5.7b also illustrates that the density of the ionosphere is generally increased with higher ambient plasma density (dashed lines), consistent with our findings from **Chapter 3** (see **Figure 3.6**). However, there are four atmosphere cases where the ionosphere density at low altitudes for the low ambient plasma density simulation slightly exceeds that for the high ambient plasma density simulation. This occurs for the four atmospheres with medium or high scale height (330 km or 100 km) and medium or high surface density (5.0×10^7 cm^{-3} or 7.5×10^7 cm^{-3}).

In **Figure 5.8** we examine the electron density and focus on the region within 400 km of Europa's surface. For each simulation we show the electron density along the upstream direction as well as on the sub- and anti-Jovian flanks. **Figure 5.8a** shows the electron density for the simulations with low ambient plasma density. In these cases, the electron density is generally consistent with the densities derived from the *Galileo* radio occultation experiment shown in **Figure 5.9** (McGrath et al., 2009, Figure 7). These electron density profiles were observed at a variety of locations over Europa's surface, just as we sample different locations for the profiles shown in **Figure 5.8**. **Figure 5.8b** shows the electron density for the simulations with high ambient plasma density. While the highest density ionospheres are significantly denser than the *Galileo* electron densities (which do not exceed 15000 cm^{-3}), most of the high ambient plasma

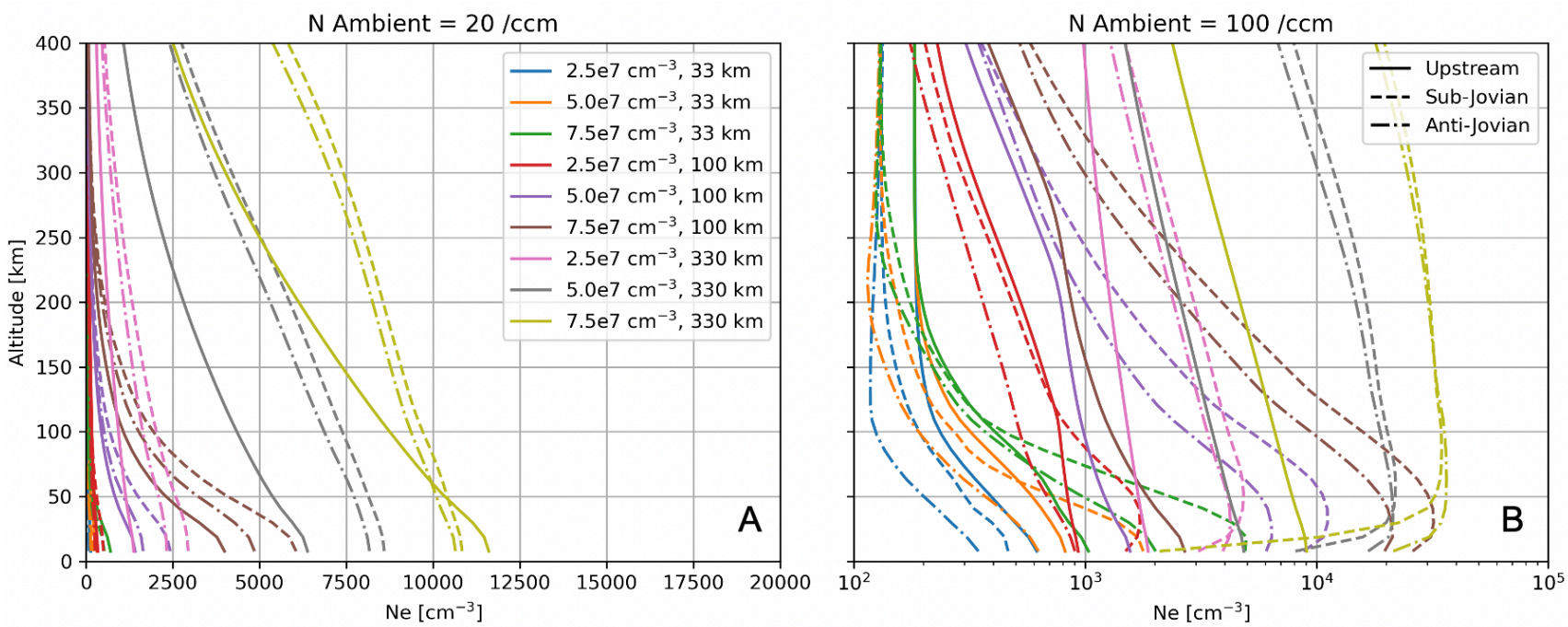

Figure 5.8: Electron density profiles at low altitudes. In both panels solid lines denote the electron density along the upstream/-X axis, dashed lines correspond to the sub-jovian/+Y axis, and dash-dot lines correspond to the anti-jovian/-Y axis. Panel A gives the electron density for the simulations with low ambient plasma density, while Panel B shows the simulations with high ambient plasma density. Note that the X axes differ between Panel A and Panel B. For Panel A the range was chosen for easy comparison with the *Galileo* radio occultation measurements shown in McGrath et al. (2009), Figure 7. For Panel B the range was increased and scaled logarithmically to show the full variability of the electron density.

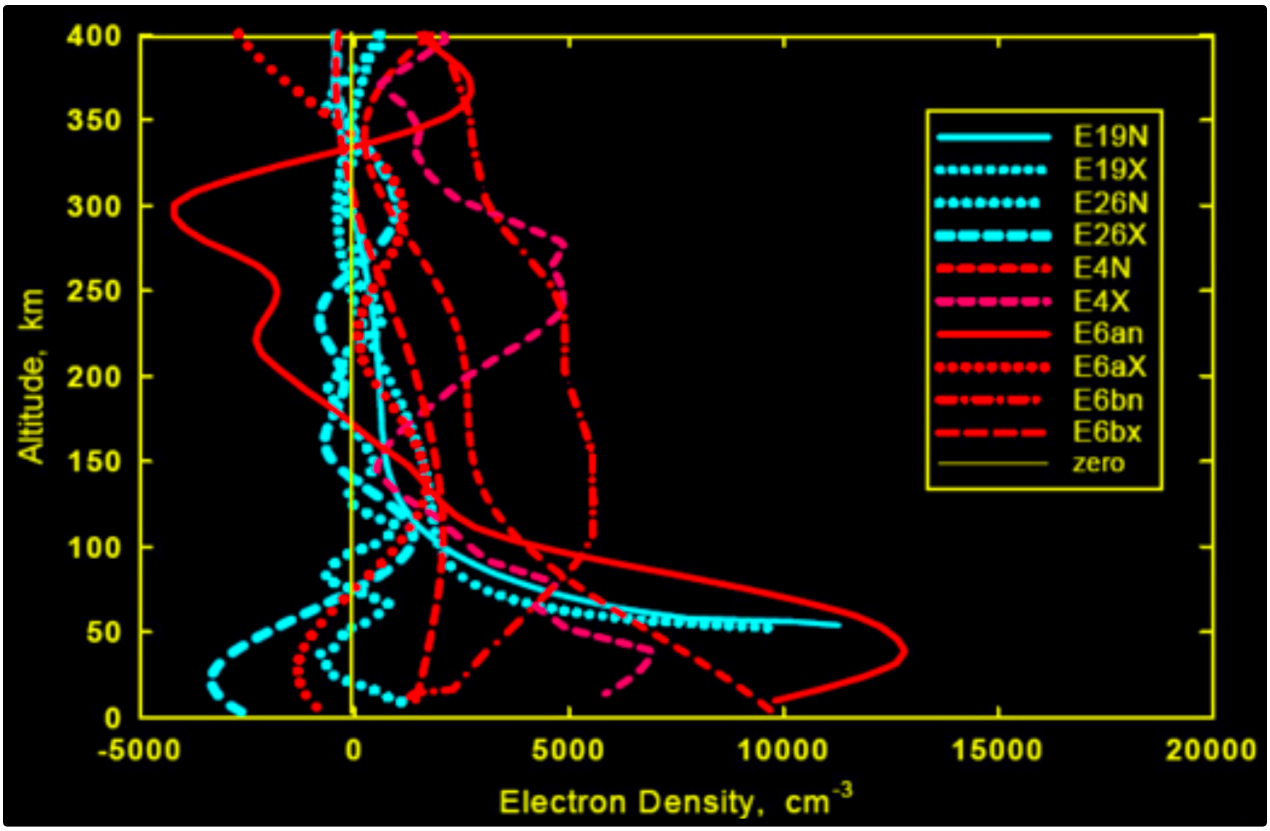

Figure 5.9: Electron density profiles measured by *Galileo* radio occultations, reproduced from McGrath et al. (2009), Figure 7.

density simulations still produced ionospheres similar to the *Galileo* profiles. Thus we find that reasonable variations in Europa's atmosphere can cause the electron density to vary by multiple orders of magnitude at the same altitudes, in agreement with the observations.

Figure 5.8 demonstrates the significant variability of Europa's ionosphere not only with variation of the atmosphere, but in different locations within the plasma interaction. In both plots different line styles indicate data extracted along the upstream/-X axis (solid), sub-Jovian/+Y axis (dash-dash), and anti-Jovian/-Y axis (dash-dot). **Figure 5.8a** shows that in the simulations with low ambient plasma density the electron density is generally higher on the sub-Jovian side (dash-dash) of the plasma interaction than the anti-Jovian (dash-dot). This asymmetry is associated with the multi-fluid properties of the plasma interaction as discussed in **Section 3.2**.

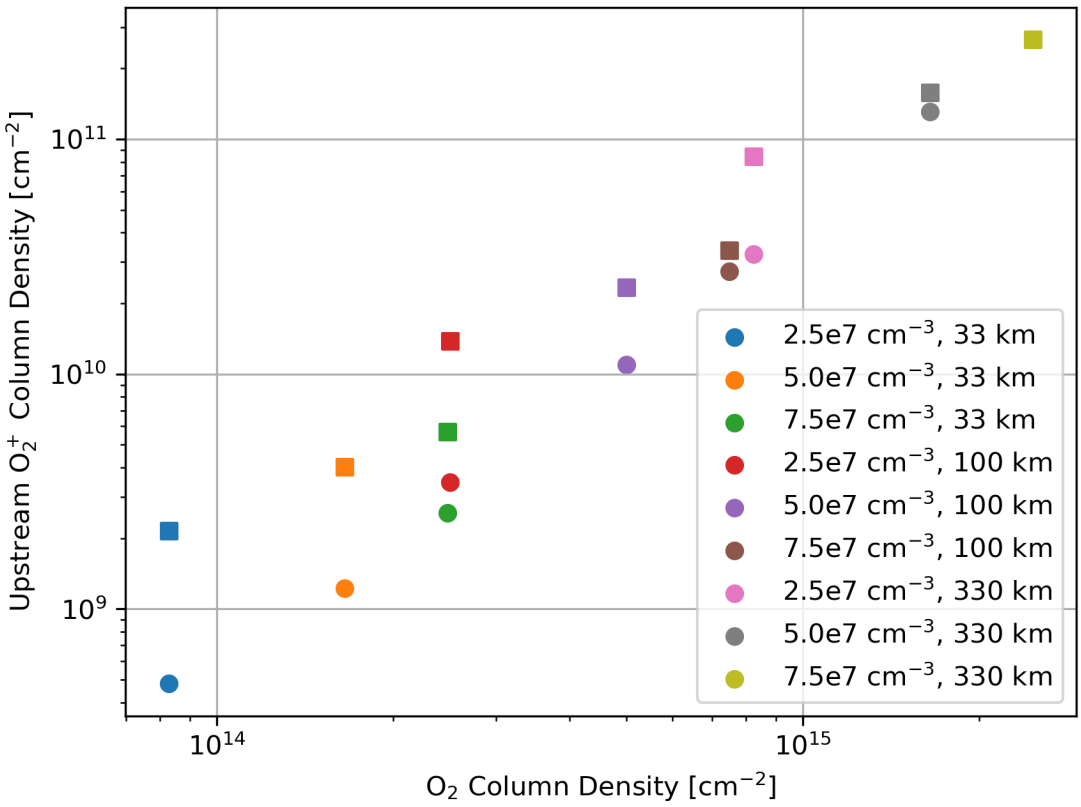

Figure 5.10: Column density of O_2^+ integrated along the upstream/-X axis. Circle markers indicate simulations with low ambient plasma density, while squares indicate high ambient plasma density. Note that the markers for the simulations with the highest column density atmosphere overlap each other.

Figure 5.10 compares the column density of Europa's ionosphere with the column density of the atmosphere, essentially integrating the curves shown in **Figure 5.7b**. The column density of the ionosphere increases with the column density of the atmosphere in a ratio of $1{:}10^4$. In other words, to increase the column density of the ionosphere by a certain amount requires that the column density of the atmosphere increase by 10,000 times that amount. In **Chapter 3** the upstream column density of O_2^+ ranged from 2.5×10^9-3.4×10^{10} cm^{-2} (see **Figure 3.6**). Here the column density ranges from 4.8×10^8-2.7×10^{11} cm^{-2} for the simulations with low ambient

plasma density and 2.2×10^{9}-2.7×10^{11} cm^{-2} for the simulations with high ambient plasma density. In this study we therefore observe a larger range of variation in the ionosphere column density that encompasses the regime explored in **Chapter 3**.

5.3 Precipitation of thermal plasma

We have described the general trends in variation of the ionospheric structure and resultant magnetic field perturbations illustrated by the results of this parameter study. As described in **Chapter 3**, these properties of the plasma interaction control the intensity and spatial patterns of the precipitation of thermal plasma onto Europa's surface. This precipitation in turn contributes to the sputtering process that generates Europa's atmosphere. The study presented in **Chapter 3** focused on the effect of the upstream plasma conditions on plasma precipitation. To develop a better understanding of the coupling between the plasma environment and Europa's atmosphere, we now analyze the simulations of this study in a similar manner as we did for **Chapter 3** to characterize the effects of Europa's atmosphere on the precipitation of thermal plasma.

Figure 5.11 and **Figure 5.12** show maps of the downward flux of ambient magnetospheric plasma from each simulation of the study. The two figures differ in that the intensity of the precipitating flux is uniformly increased in the simulations with high ambient plasma density (**Figure 5.11**). Within each figure, trends in temperature and precipitation patterns emerge with the varying surface density and scale height of the atmosphere. For atmospheres with smaller scale heights, or lower surface densities, more magnetospheric plasma with temperatures higher than 100 eV precipitates, as indicated by the orange contours in each panel of the two figures. As was observed in **Figure 3.8**, on the leading hemisphere (0˚-180˚ W. Lon.) in all simulations we observe a patch of no precipitation near the equator, and low

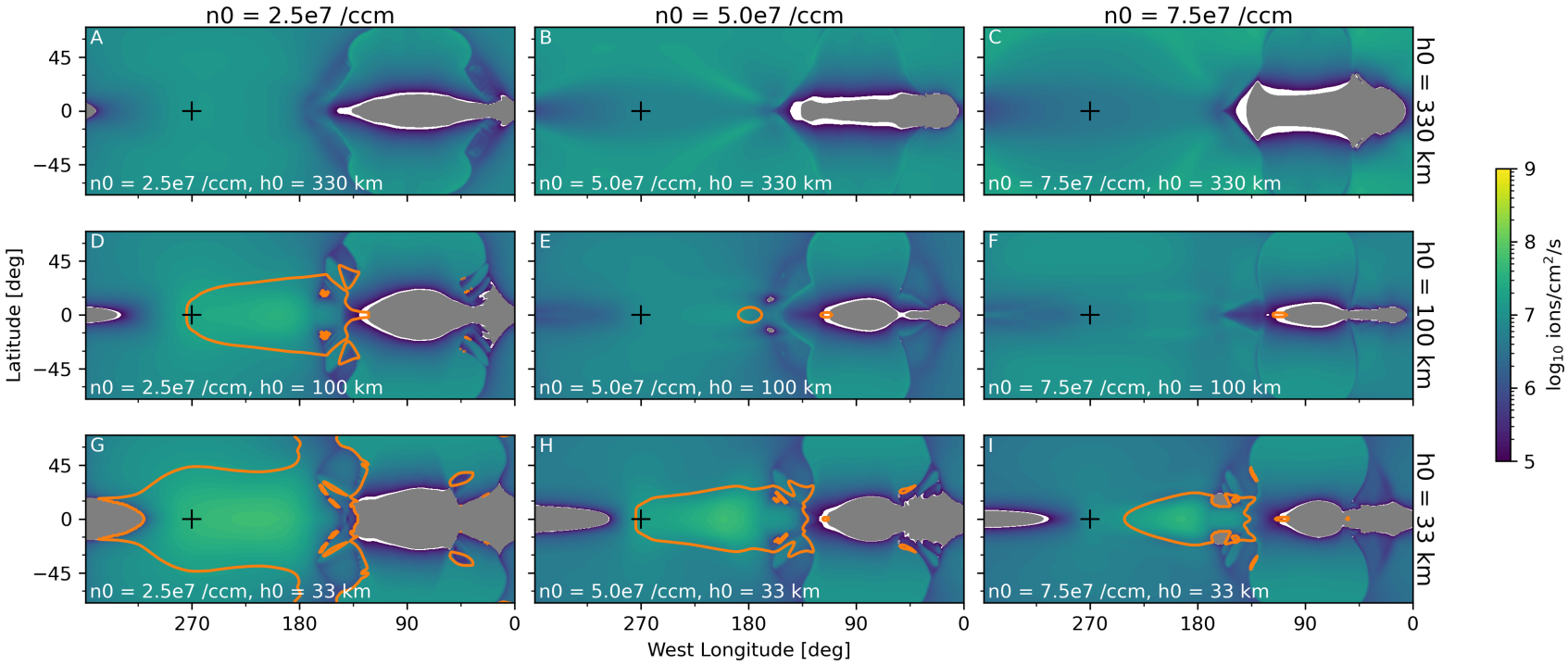

Figure 5.11: Maps of downward flux of the ambient plasma fluid in each of the simulations with low upstream plasma density. Grey regions block out locations where the net flux of plasma is outward. Black pluses mark the ram direction, or the apex of the trailing hemisphere, at 0˚ latitude and 270˚ West longitude. Orange contours describe regions where the temperature of the precipitating plasma exceeds 100 eV.

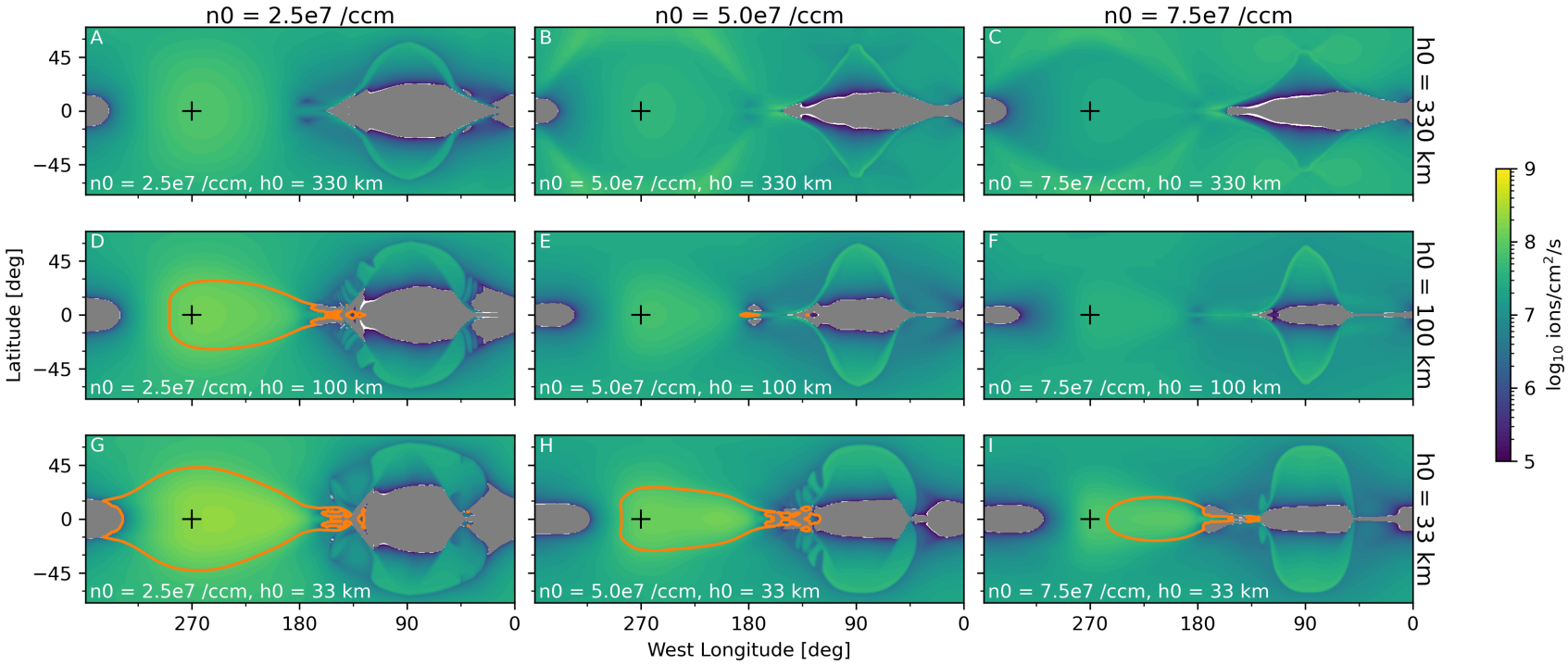

Figure 5.12: Maps of downward flux of the ambient plasma fluid in each of the simulations with high upstream plasma density. Annotations are as described for **Figure 5.11**.

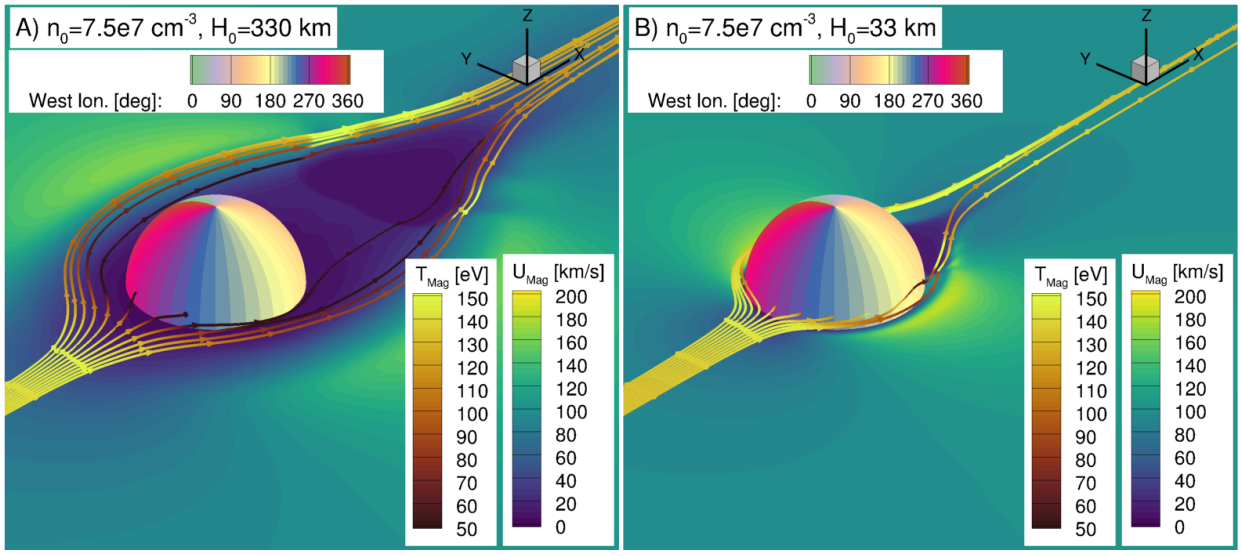

Figure 5.13: 3D streamtraces of the ambient magnetospheric fluid in the simulations with high ambient plasma density, high atmosphere surface density, and either high (A) or low (B) atmosphere scale height. This view shows streamtraces that were seeded upstream and run from left to right, with some terminating on Europa's trailing hemisphere and others continuing downstream. Color contours show the speed of the magnetospheric plasma in the Z=0 plane. The streamlines are colored according to the temperature of the magnetospheric plasma. The simulation shown in Panel A corresponds to **Figure 5.11c**, while Panel B corresponds to **Figure 5.11i**.

precipitation at middle and high latitudes. However, in contrast to **Figure 3.8**, for many simulations the maximum intensity of precipitating plasma does not occur near the apex of the trailing hemisphere (indicated by black plus symbols). In particular, in **Figure 5.11c** on the trailing hemisphere (180˚ – 360˚ W. Lon.) we observe a lens-like pattern of decreased flux around the apex of the hemisphere and higher flux in a rim around the edge of the hemisphere. This is in contrast to, for example, **Figure 5.11i**, which exhibits a clear bulls-eye pattern of high flux peaking near the apex of the trailing hemisphere, as did all the simulations shown in **Figure 3.8**.

Figure 5.13 examines this feature by comparing the simulations shown in **Figure 5.11c** and **Figure 5.11i**. **Figure 5.13** shows the temperature of the magnetospheric plasma along streamlines as they approach Europa. Here the temperature is calculated as $T = p/nk_B$. We

observe that in **Figure 5.13a** as plasma approaches Europa the speed and temperature of the plasma decreases and streamlines are strongly diverted in the +Y and -Y directions. In **Figure 5.13b**, where the scale height of the atmosphere is much smaller, the temperature of the impinging plasma is much less decreased as it interacts with the ionosphere over a shorter distance. Since the temperature of the magnetospheric plasma is higher, the ionosphere presents a less significant obstacle to the impinging magnetospheric plasma, and plasma is therefore less strongly diverted.

In **Figure 5.13b** we also observe that the diversion of plasma is asymmetric such that streamlines are more strongly excluded from Europa's surface on the sub-Jovian side of the moon, whereas streamlines are able to precipitate on the anti-Jovian side. This corresponds to the patches near the equator in **Figure 5.11i** where no plasma precipitates on the sub-Jovian side (~315˚-360˚) and where relatively warm plasma precipitates on the anti-Jovian side (~180˚-270˚). This occurs because the ionosphere tends to be denser on the sub-Jovian side than on the anti-Jovian side (**Figure 5.8**). The cause of this asymmetry is the Lorenz force acting on the ionospheric plasma, and was previously discussed in **Section 3.2**.

Figure 5.14 shows the fraction of streamtraces originating from the upstream that were diverted away from Europa's surface in each simulation. As described in **Section 3.2**, we seeded streamtraces of the ambient plasma velocity upstream of Europa, then measured the fraction of streamtraces that were diverted away from Europa's surface. Whereas in **Chapter 3** we found that ~ 88% of streamtraces were diverted, with a variation of just ±2% across the whole study, here we find much more variation. Across this study the diversion ranged from 78% - 97%. As in **Chapter 3**, we found that the ambient plasma density made little difference in varying the fraction of diverted streamtraces (less than 5% change). The most pronounced change in

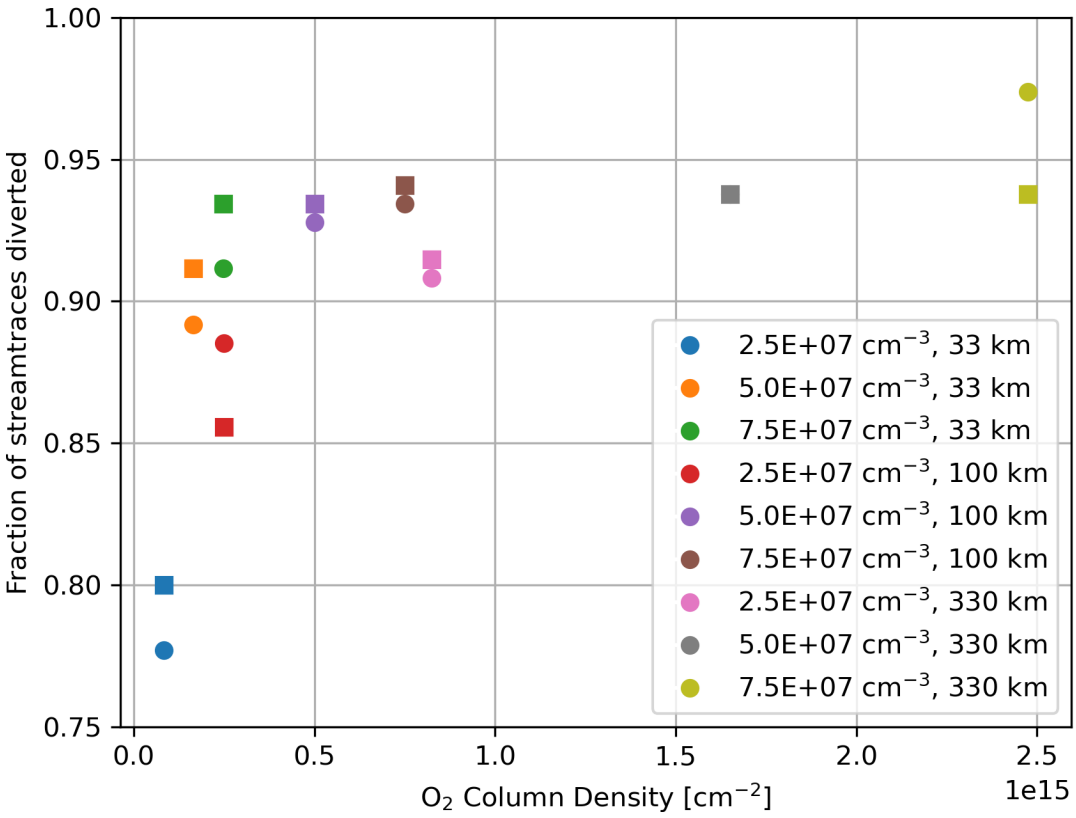

Figure 5.14: Fraction of streamtraces diverted in each simulation. Annotations are as described for **Figure 5.10**.

diversion is caused by increasing the surface density of the atmosphere; considering just the simulations with low ambient plasma density and 33 km scale height atmospheres, we find that the fraction of diverted streamtraces increases from 78% (surface density=2.5×10^{7} cm^{-3}) to 89% (surface density=5.0×10^{7} cm^{-3}) to 91% (surface density=2.5×10^{7} cm^{-3}).

This result is in qualitative agreement with the results of Saur et al. (1998), who developed a fluid model for Europa's plasma interaction to study the coupling between the plasma and the neutral atmosphere. The authors varied the surface density of the atmosphere, and therefore the column density of the atmosphere, and assessed the resulting system for mass balance between the different sources and losses in the model. Figure 3 of Saur et al. (1998) shows that they found that as the column density increased from 0.1-1.5$\times10^{15}$ cm^{-2} the effective

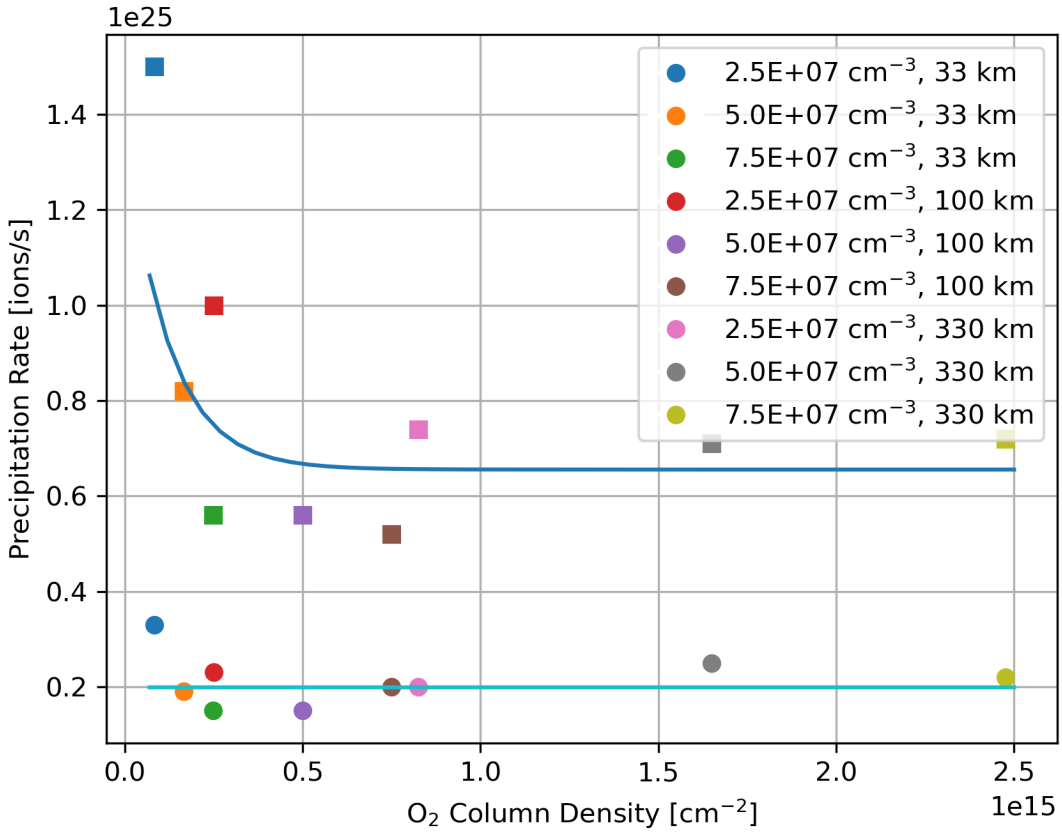

Figure 5.15: Integrated downward flux of thermal ambient plasma for each simulation. Annotations are as described for **Figure 5.10**. Trend lines have been fit to the data; the method and fit parameters are discussed in the text.

radius of Europa as an obstacle to the plasma flow decreased significantly. Our findings are consistent with this result, as shown by **Figure 5.14**, which shows a sharp increase in the amount of streamtraces diverted away from Europa's surface through the same parameter space in atmospheric column density.

As in **Chapter 3**, we integrated the downward number flux of the ambient plasma over Europa's surface to calculate the precipitation rate for each simulation, shown in **Figure 5.15**. In **Chapter 3** the rate ranged from (5.6-26)×10^{24} ions/s, while in this study the rate ranges from (1.5-3.3)×10^{24} ions/s for the simulations with low ambient plasma density and (5.2-

15)×10^{24} ions/s for the simulations with high ambient plasma density. In **Chapter 3** we showed that the precipitation rate increased linearly with the density of the ambient plasma (**Figure 3.10**). Consistent with that result, we find that for all atmosphere cases the precipitation rate increases with the ambient plasma density. However, we also identify that, particularly in the high ambient plasma density cases, the precipitation rate drops quickly as the atmosphere column density increases to 0.5×10^{15} cm^{-2}, and at higher column densities is approximately constant.

To aid in the application of these results, we have fit functional forms to the precipitation rate of ambient, thermal magnetospheric plasma to Europa's surface as a function of atmosphere column density for these two cases. In calculating the fits, we did not include the simulations with the lowest and the highest atmosphere column density in each case, since these simulations may not represent realistic cases for Europa's atmosphere (note that, as shown in **Figure 5.1,** the atmospheres with the highest and lowest column density lie outside the column density range established by Hall et al., 1995 and 1998). We found that the simulations with low ambient plasma density (20 cm^{-3}) were well fit by a constant precipitation rate of 1.96×10^{24} ions/s. However, the simulations with high ambient plasma density (100 cm^{-3}) were better fit by an exponential curve of the form $P = 7.1 \times 10^{24} \cdot \exp(-1 \cdot C \cdot 7.47 \times 10^{-15}) + 6.4 \times 10^{24}$, where P gives the precipitation rate of thermal magnetospheric plasma in ions/s and C is the O_2 column density of the atmosphere in cm^{-2}.

5.4 Conclusions

To better understand how variations in Europa's atmosphere affect the bulk plasma properties and magnetic fields of Europa's plasma interaction, we conducted a parameter study that explores a reasonable parameter space for the atmosphere. Our design for the study was informed by the current best constraints on the atmosphere provided by analysis of HST

observations (Hall et al., 1995 and 1998; Roth et al., 2016) as well as predictions based on various models for the atmosphere (e.g. Cassidy et al., 2007 and 2013; Teolis et al., 2017a; and other references in Plainaki et al., 2018).

In this study we observed a larger variation in ionosphere density as compared to the variation observed in the study conducted for **Chapter 3**. As each study explored the full range of variation in the respective parameters under investigation, this indicates that variation in Europa's neutral atmosphere could potentially have stronger effects on the density of Europa's ionosphere than variation of magnetospheric conditions. However, we note that the variation of magnetospheric conditions explored in **Chapter 3** is relatively better understood. In particular, the magnetospheric magnetic field and plasma properties are known to vary periodically as Jupiter's dense plasma sheet wobbles up and down over Europa. The effects of this variation on the magnetic fields of the plasma interaction were observed in the *Galileo* datasets. While mechanisms that cause variation in Europa's atmosphere have been proposed through investigation with atmospheric models and based on observations from the HST, the current limitations on observations of Europa's atmosphere prevent detailed measurement of potential time variation in the atmosphere. Therefore, while our study shows that variations in the atmosphere could potentially have a stronger effect on Europa's ionosphere than variations in magnetospheric parameters, it is not known whether these variations occur to the degree modeled here with regularity. Nevertheless, the qualitative similarities between the modeled and measured electron density profiles indicate that this is possible (compare **Figure 5.8** and **Figure 5.9**).

In general, we found that as the column density of the atmosphere increased, the column density of the ionosphere increased as well. The implications for the precipitation of thermal plasma onto Europa's surface were that simulations with atmospheres with higher column

densities, either due to increased scale height or increased surface density, saw less precipitation of thermal plasma. As the atmosphere column density increased from ~10^{14} cm^{-2} to 5×10^{14} cm^{-2} the total amount of precipitating thermal plasma decreased sharply; at higher column densities the precipitation rate appears to saturate at 2×10^{24} ions/s for the simulations with low ambient plasma density and 6.4×10^{24} ions/s for simulations with higher ambient plasma density. This behavior is controlled principally by the diversion of impinging plasma to the flanks of the plasma interaction by Europa's ionosphere. The leveling-off of the precipitation rate with increasing column density contrasts with the effect observed in **Chapter 3**, where the thermal plasma precipitation rate increased approximately linearly with the ambient plasma density.

We also observed that the temperature of the precipitating plasma decreased significantly with increasing atmosphere column density. The temperature of the precipitating plasma generally decreased with the surface density of the atmosphere, and the simulations with the highest scale heights saw no plasma precipitate with temperatures higher than 100 eV. This indicates that sputtering by thermal ions should be less significant when the atmosphere density is high.

In designing the input parameters for the simulations, we made two simplifying assumptions for the magnetic fields: we aligned the background magnetic field with the Z axis, and we did not include Europa's induced field. Doing so permitted us to focus on the interaction between the atmosphere and the plasma fluids without the obfuscation of additional asymmetries caused by the B_X and B_Y components of the background magnetic field. We expect that the main effect of including these components would be to tilt the interaction and cause the precipitation of plasma to be displaced elsewhere on Europa's surface, but should not affect the total precipitation rate in any significant way. More significant effects could be caused by the

inclusion of the induced field, which is variable in strength and direction depending on the background Jovian field, and could contribute to shielding parts of the surface from direct precipitation (as was observed for energetic particles by Nordheim et al., 2021).

Chapter 6 Summary and Outlook

Europa, one of the many moons of Jupiter, is coupled to the magnetosphere of its parent planet by the interaction of Jupiter's magnetospheric plasma and magnetic field with Europa's atmosphere, ionosphere, surface, and subsurface ocean. Over the past several decades it has fascinated planetary scientists and stimulated a proliferation of research on the so-called Ocean Worlds and moon-magnetosphere interactions of our solar system. However, there are still gaps in our understanding of this complex system. This dissertation undertook to fill many of these gaps through the development of a multi-fluid MHD model for the plasma interaction. We then applied the model to study the plasma interaction's variability in response to changing external and internal conditions. Understanding Europa's space environment as a unified, coupled system will be critical to the success of NASA's *Europa Clipper* mission in the coming decades.

In the following sections, we summarize the conclusions of this research and the implications derived from it. In **Section 6.1** we review the conclusions reached in **Chapter 2-5**. In **Section 6.2** we outline the connections between this research and the goals of the *Europa Clipper* mission, and we finish by sketching the unified system of Europa's space environment, which this dissertation partially illuminates.

6.1 Summary

In **Chapter 2** we discussed the development of a new multi-fluid magnetohydrodynamic model for Europa's plasma interaction. The development of this model was motivated by the need to understand the role of Jupiter's magnetospheric plasma in the plasma interaction between Europa and Jupiter's magnetosphere. To that end, a model was developed that built on the work

of Rubin et al. (2015) using the BATS-R-US MHD framework (Toth et al., 2012). The model solves steady state solutions for the multi-fluid MHD equations corresponding to three ion fluids: magnetospheric ions, ionospheric O_2^+, and ionospheric O^+. The model self-consistently develops solutions for the bulk parameters of these fluids as well as the magnetic field resulting from the plasma interaction. Europa's atmosphere is prescribed in the model, and is coupled to the plasma through source and loss terms that represent the effects of ionization, recombination, and charge exchange on the mass, momentum, and pressure of the MHD fluids. Two simulations of the *Galileo* E4 and E14 flybys were conducted to validate the model and assess the model's performance. The good agreement between the simulated magnetic fields and plasma conditions and the *Galileo* data indicates that the model accurately represents the plasma interaction under a variety of conditions. We therefore proceeded to apply the model to address various questions about the variability of Europa's plasma interaction in response to the external and internal conditions.

In **Chapter 3** we investigated the variability of Europa's plasma interaction in response to the changing conditions of Jupiter's magnetosphere. We explored a parameter space that represents the range of different magnetic field and plasma conditions Europa experiences during Jupiter's 11-hour synodic rotation, and considered three different cases for the global state of the magnetosphere. We selected nine different sets of parameters with which we conducted steady state simulations that comprised the parameter study. One aspect of the plasma interaction that we chose to focus on was the precipitation of thermal plasma from Jupiter's magnetosphere onto Europa's surface. The precipitation of these thermal ions onto Europa's icy surface causes sputtering to occur, by which neutral particles are released into Europa's atmosphere. This process is therefore important for understanding the coupling between Europa's plasma

interaction, surface, and atmosphere. By examining maps of the downward flux of magnetospheric plasma onto Europa's surface for each simulation, we have quantified the access of Jupiter's magnetospheric plasma onto Europa's surface and its variability in response to the changing conditions in the ambient environment. In all simulated precipitation maps, pronounced asymmetries develop between the upstream and downstream hemispheres as a result of the interaction between the incident Jovian flow and Europa's ionosphere. One notable result from the MHD model was that magnetospheric plasma can gain significant access to Europa's leading, or downstream, hemisphere at mid and high latitudes. Previously, analytic models for plasma precipitation only considered access of magnetospheric plasma to the trailing hemisphere. We analyzed the simulation results and determined that the total precipitation rate of magnetospheric plasma onto Europa's surface increases linearly from 5.6–26 $\times 10^{24}$ ions/s with the density of the ambient magnetospheric plasma, establishing a reference for how precipitation changes with Europa's magnetic latitude in Jupiter's magnetosphere.

In **Chapter 4** we turned our attention to the *Galileo* E15 flyby. Due to the configuration of Europa with respect to Jupiter and the Sun during this flyby, we identified it as a good candidate for investigating the effects of changes in Europa's atmosphere on the plasma interaction. Europa's atmosphere was likely altered during this flyby due to the effects of solar illumination on the sputtering process that generates the atmosphere. We reviewed the analysis of Volwerk et al. (2001) and incorporated the predictions of the Plainaki et al. (2013) model for Europa's atmosphere under changing solar illumination. We have developed several different atmosphere models taking into account the solar illumination effects and incorporated them into our multi-fluid model to investigate how the global plasma interaction varies as a result of changes to the atmospheric configuration. While none of the simulations can explain all of the

main features in the *Galileo* magnetic field and plasma data, the simulation results collectively did suggest that some sort of atmosphere enhancement on the moon's leading hemisphere is needed to explain the magnetic field configuration and plasma density enhancement observed in the wake region. Such an atmosphere enhancement could arise from enhanced sputtering yield on the sunlit hemisphere, which was the leading hemisphere during the E15 flyby. Because of limited observational constraints on the atmosphere and consequently a large number of free parameters involved in specifying the atmosphere model, our modeling did not lead to definitive conclusions about the detailed configuration of the atmosphere during this flyby. However, our work raised new questions about the coupling between Europa's atmosphere and plasma interaction that should be addressed through future work.

In **Chapter 5** we set out to investigate the connections between Europa's atmosphere and plasma interaction in a more systematic fashion. We consulted the current constraints on Europa's atmosphere to consider a set of atmosphere models for a new parameter study. In this study we mainly varied parameters of the atmosphere, but we also included two sets of simulations to compare the effects of different magnetospheric conditions in conjunction with changes in the atmosphere. We observed that variations of the atmosphere within reasonable ranges can result in changes in the plasma density by several orders of magnitude at the same altitudes in different simulations. This result agrees with the large variability of Europa's ionospheric density observed by the *Galileo* radio occultation experiment (McGrath et al., 2009). As we did in **Chapter 3**, we then analyzed the precipitation of thermal plasma in the simulations. We found that the precipitation rate quickly decreases with increasing column density, then levels off at a rate determined by the density of the upstream plasma.

Together, **Chapter 3** and **Chapter 5** paint a multi-dimensional picture of how precipitation of magnetospheric plasma depends on the variation of Europa's plasma interaction. The precipitation rate is a function of two features of the system; the density of the magnetospheric plasma, and the degree to which plasma impinges on the surface or is diverted away by the plasma interaction. In **Chapter 3** we studied the effects of variation in the density of the upstream plasma. In **Chapter 5** we varied the atmosphere, which primarily controls the diversion of magnetospheric plasma. We studied the external and internal factors separately to understand how they alter the plasma interaction and ultimately control the precipitation rate. In doing so we laid the groundwork to synthesize these two trends, enabling us to conduct more realistic simulations in the future that incorporate both of these effects, and to untangle the results.

6.2 Outlook

6.2.1 Connections with Europa Clipper

NASA's upcoming *Europa Clipper* mission (Howell and Pappalardo, 2020) will greatly improve our understanding of Europa's plasma interaction and its coupling to the neutral atmosphere. *Europa Clipper* will conduct over 40 close flybys of the moon during which the magnetic field and plasma near Europa will be observed simultaneously by the Europa Clipper Magnetometer (ECM) and the Plasma Instrument for Magnetic Sounding (PIMS) investigations. Further, Europa Clipper's Ultraviolet Spectrograph (Europa-UVS) and other *in situ* instruments (e.g., the MAss SPectrometer for Planetary EXploration/Europa, or MASPEX) will provide new measurements of Europa's neutral atmosphere, better constraining the structure and variability of the atmosphere. Simultaneous observations of the plasma interaction and atmosphere will be critical for supplying input parameters to global simulations of Europa's plasma interaction, such

as the multi-fluid MHD model presented in this dissertation, which in turn can provide 3D global context for interpreting the observations. Such an effort will enhance the science return of *Europa Clipper* by illuminating the coupling between the electromagnetic fields, atmosphere, and plasma populations at Europa.

6.2.2 Coupling between Europa's surface, atmosphere, and plasma interaction

As described in **Chapter 1,** Europa's atmosphere is generated by sputtering interactions between magnetospheric plasma and Europa's icy surface. We have established in **Chapter 3** and **Chapter 5** that the plasma interaction controls this precipitation, and that changes in the neutral atmosphere have significant effects on the plasma interaction itself. Thus, Europa's surface, atmosphere, and plasma interaction are coupled together by exchanges of mass and energy. The amount of sputtered neutrals entering Europa's atmosphere depends in part on the access of the magnetospheric plasma to Europa's surface, which is in turn affected by the strength of the electromagnetic interaction with the ionosphere generated from the neutral atmosphere. One can imagine that this system incorporates feedback between the different elements: a denser neutral atmosphere would tend to generate a denser ionosphere, which as we showed in **Chapter 5** tends to impede the precipitation of thermal magnetospheric plasma. Energetic particles also play a significant role in weathering and otherwise altering Europa's icy surface (Paranicas et al., 2009; Breer et al., 2019; Nordheim et al., 2018), including producing atmospheric O_2 by sputtering (Johnson et al., 2009; Cassidy et al., 2013; Vorburger and Wurz, 2018). Though energetic particles are not expected to significantly alter the magnetic fields of the plasma interaction because the total pressure of the ambient environment is dominated by the magnetic field (Kivelson et al., 2004), their contribution to the yield of sputtered neutrals would be necessary to accurately model this coupling between Jupiter's magnetosphere and Europa's

atmosphere. While our current model does not include the energetic particle population, their precipitation can be estimated by tracing energetic particles through the electromagnetic fields simulated by the MHD model (Nordheim et al., 2021).

By characterizing the variability of the plasma interaction and investigating trends in the precipitation rate, we have begun to bridge the gap between models for Europa's plasma interaction and models for the atmosphere. The work completed for this dissertation is therefore simply the first step towards a holistic understanding of the rich, complex system of Europa's space environment.

Appendices

Appendix A Coordinate Systems

A.1 Jupiter System-III

This coordinate system rotates with the planet Jupiter. It is useful for analyzing data that is governed by the 11-hour period of Jupiter's rotation, and for determining Europa's position within Jupiter's magnetosphere. Throughout this dissertation we use the right-handed System-III longitude. This means that Europa's longitude decreases with time as Jupiter rotates. While 0˚ S-III longitude has no particular significance here, it may be useful to note that Europa is positioned at 0˚ S-III longitude about an hour after its most southward excursion from Jupiter's plasma sheet. Further details are given by Bagenal and Wilson (2015).

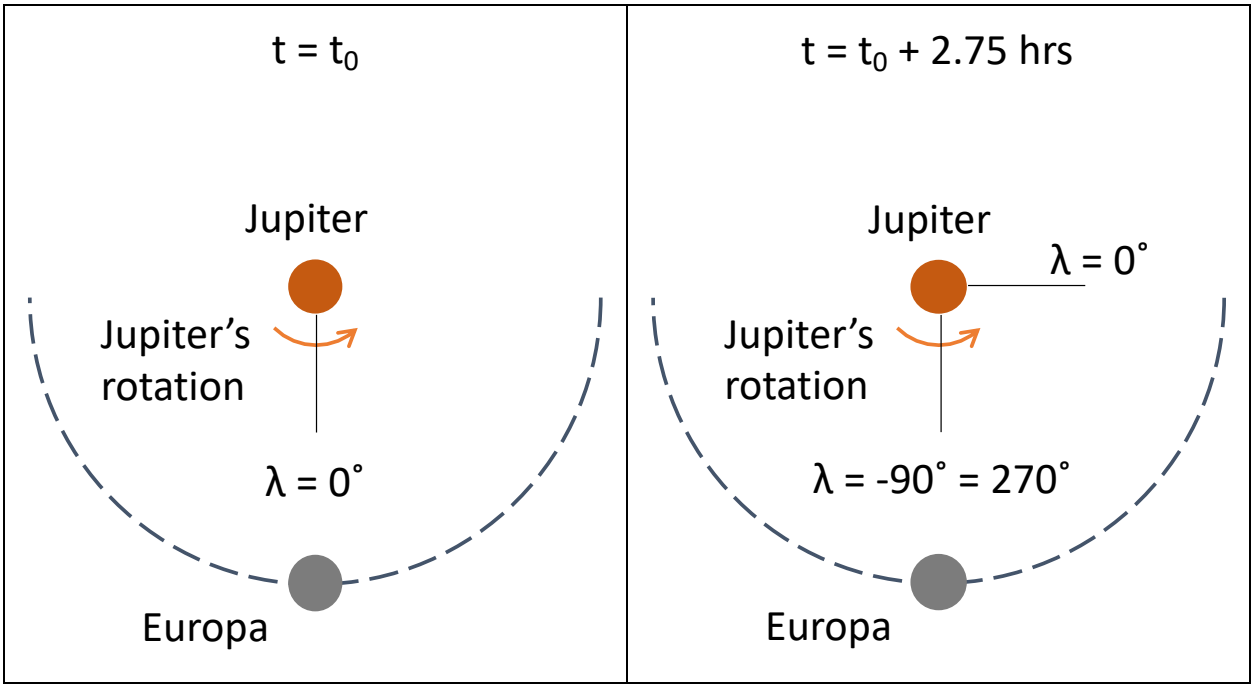

Figure A.1: Diagram of Europa's position in Jupiter System-III longitude.

A.2 E-Phi-Omega (EPO)

E-Phi-Omega (EPO or EPhiO) is a Europa-centric coordinate system used to analyze *in situ* magnetic field and plasma measurements (Kivelson et al., 2009).

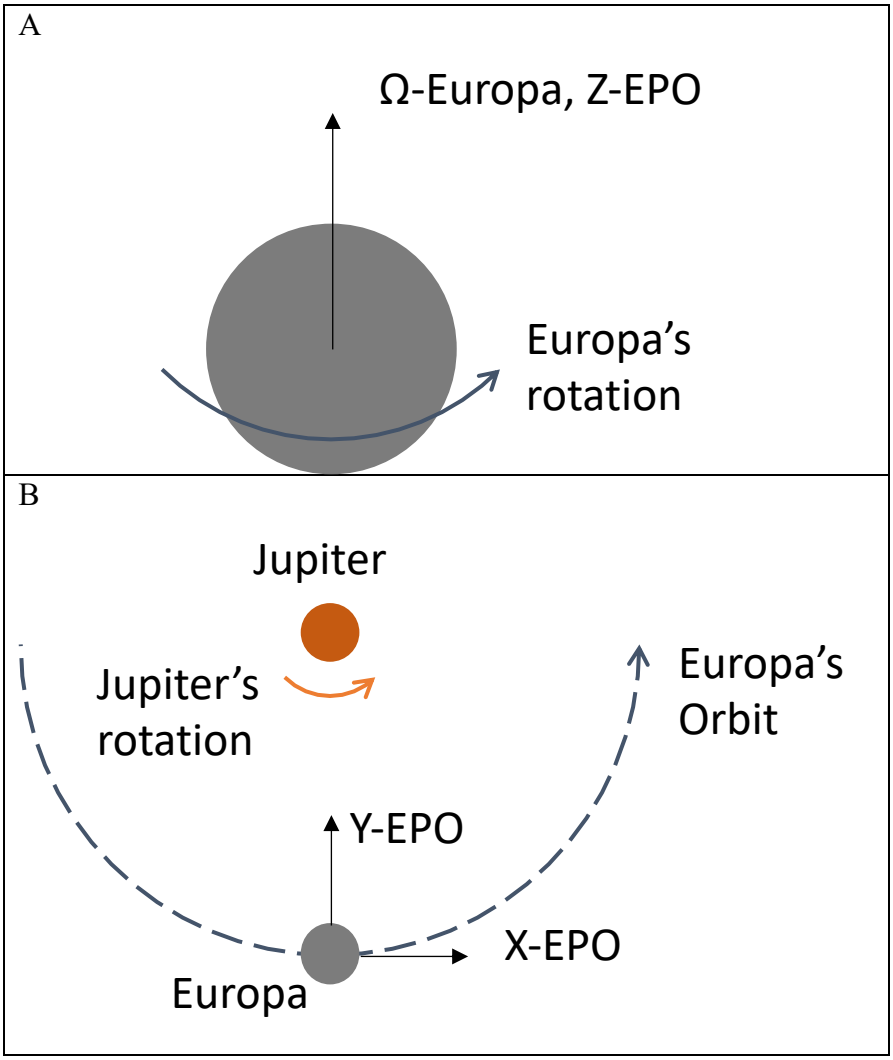

Figure A.2: (A) In the EPhiO coordinate system, Z is aligned with Europa's spin axis. (B) The vector X is along the background flow and $\vec{Y} = \vec{Z} \times \vec{X}$ is positive towards Jupiter.

A.3 E-Phi-B (EPB)

E-Phi-B is a Europa-centric coordinate system used to analyze *in situ* magnetic field and plasma measurements (Kivelson et al., 2009). If the bulk flow velocity is assumed to be parallel to Europa's orbital motion, it differs from the E-Phi-O system by a rotation about the X-axis such that the background magnetic field lies in the XZ-EPB plane. This coordinate system organizes the data around the natural characteristics of the plasma interaction.

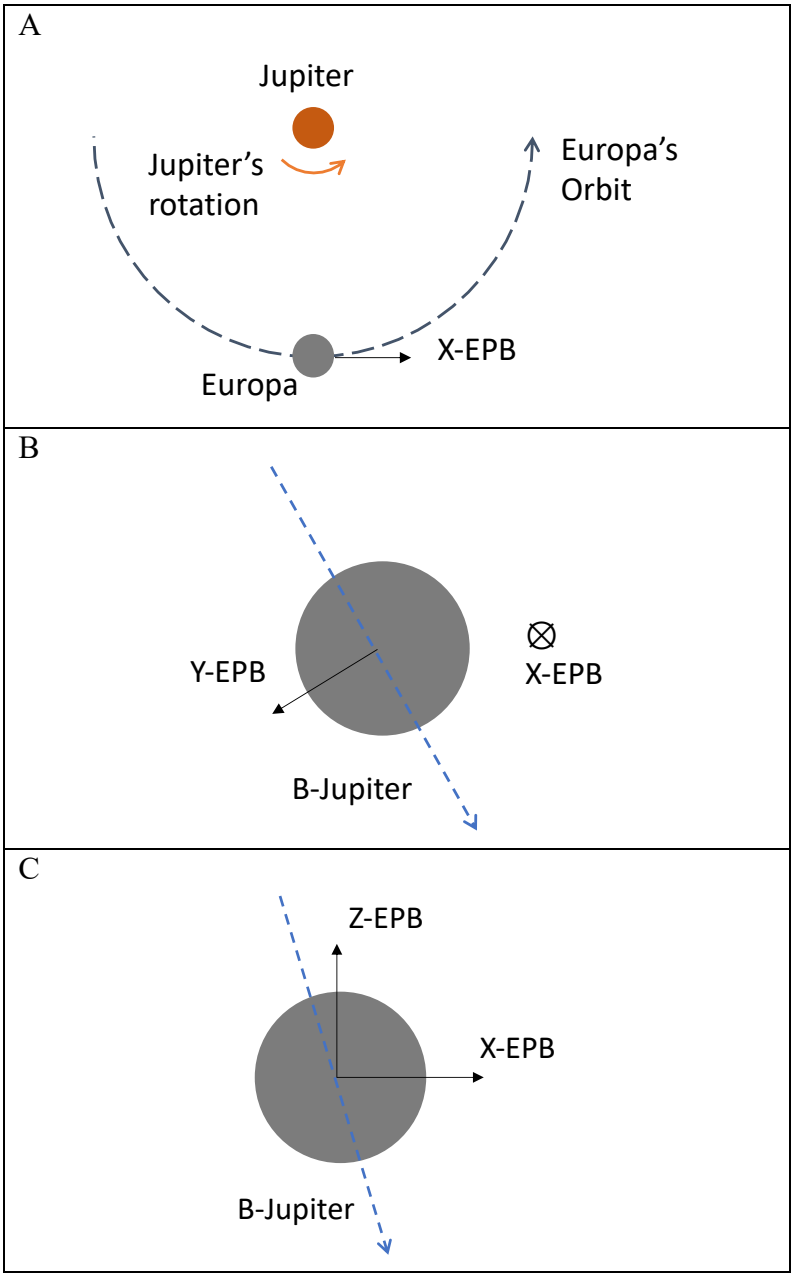

Figure A.3: (A) In the EPhiB coordinate system, x is along the background flow. (B) The vector $\vec{Y} = \hat{b} \times \vec{X}$ and is positive towards Jupiter, where $\hat{b}$ is the background Jovian magnetic field at the time of the spacecraft's closest approach. (C) The vector $\vec{Z} = \vec{X} \times \vec{Y}$ and B lies in the XZ plane.

A.4 Europa Geographic

This coordinate system is used to analyze data on Europa's surface. It has been used for many applications, e.g. by Paranicas et al. (2009) to analyze the precipitation of magnetospheric particles onto Europa's surface.

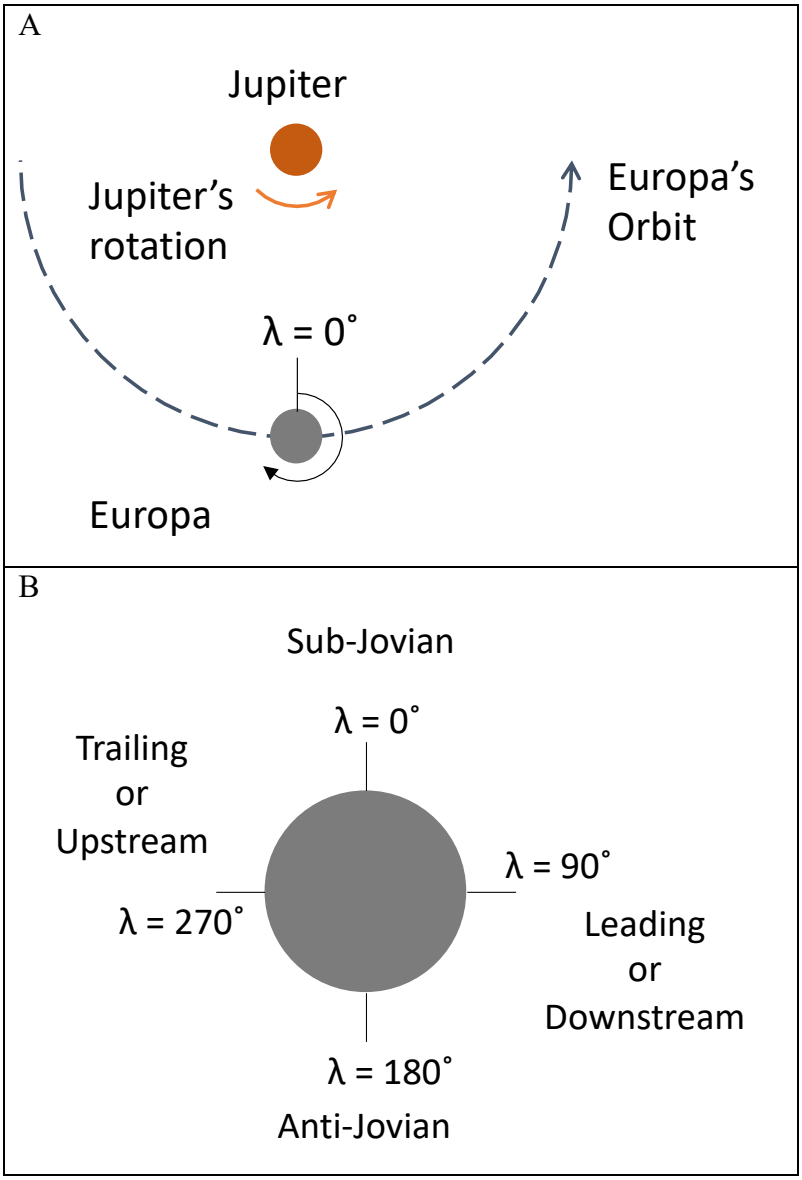

Figure A.4: (A) Europa geographic longitude originates at the Jupiter-facing meridian. West longitude increases in the opposite sense to Europa's orbital motion. (B) The hemispheres centered at 0˚ and 180˚ West lon. are respectively called the sub- and anti-Jovian hemispheres. The hemispheres centered at 90˚ and 270˚ West lon. are respectively called the leading and trailing hemispheres in reference to Europa's orbital motion, or the down- and upstream hemispheres in reference to magnetospheric plasma flow. In EPhiO coordinates, the sub-jovian meridian corresponds to the +Y axis, the leading meridian corresponds to the +X axis, the anti-jovian meridian corresponds to the -Y axis, and the trailing meridian corresponds to the -X axis.

Bibliography

Arnold, H., Liuzzo, L., & Simon, S. (2019, feb). Magnetic signatures of a plume at Europa during the Galileo E26 flyby. Geophysical Research Letters, 46(3), 1149–1157. doi: 10.1029/2018gl081544

Arnold, H., Liuzzo, L., & Simon, S. (2020, jan). Plasma interaction signatures of plumes at Europa. Journal of Geophysical Research: Space Physics, 125(1). doi: 10.1029/2019ja027346

Bagenal, F., & Dols, V. (2020, may). The space environment of io and Europa. Journal of Geophysical Research: Space Physics, 125(5). doi: 10.1029/2019ja027485

Bagenal, F., Sidrow, E., Wilson, R. J., Cassidy, T. A., Dols, V., Crary, F. J., . . . Paterson, W. R. (2015, nov). Plasma conditions at Europa's orbit. Icarus, 261, 1–13. doi: 10.1016/j.icarus.2015.07.036

Bagenal, F. & Wilson, R. J. (2015). Jupiter Coordinate Systems. LASP – U of Colorado. Retrieved June 14, 2021 from https://lasp.colorado.edu/home/mop/files/2015/02/CoOrd_systems7.pdf

Blöcker, A., Saur, J., & Roth, L. (2016, oct). Europa's plasma interaction with an inhomogeneous atmosphere: Development of Alfvén winglets within the Alfvén wings. Journal of Geophysical Research: Space Physics, 121(10), 9794–9828. doi: 10.1002/2016ja022479

Breer, B. R., Liuzzo, L., Arnold, H., Andersson, P. N., & Simon, S. (2019, sep). Energetic ion dynamics in the perturbed electromagnetic fields near Europa. Journal of Geophysical Research: Space Physics, 124(9), 7592–7613. doi: 10.1029/2019ja027147

Carlson, R. W., Calvin, W. M., Dalton, J. B., Hansen, G. B., Hudson, R. I., Johnson, R. E., . . . Moore, M. H. (2009). Europa's surface composition. In R. T. Pappalardo, W. B. McKinnon, & K. K. Khurana (Eds.), Europa (chap. 12). University of Arizona Press.

Carnegie Science. (2018). A Dozen New Moons of Jupiter Discovered, Including One "Oddball". Retrieved October 28, 2021, from https://carnegiescience.edu/news/dozen-new-moons-jupiter-discovered-including-one-%E2%80%9Coddball%E2%80%9D.

Cassidy, T. A., Johnson, R. E., McGrath, M. A., Wong, M. C., & Cooper, J. F. (2007, nov). The spatial morphology of Europa's near-surface O2 atmosphere. Icarus, 191(2), 755–764. doi: 10.1016/j.icarus.2007.04.033

Cassidy, T. A., Paranicas, C. P., Shirley, J. H., Dalton III, J. B., Teolis, B. D., John- son, R. E., . . . Hendrix, A. R. (2013, mar). Magnetospheric ion sputtering and water ice grain size at Europa. Planetary and Space Science, 77, 64–73. doi: 10.1016/j.pss.2012.07.008

Collinson, G., Paterson, W. R., Bard, C., Dorelli, J., Glocer, A., Sarantos, M., & Wilson, R. (2018, apr). New results from Galileo s first flyby of Ganymede: Reconnection-driven

flows at the low-latitude magnetopause boundary, crossing the cusp, and icy ionospheric escape. Geophysical Research Letters, 45(8), 3382–3392. doi: 10.1002/2017gl075487

Galilei, G., Carlos, E. Stafford., Kepler, J. (1880). The sidereal messenger of Galileo Galilei: and a part of the preface to Kepler's Dioptrics containing the original account of Galileo's astronomical discoveries. London: Dawsons of Pall Mall.

Glocer, A., Tóth, G., Ma, Y., Gombosi, T., Zhang, J. C., & Kistler, L. M. (2009, dec). Multifluid Block-Adaptive-Tree Solar wind Roe-type Upwind Scheme: Magnetospheric composition and dynamics during geomagnetic storms-initial results. Journal of Geophysical Research: Space Physics, 114(A12), n/a–n/a. doi: 10.1029/2009ja014418

Hall, D. T., Feldman, P. D., McGrath, M. A., & Strobel, D. F. (1998, may). The far-ultraviolet oxygen airglow of Europa and Ganymede. The Astrophysical Journal, 499(1), 475–481. doi: 10.1086/305604

Hall, D. T., Strobel, D. F., Feldman, P. D., McGrath, M. A., & Weaver, H. A. (1995, feb). Detection of an oxygen atmosphere on Jupiter's moon Europa. Nature, 373(6516), 677–679. doi: 10.1038/373677a0

Harris, C. D. K., Jia, X., Slavin, J. A., Toth, G., Huang, Z., & Rubin, M. (2021). Multi-fluid MHD simulations of Europa's plasma interaction under different magnetospheric conditions. *Journal of Geophysical Research: Space Physics*, *126*, e2020JA028888. https:// doi.org/10.1029/2020JA028888

Howell, S. M., & Pappalardo, R. T. (2020, mar). Nasa's Europa Clipper– a mission to a potentially habitable ocean world. Nature Communications, 11(1). doi: 10 .1038/s41467-020-15160-9

Huebner, W. F., J. J. Keady, and S. P. Lyon (1992), Solar photo rates for planetary atmospheres and atmospheric pollutants, Astrophys. Space Sci., 195, 1–289.

Huybrighs, H. L. F. (2018). A search for signatures of Europa's atmosphere and plumes in Galileo charged particle data (Unpublished doctoral dissertation). Technische Universitat Braunschweig.

Hwang, W., Y.-K. Kim, and M. E. Rudd (1996), New model for electron-impact ionization cross sections of molecules, J. Chem. Phys., 104, 2956–2966.

Jia, X., Kivelson, M. G., Khurana, K. K., & Kurth, W. S. (2018, may). Evidence of a plume on Europa from Galileo magnetic and plasma wave signatures. Nature Astronomy, 2(6), 459–464. doi: 10.1038/s41550-018-0450-z

Jia, X., Walker, R. J., Kivelson, M. G., Khurana, K. K., & Linker, J. A. (2009, sep). Properties of Ganymede's magnetosphere inferred from improved three- dimensional MHD simulations. Journal of Geophysical Research: Space Physics, 114(A9), n/a–n/a. doi: 10.1029/2009ja014375

Johnson, R. E., Burger, M. H., Cassidy, T. A., Leblanc, F., Marconi, M., & Smyth, W. H. (2009). Composition and detection of Europa's sputter-induced atmosphere. In R. T. Pappalardo, W. B. McKinnon, & K. K. Khurana (Eds.), Europa (chap. 21). University of Arizona Press.

Khurana, K. K. (1997, jun). Euler potential models of Jupiter's magnetospheric field. Journal of Geophysical Research: Space Physics, 102(A6), 11295–11306. doi: 10.1029/97ja00563

Khurana, K. K., Kivelson, M. G., Stevenson, D. J., Schubert, G., Russell, C. T., Walker, R. J., & Polanskey, C. (1998, oct). Induced magnetic fields as evidence for subsurface oceans in Europa and Callisto. Nature, 395(6704), 777–780. doi: 10.1038/27394

Khurana, K. K., Kivelson, M. G., Vasyliunas, V. M., Krupp, N., Woch, J., Lagg, A., . . . Kurth, W. S. (2004). The configuration of Jupiter's magnetosphere. In F. Bagenal, T. E. Dowling, & W. B. McKinnon (Eds.), Jupiter: The planet, satellites, and magnetosphere (chap. 24). Cambridge University Press.

Kivelson, M. G. (2000, aug). Galileo magnetometer measurements: A stronger case for a subsurface ocean at Europa. Science, 289(5483), 1340–1343. doi: 10 .1126/science.289.5483.1340

Kivelson, M. G., Bagenal, F., Kurth, W. S., Neubauer, F. M., Paranicas, C., & Saur, J. (2004). Magnetospheric interactions with satellites. In F. Bagenal, T. E. Dowling, & W. B. McKinnon (Eds.), Jupiter: The planet, satellites, and magnetosphere (chap. 21). Cambridge University Press.

Kivelson, M. G., & Khurana, K. K. (2009). Europa's interaction with the Jovian magnetosphere. In R. T. Pappalardo, W. B. McKinnon, & K. K. Khurana (Eds.), Europa (chap. 23). University of Arizona Press.

Kliore, A. J. (1997, jul). The ionosphere of Europa from Galileo radio occultations. Science, 277(5324), 355–358. doi: 10.1126/science.277.5324.355

Kurth, W. S., Gurnett, D. A., Persoon, A. M., Roux, A., Bolton, S. J., & Alexander, C. J. (2001). The plasma wave environment of Europa. Planetary and Space Science, 49(3), 345–363. (Magnetospheres of the Outer Planets (Part I)) doi: https://doi.org/10.1016/S0032-0633(00)00156-2

Lipatov, A. S., Cooper, J. F., Paterson, W. R., Jr., E. C. S., Hartle, R. E., & Simp- son, D. G. (2013, mar). Jovian plasma torus interaction with Europa. plasma wake structure and effect of inductive magnetic field: 3D hybrid kinetic simulation. Planetary and Space Science, 77, 12–24. doi: 10.1016/j.pss.2013.01.009

Lipatov, A. S., Cooper, J. F., Paterson, W. R., Sittler, E. C., Hartle, R. E., & Simp- son, D. G. (2010, nov). Jovian plasma torus interaction with Europa: 3D hybrid kinetic simulation. first results. Planetary and Space Science, 58(13), 1681–1691. doi: 10.1016/j.pss.2010.06.015

Mauk, B. H. (2004). Energetic ion characteristics and neutral gas interactions in Jupiter's magnetosphere. Journal of Geophysical Research, 109(A9). doi: 10 .1029/2003ja010270

Mauk, B. H., Clark, G., Allegrini, F., Bagenal, F., Bolton, S. J., Connerney, J. E. P., . . . Rymer, A. M. (2020, apr). Juno energetic neutral atom (ENA) remote measurements of magnetospheric injection dynamics in Jupiter's Io torus regions. , 125(5). doi: 10.1029/2020ja027964

McGrath, M. A., Hansen, C. J., & Hendrix, A. R. (2009). Observations of Europa's tenuous atmosphere. In R. T. Pappalardo, W. B. McKinnon, & K. K. Khurana (Eds.), Europa (chap. 20). University of Arizona Press.

Milillo, A., Plainaki, C., Angelis, E. D., Mangano, V., Massetti, S., Mura, A., . . . Rispoli, R. (2016, oct). Analytical model of Europa's O2 exosphere. Planetary and Space Science, 130, 3–13. doi: 10.1016/j.pss.2015.10.011

Neubauer, F. M. (1980, mar). Nonlinear standing Alfvén wave current system at Io: Theory. Journal of Geophysical Research: Space Physics, 85(A3), 1171–1178. doi: 10.1029/ja085ia03p01171

Neubauer, F. M. (1998, aug). The sub-Alfvénic interaction of the Galilean satellites with the Jovian magnetosphere. Journal of Geophysical Research: Planets, 103(E9), 19843–19866. doi: 10.1029/97je03370

Nordheim, T. A., … (2021). Magnetospheric ion bombardment of Europa's surface, Planetary Science J., accepted

Nordheim, T. A., Hand, K. P., & Paranicas, C. (2018, jul). Preservation of potential biosignatures in the shallow subsurface of Europa. Nature Astronomy, 2(8), 673–679. doi: 10.1038/s41550-018-0499-8

Oza, A. V., Leblanc, F., Johnson, R. E., Schmidt, C., Leclercq, L., Cassidy, T. A., & Chaufray, J.-Y. (2019, mar). Dusk over dawn O2 asymmetry in Europa's near-surface atmosphere. Planetary and Space Science, 167, 23–32. doi: 10.1016/j.pss.2019.01.006

Paganini, L., Villanueva, G. L., Roth, L., Mandell, A. M., Hurford, T. A., Retherford, K. D., & Mumma, M. J. (2019, nov). A measurement of water vapour amid a largely quiescent environment on Europa. Nature Astronomy. doi: 10.1038/s41550-019-0933-6

Paranicas, C., Cooper, J. F., Garrett, H. B., Johnson, R. E., & Sturner, S. J. (2009). Europa's radiation environment and its effects on the surface. In R. T. Pappalardo, W. B. McKinnon, & K. K. Khurana (Eds.), Europa (chap. 22). University of Arizona Press.

Paranicas, C., Ratliff, J. M., Mauk, B. H., Cohen, C., & Johnson, R. E. (2002, mar). The ion environment near Europa and its role in surface energetics. Geophysical Research Letters, 29(5), 18–4. doi: 10.1029/2001gl014127

Paterson, W. R., Frank, L. A., & Ackerson, K. L. (1999, oct). Galileo plasma observations at Europa: Ion energy spectra and moments. Journal of Geophysical Research: Space Physics, 104(A10), 22779–22791. doi: 10.1029/1999ja900191

Plainaki, C., Cassidy, T. A., Shematovich, V. I., Milillo, A., Wurz, P., Vorburger, A., . . . Teolis, B. (2018, jan). Towards a global unified model of Europa's tenuous atmosphere. Space Science Reviews, 214(1). doi: 10.1007/s11214-018-0469-6

Plainaki, C., Milillo, A., Mura, A., Saur, J., Orsini, S., & Massetti, S. (2013, nov). Exospheric O2 densities at Europa during different orbital phases. Planetary and Space Science, 88, 42–52. doi: 10.1016/j.pss.2013.08.011

Pospieszalska, M. K., & Johnson, R. E. (1989, mar). Magnetospheric ion bombardment profiles of satellites: Europa and Dione. Icarus, 78(1), 1–13. doi: 10 .1016/0019-1035(89)90065-1

Roth, L., Saur, J., Retherford, K. D., Strobel, D. F., Feldman, P. D., McGrath, M. A., & Nimmo, F. (2013, dec). Transient water vapor at Europa's south pole. Science, 343(6167), 171–174. doi: 10.1126/science.1247051

Roth, L., Saur, J., Retherford, K. D., Strobel, D. F., Feldman, P. D., McGrath, M. A., . . . Ivchenko, N. (2016, mar). Europa's far ultraviolet oxygen aurora from a comprehensive set of HST observations. Journal of Geophysical Research: Space Physics, 121(3), 2143–2170. doi: 10.1002/2015ja022073

Rubin, M., Jia, X., Altwegg, K., Combi, M. R., Daldorff, L. K. S., Gombosi, T. I., . . . Wurz, P. (2015, may). Self-consistent multifluid MHD simulations of Europa's

exospheric interaction with Jupiter's magnetosphere. Journal of Geophysical Research: Space Physics, 120(5), 3503–3524. doi: 10.1002/2015ja021149

Rubin, M., Koenders, C., Altwegg, K., Combi, M. R., Glassmeier, K. H., Gombosi, T. I., . . . Tóth, G. (2014, nov). Plasma environment of a weak comet – predictions for comet 67P/Churyumov–Gerasimenko from multifluid-MHD and hybrid models. Icarus, 242, 38–49. doi: 10.1016/j.icarus.2014.07.021

Samson, J. A. R., and J. L. Gardner (1975), On the ionization potential of molecular oxygen, Can. J. Phys., 53(19), 1948–1952, doi:10.1139/p75-244.

Saur, J., Strobel, D. F., & Neubauer, F. M. (1998, aug). Interaction of the Jovian magnetosphere with Europa: Constraints on the neutral atmosphere. Journal of Geophysical Research: Planets, 103(E9), 19947–19962. doi: 10.1029/97je03556

Schilling, N. (2006). Time varying interaction of Europa's atmosphere-ionosphere and it's conducting ocean with the Jovian magnetosphere (Unpublished doctoral dissertation). University of Cologne.

Schilling, N., Neubauer, F. M., & Saur, J. (2007, dec). Time-varying interaction of Europa with the jovian magnetosphere: Constraints on the conductivity of Europa's subsurface ocean. Icarus, 192(1), 41–55. doi: 10.1016/j.icarus.2007.06.024

Schilling, N., Neubauer, F. M., & Saur, J. (2008, mar). Influence of the internally induced magnetic field on the plasma interaction of Europa. Journal of Geophysical Research: Space Physics, 113(A3), n/a–n/a. doi: 10.1029/2007ja012842

Schubert, G., Sohl, F., & Hussman, H. (2009). Interior of Europa. In R. T. Pappalardo, W. B. McKinnon, & K. K. Khurana (Eds.), Europa (chap. 14). University of Arizona Press.

Schunk, R., and A. Nagy (2009), Ionospheres: Physics, Plasma Physics, and Chemistry, Cambridge Univ. Press, Cambridge, U. K.

Southwood, D. J., Kivelson, M. G., Walker, R. J., & Slavin, J. A. (1980). Io and its plasma environment. Journal of Geophysical Research, 85(A11), 5959. doi: 10 .1029/ja085ia11p05959

Sparks, W. B., Hand, K. P., McGrath, M. A., Bergeron, E., Cracraft, M., & Deustua, S. E. (2016, sep). Probing for evidence of plumes on Europa with HST/STIS. The Astrophysical Journal, 829(2), 121. doi: 10.3847/0004-637x/829/2/121

Teolis, B. D., Wyrick, D. Y., Bouquet, A., Magee, B. A., & Waite, J. H. (2017a, mar). Plume and surface feature structure and compositional effects on Europa's global exosphere: Preliminary Europa mission predictions. Icarus, 284, 18–29. doi: 10.1016/j.icarus.2016.10.027

Teolis, B. D., Plainaki, C., Cassidy, T. A., & Raut, U. (2017b, oct). Water ice radiolytic O2 , H2 , and H2 O2 yields for any projectile species, energy, or temperature: A model for icy astrophysical bodies. Journal of Geophysical Research: Planets, 122(10), 1996–2012. doi: 10.1002/2017je005285

Tóth, G., van der Holst, B., Sokolov, I. V., Zeeuw, D. L. D., Gombosi, T. I., Fang, F., . . . Opher, M. (2012, feb). Adaptive numerical algorithms in space weather modeling. Journal of Computational Physics, 231(3), 870–903. doi: 10.1016/j.jcp.2011.02.006

Volwerk, M., Khurana, K., & Kivelson, M. (2007, may). Europa's Alfvén wing: shrinkage and displacement influenced by an induced magnetic field. Annales Geophysicae, 25(4), 905–914. doi: 10.5194/angeo-25-905-2007

Volwerk, M., Kivelson, M. G., & Khurana, K. K. (2001, nov). Wave activity in Europa's wake: Implications for ion pickup. Journal of Geophysical Research: Space Physics, 106(A11), 26033–26048. doi: 10.1029/2000ja000347

Vorburger, A., & Wurz, P. (2018, sep). Europa's ice-related atmosphere: The sputter contribution. Icarus, 311, 135–145. doi: 10.1016/j.icarus.2018.03.022

Yoshioka, K., Tsuchiya, F., Kagitani, M., Kimura, T., Murakami, G., Fukuyama, D., . . . Fujimoto, M. (2018, oct). The influence of Ios 2015 volcanic activity on Jupiter's magnetospheric dynamics. , 45(19), 10,193–10,199. doi: 10.1029/2018gl079264

Zimmer, C. (2000, oct). Subsurface oceans on Europa and Callisto: Constraints from Galileo magnetometer observations. Icarus, 147(2), 329–347. doi: 10.1006/icar .2000.6456